University Of Oxford



Mathematical, Physical and Life Science Division,
Department Of Physics,
Atomic And Laser Physics

2014

D.Phil. Thesis

Plasma Evolution and Continuum Lowering in Hot Dense Matter generated by X-ray Free Electron Lasers

Orlando Ciricosta

Supervisor: Prof. J.S. Wark

Plasma Evolution and Continuum Lowering in Hot Dense Matter generated by X-ray Free Electron Lasers

Orlando Ciricosta
Wolfson College

Thesis submitted for the Degree of Doctor of Philosophy
Hilary Term 2014

Abstract

The advent of the 4th generation X-ray sources paves the way for a new phase of experimental investigation of Hot-Dense plasmas. At the Linac Coherent Light Source (LCLS), pulses of keV X-rays, shorter than 100 fs, and with intensities up to 10^{18} W·cm^{-2}, are routinely produced, allowing for the production of uniform samples of solid-density plasmas. The simple single-photon X-ray absorption mechanism can be easily modelled, so that the plasma conditions can be accurately retrieved, without relying on diagnostic techniques that are not benchmarked in this high density regime.

The work presented here describes the results of the first experiment where the LCLS interacts with a solid Al target, isochorically heating it at temperatures up to 190 eV. The system is described by the SCFLY non-LTE model, where the density and temperature are computed self consistently, as a consequence of the detailed atomic processes, rather than imposed by the user. The approximations affecting the simulations are discussed in detail.

The code is first validated, by modelling the charge state distribution measured in a previous experiment (L. Young *et. al*), where the LCLS interacts with a Ne gas, a simplified (collisionless) problem. Then it is used to model the K_α spectroscopic data obtained for Al. The plasma evolution, explained by SCFLY simulations, is found to be primarily determined by collisions, whose visible effects on the experimental spectra are discussed.

By varying the wavelength of the laser and observing the change in the K_α fluorescence, the K-edges for different ions in the plasma were determined, leading to a charge resolved measurement of continuum lowering in the HDM system. The results disagree with the widely used Stewart-Pyatt model, with the disagreement increasing for higher charge states, but are consistent with the older Ecker-Kröll model. These results have profound implications for dense plasma modelling.

to Sam and Andrea,
whose companionship along the Road
has no price

Acknowledgements

There are three people I feel compelled to thank here before anyone else, for their primary role in this work. First I'd like to thank Justin Wark: his supervision has been invaluable, both for the work described in this thesis, and for the development of my professional skills. Second I want to thank Sam Vinko, for being an excellent senior professional partner, a trusted friend, and because I'd be incredibly lucky if I absorbed even the smallest fraction of his networking skills. Finally I want to thank Hyun-Kyun Chung: she has always been very keen to help me with SCFLY, and our collaboration has been fundamental to the results presented in this work.

I'd also like to thank all of the authors of Ref. [1,2] for their contribution on the Al work, and in particular David Rackstraw, for the daily discussions about the data. A special thanks also goes to Dick Lee, for his major contribution to both the Ne and Al work described here, to Benjamin Barbrel, who has worked with me on the setup of the follow-up experiment described in the final chapter of this thesis, and to Basil Crowley for the stimulating discussions on the nature of continuum lowering.

Apart from the people directly involved with the research, I'd also like to thank my family and the friends, colleagues and flat mates who have supported me during my DPhil period. First of all I'd like to thank Francesca: I've always felt welcome in her and Sam's place, and she is also the most skilled "pizzaiola" I have ever met. Second I'd like to thank all the wonderful people I have met at the various conferences and experiments, without whom my DPhil would have surely been much less fun: a list of names would be unpractical here, but I am sure the relevant people can guess who I am talking about. A particular thanks goes to David M., for relentlessly pointing out the random output of my vocal folds, whenever my poor brain gets lost between the various "tough and bough and cough and dough", and also to Gabriel, for sharing jewels such as "Heavy metal farmer" on my Facebook page. Thanks also to all of the other members of the group, with whom I have shared conferences, dinners, experiments, referee's reports etc. Finally, though she can't read, I want to thank hurricane Rika, who considers me good enough as a pillow: I appreciate that.

The author is grateful to the U.K. EPSRC for support under grant number EP/H035877/1. Portions of this research were carried out on the SXR Instrument at the Linac Coherent Light Source (LCLS), a division of SLAC National Accelerator Laboratory and an Office of Science user facility operated by Stanford University for the U.S. Department of Energy. The SXR Instrument is funded by a consortium whose membership includes the LCLS, Stanford University through the Stanford Institute for Materials Energy Sciences (SIMES), Lawrence Berkeley National Laboratory (LBNL), University of Hamburg through the BMBF priority program FSP 301, and the Center for Free Electron Laser Science (CFEL).

Contents

Abstract **i**

Acknowledgements **iii**

1 Introduction **1**
1.1 Hot Dense Matter 1
1.2 HDM studies with X-ray Lasers 4
1.2.1 The Linac Coherent Light Source (LCLS) 9
1.2.2 Modelling the laser-matter interaction: SCFLY 11
1.3 Structure of the thesis 14
1.4 Author contribution 15

2 Reduced problem: X-ray laser interacting with a gas **17**
2.1 Young's experiment on Neon 18
2.1.1 Experimental results 19
2.2 SCFLY simulations 22
2.2.1 Local evolution 27
2.2.2 Role of collisions 33

3 Isochoric heating of Aluminium foils to the HDM regime **38**
3.1 The experiment 39
3.1.1 Data analysis technique 40
3.1.2 K-alpha spectroscopy 41

3.1.3 Experimental results . . . 42
3.2 Simulations . . . 45
3.2.1 Temperature and density evolution . . . 47
3.2.2 Charge states distribution . . . 51
3.3 Collisional processes . . . 53
3.3.1 Time-dependent emission . . . 56

4 Continuum lowering in Hot Dense Aluminium 59
4.1 Continuum lowering in dense plasmas . . . 60
4.1.1 Stewart-Pyatt model . . . 62
4.1.2 Ecker-Kröll model . . . 64
4.2 Measuring the IPD . . . 69
4.3 Experimental results . . . 71
4.3.1 K-edges and simulated spectra . . . 73
4.3.2 Pressure ionization effects . . . 77
4.4 Remarks . . . 79

5 Details of the modelling 81
5.1 Modelling the X-ray laser properties . . . 81
5.1.1 Measured spatial profile . . . 82
5.1.2 SASE temporal profile and pulse duration . . . 86
5.1.3 Beamline transmission . . . 91
5.2 Instantaneous thermalization . . . 93
5.2.1 Auger electrons simulations . . . 94

6 Conclusions and future work 102
6.1 Summary and Conclusions . . . 102
6.2 Further work on IPD . . . 105
6.2.1 LCLS experiment on different materials . . . 106
6.2.2 Pressure ionization at Orion and OMEGA . . . 106
6.3 Further work on the Al data . . . 108
6.4 Further work on SCFLY . . . 109

References 111

List of Acronyms 121

List of Figures 123

Notation 124

CHAPTER 1

Introduction

The work presented in this thesis is a modest contribution to the tremendous research effort aimed to study those plasmas that cannot be described by the classical ideal plasma theory. In particular it is about a new experimental and modelling framework capable of providing unprecedented insight into the physics of plasmas in the Hot Dense Matter (HDM) regime, and about its first scientific outcome.

1.1 Hot Dense Matter

Plasmas in the HDM regime are characterized by densities near and above the characteristic density of a solid ($\sim$ 1 g·cm^{-3}) and temperatures of the order of hundreds eV; when the temperature is instead in the range from 1 to a few tens of eV, the plasma is said to be in the Warm Dense Matter

state, or WDM.

In a HDM/WDM plasma the inter-particle Coulomb interaction energies are comparable or even greater than the thermal energy and, as a result, the standard perturbative approaches which are the backbone of plasma physics [3,4] are not applicable (see also §4.1). On the other hand, given that the thermal energy is not negligible either, the system cannot be described with a solid state theory approach, so that a rigorous theoretical description of such a plasma poses a formidable challenge.

The condition that describes this state in terms of electron density (n_e) and temperature (T_e) can be expressed by the electron-electron coupling parameter

$$\Gamma_{ee} = \frac{e^2}{k_B T_e} \left(\frac{3}{4\pi n_e} \right)^{-1/3}. \tag{1.1}$$

When this quantity is greater than or of the order of 1, the Coulomb interactions between electrons cannot be treated perturbatively, when instead it approaches $1/\bar{z}$ or $1/\bar{z}^{5/3}$ – where $\bar{z}$ is the average ionization degree of the plasma, defining the average charge of the ions $\bar{z}e$, and the ion density $n_i = n_e/\bar{z}$ – the same holds for the treatment of the electron-ion and ion-ion interactions respectively. This defines the ion-electron and ion-ion coupling parameters $\Gamma_{ei} = \bar{z}\Gamma_{ee}$ and $\Gamma_{ii} = \bar{z}^{5/3}\Gamma_{ee}$.

A material independent plot showing the regions of the density-temperature space roughly occupied by HDM and WDM is shown in Fig. 1.1, along with the isolines for three values of the quantity defined by Eq. (1.1); note, as an example, that the isoline $\Gamma_{ee} = 0.1$ corresponds to $\Gamma_{ii} = 1$ for a plasma with $\bar{z} \simeq 4$, so that such a plasma would still be strongly coupled. Also shown are a few examples of real life non-ideal plasmas, compared with the density and temperature conditions for the experiment described in this thesis. The importance of understanding the behaviour of materials in the

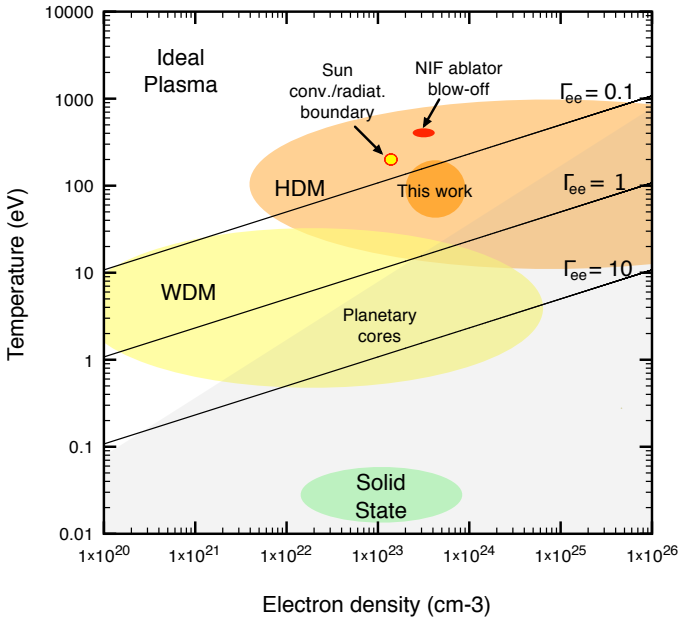

Figure 1.1: Temperature-density phase diagram for the general plasma. A few isolines for the parameter Γ_{ee} described by Eq. (1.1) are shown, as well as the regions corresponding approximately to the HDW and WDM regimes. Note that HDM plasmas are usually highly ionized, so that the Γ_{ie} and Γ_{ii} can exceed Γ_{ee} by more than an order of magnitude for non-hydrogen plasmas. The shaded region corresponds to temperatures below the Fermi temperature, where electron degeneracy effects become significant and the electron coupling parameter differs from the plotted Γ_{ee} (see text). A few examples of plasma conditions, along with the range of conditions achieved in the experiment described in this thesis, are also plotted.

HDM regime is typified by the two examples reported on the plot.

Firstly HDM studies are important in the context of the physics of inertial confinement fusion (ICF) [5, 6]. In particular, in the indirect-drive approach [7, 8], the understanding of how high-density carbon and gold react when heated to temperatures of a few hundreds eV is essential in order to model the blow-off phase of the compression [9], and the opacity properties of the hohlraum walls, determining the X-ray energy losses, and thus the efficiency of the laser-target coupling [10].

Second, HDM (and WDM) plasmas occur in any kind of star. As an example the plot in Fig. 1.1 shows the conditions expected at the boundaries between the radiative and the convective zone of the Sun [11, 12], where even modest opacity variations due to metals (i.e. lithium and heavier elements) affect the heat conduction, and thus the structural models, of the solar interior [13–15]. In these conditions the electron density will be largely determined by the fully ionized hydrogen and helium plasma, but the relevant quantity determining the opacity is the partial ionization of the heavier ions embedded in this environment: if z denotes the average ionization of the species under consideration (dependent on the continuum lowering, §4), the relevant coupling parameter, limiting the applicability of standard approaches, is $z\Gamma_{ee}$, which is again greater than 1 for metals in the phase space region under consideration.

For sake of completeness, the shaded region in Fig. 1.1 represents matter with a temperature lower than the Fermi temperature at a given density ($T_F \propto n_e^{2/3}$). In this region Γ_{ee} is not described anymore by Eq. (1.1) due to degeneracy, but can be defined by an effective temperature approach [16, 17]. The plasmas described in this thesis are however largely in the non-degenerate regime, so that the usual expressions are still valid.

1.2 HDM studies with X-ray Lasers

If the theoretical treatment of HDM is a huge challenge, the experimental studies on this subject are no less troublesome. The problems that have hindered so far the experimental investigation of HDM are mainly two: firstly the creation of uniform samples that are at the same time dense, hot and highly ionized, and in a defined density and temperature state for a time long enough to be probed, is far from trivial by using conventional laser-

plasma techniques; second, even the shortest optical probes [18], that could potentially provide the right temporal and spatial resolution to study these fast-evolving states (the relevant timescales are of the order of the femtosecond, see §3), are inevitably unable to propagate through the overdense plasma medium (as an example, at the density of solid Al, the plasma frequency of the Al^{3+} plasma corresponds to a photon energy of $\sim$15 eV).

The natural candidate as the solution of all of these issues is a high-power femtosecond X-ray laser, capable of propagating through a solid density plasma: such a laser can in principle deposit a large amount of energy in the bulk material, before any hydrodynamic expansion occurs, creating a plasma virtually free of longitudinal gradients, and/or can probe a dense plasma, on the same timescales as the evolution of its thermodynamic properties.

Unfortunately, even without paying attention to the aforementioned pulse duration constraints, it is notoriously difficult to generate laser radiation in the X-ray range, due to the lack of efficient cavity mirrors, and to the highly inefficient pumping process to achieve a population inversion in a classic three/four-level laser scheme for these wavelengths. Using a highly ionized plasma as gain medium, XUV pulses with 1 ps $\rightarrow$ 1 ns duration and energies in the range 10 μJ $\rightarrow$ 1 mJ can be produced [19], but the output power of these sources is not enough to be used as a pump. On the other hand high harmonic generation sources can generate extremely short high quality XUV pulses, but the efficiency of the conversion process is generally quite low and dramatically reduces at the shortest output wavelengths [20].

An alternative scheme to achieve lasing action in the X-ray regime is used in a free electron laser (FEL). Here a bunch of relativistic electrons moves through a periodic transverse magnetic field, in a structure called an undulator, emitting stimulated bremsstrahlung at a resonant wavelength,

which along the longitudinal axis is given by [21]

$$\lambda = \frac{\lambda_u}{2\gamma^2}\left(1 + \frac{K_0^2}{2}\right) \tag{1.2}$$

where λ_u is the period of the undulator, γ is the electron energy in units of the rest energy, and K_0 is known as the undulator parameter, given in terms of the amplitude of the magnetic field by $0.934 \cdot B[\mathrm{T}]\lambda_u[\mathrm{cm}]$. Clearly one of the most attractive features of an FEL, if compared with a standard laser, is the great tunability of the emission wavelength, easily achieved by tuning the electron beam energy.

Despite the concept of the undulator being actually older (Motz 1951 [22]) than the very first optical laser operation [23] and the FEL concept being invented in 1971 [24], a major breakthrough for the production of a high-power Xray laser source was the recent coupling of undulators with a linear accelerator machine (4th generation light sources[1]).

Undulators had in fact been used in the past two decades as insertion devices at synchrotron sources (3rd generation light sources), providing high quality, stable X-ray beams, but with either a long pulse duration (tens of ps) or a low photon flux [26]. The lasing gain in these machines is quite limited by the gradual degradation of the electron beam as it repeatedly travels through the ring; that affects the coupling between the light and the electrons during the transit through the undulator, and prevents the build-up of coherent amplified radiation.

The situation is dramatically different with the high quality electron beam produced by a linear accelerator (or linac): here, in a single pass through an undulator, an efficient coupling between the electron bunch and the radiation at the resonant wavelength given by (1.2), leads to a mod-

[1] A summary of the different generations of light sources can be found in [25]

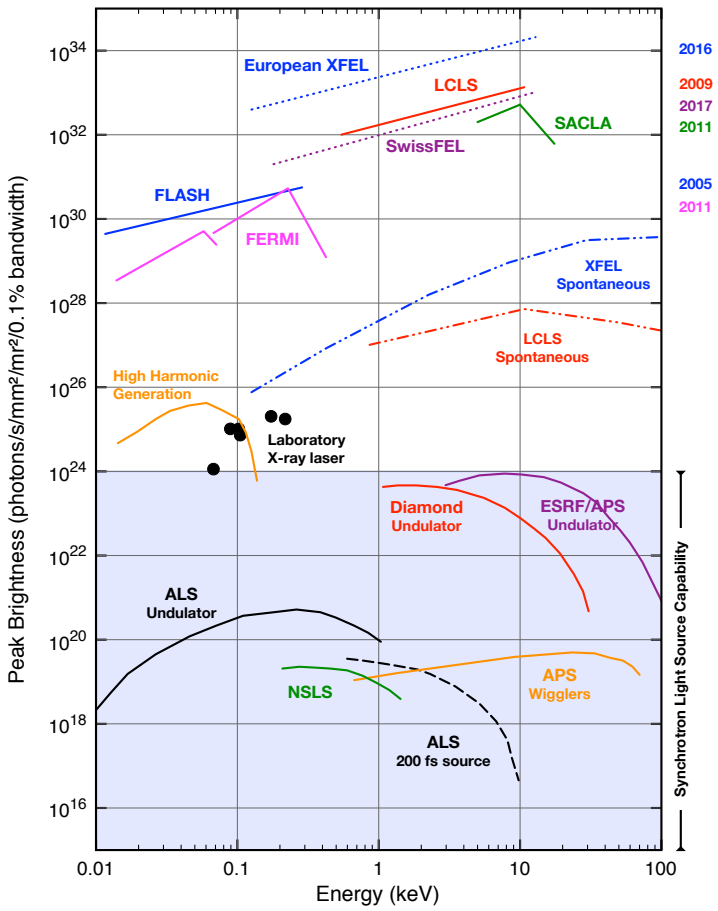

Figure 1.2: Comparison of the peak brightness of available and future light sources in the XUV and X-ray photon energy range. The upper part of the plot shows the operating and planned FEL sources, and the year corresponding to the start of operations. Image courtesy of Dr Vinko.

ulation of the bunch (microbunching), and an exponential growth of the emitted radiation up to a threshold level, that is to the production of an intense laser pulse generated by Self-Amplified Spontaneous Emission (SASE process) [27–29]. The result of changing from a synchrotron to a linac was an impressive jump – to date, up to nine orders of magnitude – in the brightness of the X-rays produced, as can be seen in Fig. 1.2. Importantly, these machines can generate pulses with a duration of 10→100 fs (or even shorter pulses [30]), that also makes them suitable for probing fast evolving

systems, and when focused, intensities up to 10^{18} W·cm^{-2} can be obtained in the X-ray, making them also suitable as a pump laser.

The first operating 4th generation light sources were the Free electron LASer in Hamburg, or FLASH (Hamburg, Germany, 2005, [31, 32]), operating in the XUV regime, and the Linac Coherent Light Source, or LCLS (Stanford, USA, 2009, [33,34]) operating in the hard X-ray regime. The very first experiments performed at the LCLS will be the subject of this thesis, and the characteristics of this remarkable machine will be shortly described in detail. To date two other XUV and X-ray FELs have started their operations, FERMI (Trieste, Italy [35]) and SACLA (Kouto, Japan [36]), to be followed in the next few years by the European XFEL (Hamburg, Germany [37]) and the SwissFEL (Villigen, Switzerland [38]); the operation wavelengths and the brightness for these facilities are reported in Fig. 1.2.

Coming back to HDM studies, besides the penetration capabilities of the X-rays, the possibility of creating a hot dense plasma by heating a material with an X-ray laser also provides another extremely interesting feature: given that the main absorption process at these wavelengths is the direct ionization of core electrons by a single photon, that is a simple atomic physics process, the modelling of the laser absorption and its relationship with the ionization and energy balance are greatly simplified, if compared with the optical case. This is an enormous advantage when modelling HDM, where the standard equation of state (EOS) models linking the deposited energy and the thermodynamic quantities of the plasma are usually outside their domain of applicability.

In this work I will show that coupling the experimental results from a laser-solid interaction experiment at an X-ray FEL with detailed time-dependent atomic kinetics calculations for the laser absorption and plasma

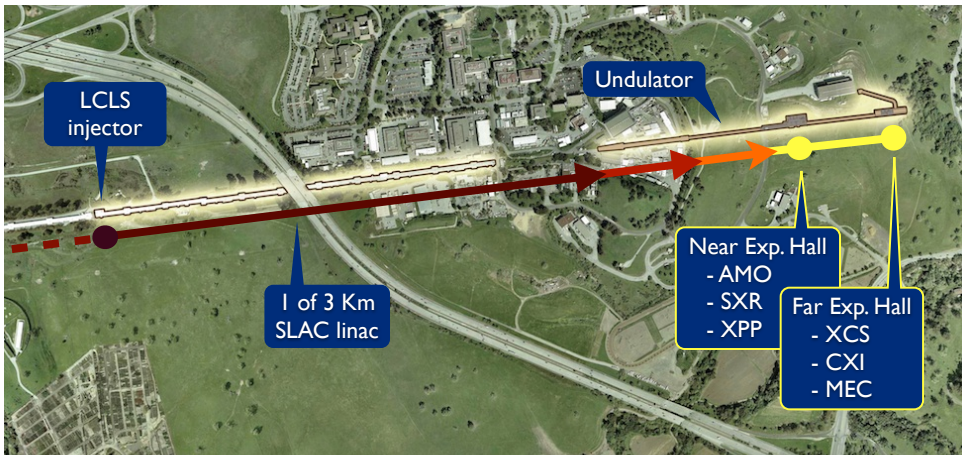

Figure 1.3: Aerial view of the Linac Coherent Light Source, showing the main parts of the system and the location of the six experimental end-stations. (Modified image. Original image credit: SLAC National Accelerator Laboratory)

evolution is a very efficient way to unveil the dynamics governing plasmas in the HDM regime: I thus next briefly describe the details of the two scientific tools at the basis of this thesis, that is the LCLS laser, and the code SCFLY.

1.2.1 The Linac Coherent Light Source (LCLS)

The Linac Coherent Light Source is the world's first true hard X-ray laser, having observed lasing at 1.5 Å for the first time in April 2009 [34]. An aerial view of the machine, located in Stanford, California, at the SLAC National Accelerator Laboratory, including its main components and a list of scientific end-stations, is shown in Fig. 1.3.

The last kilometre of the old SLAC linac has been modified to include a high brightness electron injector and two bunch compressors, so that a high quality, short electron bunch (10∼100 fs), with an energy between 3.5 and 15 GeV and a repetition rate up to 120 Hz, can be injected in a 132 m undulator, with $\lambda_u = 3$ cm and $K_0 = 3.5$; here the X-ray lasing reaches the saturation

regime, producing by SASE process short pulses of X-rays, with a photon energy between 280 eV and 10 keV, and a pulse energy between 0.1 and 1 mJ depending on duration. The interested reader can find more detailed technical information on the LCLS in the conceptual design report [39].

The X rays produced in the FEL are delivered to one of six end-stations, or instruments, each one providing the users with different diagnostics and photon energy ranges, suitable for different kinds of scientific investigation. A typical experiment consists of five 12-hour shifts of beamtime at one of these endstations, with the facility operating two experiments and two instruments non-stop for five days a week. Importantly, the time required to change the operating X-ray photon energy, by varying the energy of the electron beam, is of the order of just a few minutes, so that a scan in wavelength can be easily performed in a single shift.

Two of the instruments, AMO (Atomic, Molecular & Optical Science) and SXR (Soft X-ray Material Science), are operated at the lowest photon energies available, between 280 eV and 2 keV; the remaining four, XPP (X-ray Pump Probe), XCS (X-ray Correlation Spectroscopy), CXI (Coherent X-ray Imaging) and MEC (Matter in Extreme Conditions), are operated in the range 4-10 keV.

The instrument specifically intended for WDM/HDM studies is MEC, where the X-rays are primarily used as a fast probe for optical laser generated plasmas. However, as it will become clear, for the kind of experiment discussed in this thesis, the lower photon energies available at the soft X-ray end-stations are required, in order to pump/probe the simple structured elements having empty N shells in the ground state configuration ($Z<18$), that are best fit for the spectroscopic studies described. Both the experiment described in this thesis, and a very recent follow-up experiment, were thus

performed at the SXR instrument.

SXR can provide X-ray pulses at the wavelengths reported above, with a pulse energy of ∼1 mJ and duration between 60 and 200 fs, or a pulse energy of 0.1 mJ and duration of less than 10 fs, in a single pulse mode or at a repetition rate up to 120 Hz. The fractional bandwidth of the pulse is ∼0.5%. The unfocused beam has a diameter of 1 mm, and can be focused to a nominal spot size of 2 μm by a pair of Kirkpatrick-Baez mirrors (KBO) [40]. The total intensity that can be delivered onto the target is thus more than 10^{17} W·cm^{-2}, an intensity regime that was previously the domain of the optical lasers.

1.2.2 Modelling the laser-matter interaction: SCFLY

If we assume that the LCLS pulse, at 1 keV and 1 mJ, can deposit its 10^{12} X-ray photons in a micrometer size volume of a target, in a time corresponding to ∼100 fs, for a material with an ion density of ∼10^{23} cm^{-3} there will be on average ∼10 absorbed photons per atom. It is then reasonable to expect that the plasma's ionization and temperature will change dramatically in a very short time, so that a time dependent modelling of the evolution of the system is vital to correctly understand any experimental measurement depending on these thermodynamic quantities. The tool I used for this purpose is a modified version of the SCFLY code [41].

SCFLY is a collisional-radiative code based on the widely used FLYCHK simulation tool [42] (which can be run via a web-based interface [43]), but featuring several improvements that make it suitable to model X-ray FEL related problems. Both codes are zero-dimensional codes, using an escape factor formalism [44] to include the effects of the opacity.

As in FLYCHK, the code uses super-configurations, that is atomic states

given in term of the occupation of energy levels described by the principal quantum number, in order to calculate the populations and charge states distribution in non-LTE (Local Thermal Equilibrium) conditions, but it features an extended number of superconfigurations. For example it includes states with two electrons excited from the K-shell, that become relevant when a sample interacts with high-intensity X-rays (as well as the following chapters, see for example [45]). Another improvement is the inclusion of line profiles for the determination of photoabsorption rates, allowing for the modelling of the off-resonance pumping of atomic transitions by the high-intensity finite-bandwidth X-ray pump.

The most relevant difference with FLYCHK, for the work described here, is that SCFLY includes a self consistent calculation of the temperature evolution of the plasma, due to the trivial relationship between the absorption mechanism (single photon absorption) and the variation of the internal energy of the system (the change in energy of the excited ion) that pertains to the absorption of X-rays. This means that SCFLY can be used as a tool to actually simulate the plasma evolution, rather than as a post-processor or to fit spectroscopic data to the emission corresponding to certain user-defined average density and temperature conditions, which is the customary way in which FLYCHK is used. The time-dependent non-LTE calculation is performed according to the following procedure.

The initial electron density $n(0)$, temperature $T(0)$, and population array $N_i(0)$ (i.e. the ground state configuration of the ions for a cold sample), corresponding to the conditions of the sample before switching on the X-ray laser, are provided by the user as an input, together with an X-ray pulse temporal and spectral profile $I(\omega, t)$. The quantities at a time $t+dt$ are then determined as a function of the quantities at time t; having determined the

number of available states $n_{eq}[n(t), T(t)]$ depending on pressure ionization (see §4), the rates of all the possible transitions (bound-bound and bound-free, collisional, radiative, or Auger) between configurations, that is $R_{ij}(t) = f(n(t), T(t), I(t))$, are calculated, and the program solves the n_{eq} coupled rate equations given by

$$\frac{N_i(t+dt) - N_i(t)}{dt} = \sum_{j \neq i}^{n_{eq}} R_{ij}(t) N_j(t) - \sum_{j \neq i}^{n_{eq}} R_{ji}(t) N_i(t) \qquad (1.3)$$

where R_{ij} denotes a transition from the configuration j to the configuration i. Solving Eq. (1.3) provides the populations $N_i(t+dt)$, and the electron density $n(t+dt) = \sum N_i(t+dt) z_i$, with z_i ionization degree of the configuration i. At this point, knowing the rates and energies ϵ_{ij} exchanged for every single transition, including the radiative transitions responsible for the laser absorption, the temperature change of the system can be calculated in terms of the energy transfer rates ($dE/dt = \sum R_{ij} \epsilon_{ij} N_j$), and it is simply given by[2]

$$\frac{3}{2} n(t+dt) k_B T(t+dt) = \frac{3}{2} n(t) k_B T(t) + \frac{dE}{dt} dt - \Delta E_{int} \qquad (1.4)$$

where ΔE_{int} is the energy stored in the ion system as excitation/ionization (readily obtained by summing the energies associated with each super-configuration, and the variation in their populations between t and $t + dt$). It is thus possible, evolving the system from the initial conditions, to get a complete time evolution of all the relevant quantities as the laser is absorbed. Eq. (1.4) assumes instantaneous thermalization of the electrons, an assumption that will be discussed in §5.2.1.

The above discussion applies for systems at a constant mass density and ion temperature, which is the relevant case for the problems discussed in the

[2]The dt in Eq. (1.3) and Eq. (1.4) are actually different in the code, due to the much finer time grid usually required to solve the rate equations, but the actual algorithm used is beyond the scope of the present discussion.

thesis. SCFLY is however able to handle, in the same fashion, expanding systems as well as systems with the same ion and electron temperature.

1.3 Structure of the thesis

This thesis is not meant to be a detailed report of all the experimental and theoretical work performed by the author in the past three years, but will rather focus, on the one hand, on the development of a procedure – based on non-LTE simulations – to describe and understand the results of a laser-solid experiment performed at an X-ray FEL and, on the other hand, on the scientific results this method has produced so far. The work is structured in six chapters, reflecting the intent just declared.

Chapter 1 is an introductory discussion which pinpoints the underlying research area, that is HDM, and the scientific tools, that is an X-ray FEL and a non-LTE code, that represent the basis of the work described through the thesis. It includes this structural description, and an outline of the author's contribution to the topics presented.

Chapter 2 presents a preliminary work, aimed to test the simulation capabilities of the SCFLY code for X-ray FEL problems. It describes the modelling of the first experiment performed at the LCLS, where the X-rays interact with a Ne gas, a simplified problem that allows one to identify the unique features of the high intensity X-ray laser-matter interaction at an atomic level, by quenching the collisional physics, before undertaking the more difficult task of describing the complex physics of HDM in the same pump conditions. The results from this chapter were published in *High Energy Density Physics* in 2011 [46].

Chapter 3 and 4 are the core of the work presented. They describe the results of the first experiment performed at the LCLS where the X-rays

interact with a solid, a thin Al foil, to produce HDM by isochoric heating of the sample.

Chapter 3 describes the experimental data obtained by K_α spectroscopy of the Al sample, their interpretation, and the details on the evolution of the system to the HDM regime. The heating process and the spectroscopy emission are explained by detailed space and time dependent SCFLY simulations, and the role of the collisional physics is underlined. The results from this chapter were published in *Nature* in 2012 [1].

Chapter 4 focuses on a particular aspect of the same experiment, that is the first measurement of continuum lowering effects with charge state resolution in a HDM plasma. It includes a theoretical description of continuum lowering and a discussion on the experimental technique and the results of the SCFLY simulations. This work has challenged the most used and accepted theoretical description of the effect, and the results presented here have been published in *Physical Review Letters* in 2012 [2].

Chapter 5 presents a more detailed discussion of the approximations used and the physical characteristic of the experimental system that affect the SCFLY simulations reported in the previous chapters. The stress is on the identification of potential issues or improvements in the simulation and experimental framework for HDM studies presented.

Finally, Chapter 6 includes a summary of the work presented, the conclusions, and mentions related and future work on the topics discussed in the manuscript.

1.4 Author contribution

Work of the scale described in this thesis is by its nature a collaborative effort. However, the key and distinct contributions made by the author can

be identified, and for the sake of clarity and proper attribution we outline them here, as well as the crucial role of collaborators.

All of the SCFLY simulations described in this thesis, and the modelling work described in Chapter 2 and 5, are due to the author.

Although the author actively participated in several experiments in the past few years (four of which at the LCLS), the experiment on Al described in the central chapters of this thesis was actually performed before the start of his D.Phil. – that is, the author was not involved in the setup nor in the data collection – and includes contributions by all of the authors listed in Ref. [1, 2]. In particular the data processing described in §3.1.1 was performed by the collaborators from the Lawrence Berkeley National Laboratory (US).

However, apart from the detailed subdivision of the practical work (simulations, experiment, etc.), the interpretation of the results, driven by the author's simulations, discussed in Chapter 3 is to be equally attributed to the author, to Dr Vinko, and to Prof. Wark; should one want to stress which idea is whose, that would not only be quite a difficult task, but would probably also end up in an unfair attribution in one way or another. A relevant contribution to the discussion was also given by R. W. Lee and H.-K. Chung.

The work described in Chapter 4 is mainly due to the author, with all of the simulations and the detalied analysis performed by him, even if once again with vital contributions by Dr. Vinko, Prof. Wark and H.-K. Chung.

H.-K. Chung and R.W. Lee are responsible for the development of the main SCFLY code, whilst the important modifications described in §4.3.1, §5.2.1 and §6.4 are however due to the author.

CHAPTER 2

Reduced problem: X-ray laser interacting with a gas

With the advent of the 4th generation X-ray sources, led by the LCLS, a completely new regime of high-intensity laser-plasma interaction has become accessible. The $>10^{17}$ W·cm^{-2} X-ray femtosecond pulse of the LCLS is able to induce in a sample single photon atomic transitions with a pump rate comparable with those of the typical competing processes (e.g. Auger decays), a condition never observed before in the X-ray regime. It is thus important to verify that any simulation tool, even if based on very well known models, is able to reproduce experimental data revealing the basic features of the new regime.

As usual in physics, when describing a complex system, it is also convenient to consider first a simplified problem, by quenching some of the

processes characterizing the complex one. Here, before describing and modelling the features of the high intensity X-ray interaction with a solid density plasma, I will describe the interaction of the LCLS pulse with a gas, where the low density of the target allows one to virtually switch off the collisional physics and, at the same time, the high density effects which will be the subject of the Chapter 4 of this thesis.

By modelling published experimental data in this regime with SCFLY, it is thus possible to test the ability of the code to model the interaction at a fundamental, atomic level, and to improve the understanding of the laser absorption process that underlies the complex plasma evolution in HDM conditions, which is the ultimate subject of this work.

2.1 Young's experiment on Neon

One of the first experiments performed at the LCLS (L.Young *et al.* [47], hereafter referred to as LY2010) measured the charge state distribution (CSD) produced in a Ne gas when irradiated by the high intensity X-ray pulse of the FEL.

The experiment was performed at the AMO instrument, where the X-ray pulse was focused to an estimated $1{\times}2$ μm^2 focal spot on a Ne gas-jet, and the charge states produced were detected by an ion time-of-flight spectrometer. The nominal X-ray pulse energy used was 2.4 mJ, with a pulse duration varying in the order of 100 fs, depending on the wavelength. This energy and focal size correspond to a photon flux of the order of 10^5 Å^{-2} per pulse on the target, so that a single atom is expected to absorb several photons during the interaction.

The sample was irradiated at three different photon energies, 800, 1050, and 2000 eV, corresponding to three different expected regimes of interac-

tion. At 800 eV the photon energy is below the K-edge of the neutral Ne atom (870 eV), so that the laser absorption is expected to proceed via a sequential single photon ionization of the eight L-shell electrons of the Ne (the L-edge energies vary between 20 eV for the neutral atom and 240 eV for the 8^+ ion). Conversely 1050 eV is above the K-edge of ions up to the 4^+, so that the first charge states are preferentially ionized by K-shell photoabsorption (due to the higher cross-section with respect to the L-shell absorption), followed by fast Auger decays. Finally at 2000 eV the photons have enough energy to fully strip the ions by sequential K-shell photoionization.

As collisional ionization and recombination processes are expected to be negligible in the low-density gas target, that is to say, the CSD cannot vary after the laser has switched off, the ion spectrometer's data represent a CSD purely determined by the photoabsorption processes typical of the X-ray interaction with the atoms. Electron spectroscopy diagnostics were also used in order to distinguish between different atomic processes, leading to different energies of the ejected electrons. The work by Young and collaborators thus represents the first experimental observation of the mechanisms underlying the new X-ray laser-matter interaction regime, at the atomic level.

2.1.1 Experimental results

The results from the ion spectroscopy measurements reported in LY2010, in the three regimes explored in the experiment, are shown in Fig. 2.1, together with the simulations presented in the same work, and the SCFLY simulations I will describe in the next section.

The LY2010 simulations are based on a rate equations atomic model by Rohringer and Santra [48], including first and second order photoionization processes and Auger decays, subsequently modified to include the effects of

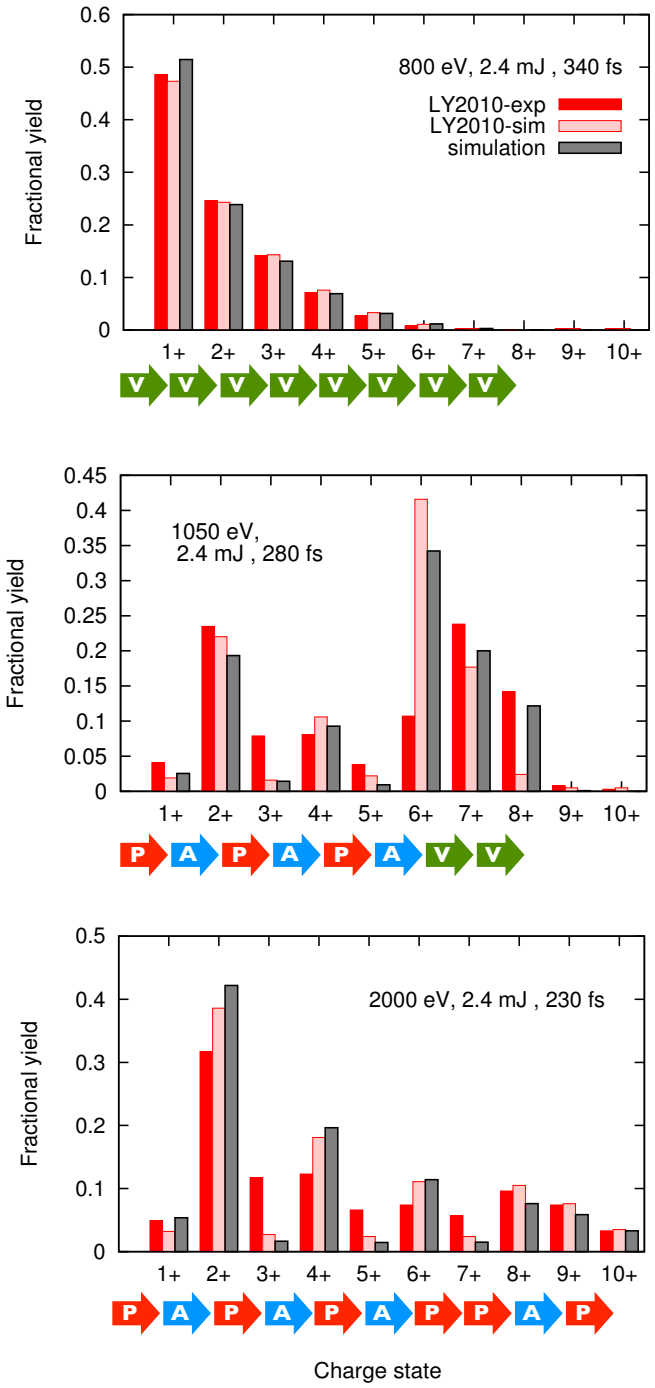

Figure 2.1: Experimental data and simulations from [47] (red and light red), compared with the SCFLY simulations [46] performed by the author (grey). The predominant expected ionization channels, following the nomenclature in [47, 48], are shown below the plots: P refers to K-shell photoionization, A to Auger decay, and V to L-shell (or Valence) photoionization.

the spatial profile of the pumping laser.

In keeping with the nomenclature used in [47, 48], the arrows below the plots in Fig. 2.1 also show the predominant ionization channels, expected to lead to the formation of highly ionized neon in the three cases. Here V refers to the photoionization of a valence (or L-shell) electron, P to the photoionization of a K-shell electron, and finally A refers to an Auger process.

The figure shows an excellent agreement between the data obtained at 800 eV and the LY2010 simulations, indicating that the simple sequential single-photon absorption process described by the VVV... chain is an accurate description of the evolution of the system when pumped below the K-edge. The situation is slightly different when pumping above the edge. Here the experimental data show an even-odd asymmetry of the CSD, explained by the fast depopulation of the odd charge states reached by a P process, due to the femtosecond timescales of the subsequent Auger decays. This is a peculiar feature of the interaction of atomic samples with an X-ray FEL. However, even if the LY2010 simulations for the 1050 and 2000 eV cases can reproduce this general trend, they clearly overestimate the odd-even asymmetry for states ionized three or more times, and there is a notable discrepancy in the case of the charge state 6^+ at 1050 eV, the highest charge state that can be reached by a PAP... chain at this wavelength, suggesting that some physics is missing in the model.

The overestimation of the odd-even asymmetry was explained by the authors of LY2010 in terms of the lack in their model of double-Auger [49] and shake-off [50] processes. As it is known experimentally [50] that $\sim$25% of the singly photoionized Ne atoms evolve into a 3^+ charge state, this means that a secondary chain PXX-PAP... can exist (where XX can be a shake-off followed by an Auger decay, or a double-Auger decay) that tends to coun-

terbalance the effect of the main PAP-APA... chain in terms of depopulating the odd/even states starting from the 3^+. The importance of the inclusion of these effects in the simulations, in order to correctly reproduce the CSD, was indeed proved in a subsequent work [51].

A similar impact on the CSD can be in principle attributed to an underestimation of the process PPA (i.e. PXX=PPA in the above discussion), that is the absorption of two photons to generate a hollow atom, followed by an Auger decay, important when the intensity is high enough that the photoabsorption rates are faster than the Auger rates. The PPA process can be in fact enhanced by the characteristic features of a SASE pulse, that has a structure with randomly distributed high intensity spikes [52], neglected in the LY2010 calculations assuming a Gaussian temporal profile. This explanation was however dismissed by the authors, on the basis of detailed simulations including SASE effects performed in [48].

The problem of the population of the 6^+ ions when pumping at 1050 eV was instead solved more recently [53] (later than the publications of the SCFLY results discussed in this chapter), and can be explained in terms of resonant pumping of a 1s→4p transition in the 6^+ ions, followed by an Auger decay depleting the 6^+ charge state in favour of the 7^+. The model used in LY2010 considered only transitions between states with populated K and L shells, but ignored higher energy orbitals, so that this effect was not reproduced. How this resonance affects the SCFLY simulations will be described in the next section.

2.2 SCFLY simulations

I performed detailed atomic-kinetics simulations for the LY2010 experiment by using SCFLY, in order to test the predictive capabilities of the code in

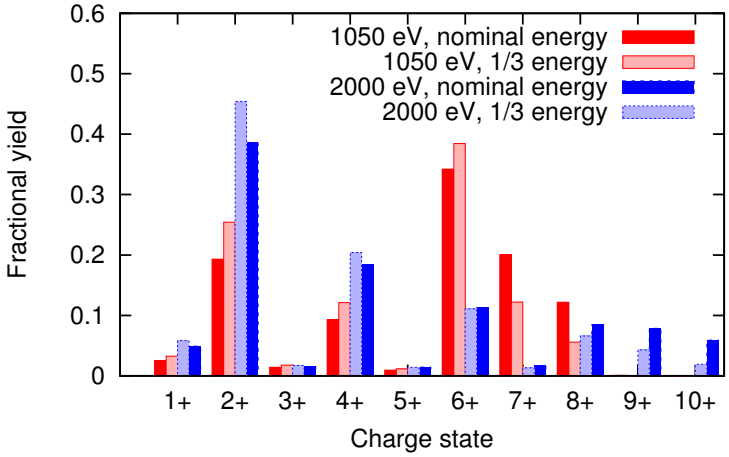

Figure 2.2: Effect of a reduction from the nominal pump energy for the simulations of the above-edge cases.

the newly available experimental conditions.

As the CSD in the Ne gas will vary spatially with the X-ray intensity evolution experienced locally, a set of 21 simulations was performed, spanning four orders of magnitude in the maximum intensity for the X-ray drive pulse; the results from each of these simulations were then weighted and integrated according to an elliptical Gaussian beam profile with axis ratio 1:2, as reported in [47], in the section of the interaction zone visible to the ion spectrometer, limited in the experiment to 1 mm by use of a slit. The axis of the waist of the beam were inferred by the measurements in [47], reporting a 3 μm^2 spot at a photon energy of 870 eV, assumed here to also hold for the 800 and 1050 eV cases, and a 2.5 μm^2 spot at 2000 eV.

The temporal profile of the intensity was assumed Gaussian, in keeping with the LY2010 calculations, which neglects the effects of the intensity spikes that characterize the pulses produced by SASE, an assumption justified by the aforementioned calculations by Rohringer and Santra [48].

The pulse energy used in the simulation at 800 eV is reduced by a factor of 2.5 with respect to the nominal 2.4 mJ, giving a fluence which is in

agreement within 20% of the value derived in LY2010. However the best fit to the data for the two simulations at 1050 and 2000 eV have energies that are much closer to the nominal values. A possible explanation for this is reported in [46], and involves pulse duration considerations, but is omitted here, as deemed irrelevant to the present discussion, since it was found that tuning the pulse energy within a factor of 3 doesn't show a qualitative impact on the simulated CSDs for the above edge cases (see Fig. 2.2).

The ion density used in the SCFLY simulations, not specified in LY2010, nor important for their atomic calculations, but needed as a fundamental parameter for the collisional-radiative calculations discussed here, was arbitrarily set to 10^{18} cm^{-3}. This value was chosen because it leads to a slightly, definitely not substantial, better agreement with some of the data, still remaining low enough as not to perturb the CSD because of collisional effects, as I will show later.

The results of the simulations are compared with the LY2010 experimental and theoretical results in Fig. 2.1, whilst the time evolution of the space integrated CSD is shown in Fig. 2.3. The latter shows how, after the rapid evolution of the CSD within the X-ray pulse, the populations tend to a constant value, which is not perturbed by collisions, and is the one that is detected by the ion spectrometer after the system expands at later times. As can be seen in Fig. 2.1 the SCFLY results are not dissimilar from the theoretical results in LY2010. The code does a good job in reproducing the experimental data at 800 eV, but as before it overestimates the odd-even asymmetry of the CSD for the two above-edge cases. Still it is found able to capture the basic features of the interaction due to the VVV... and PAP... chains in the different pumping regimes, which was the main purpose of this test work.

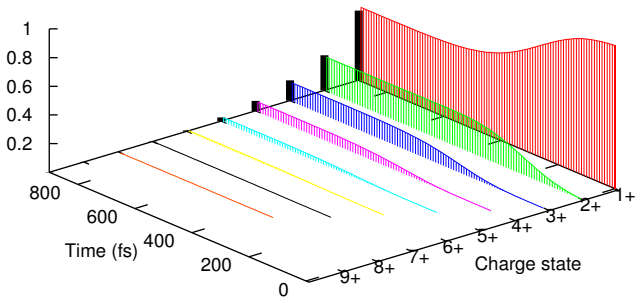

800 eV, 340 fs Gaussian pulse peaked at t=350 fs

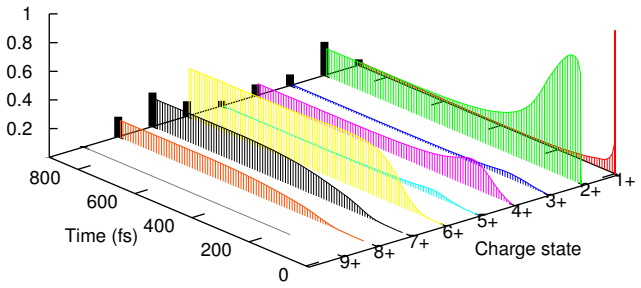

1050 eV, 280 fs Gaussian pulse peaked at t=350 fs

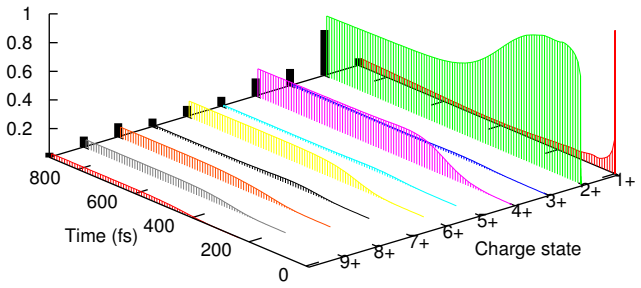

2000 eV, 230 fs Gaussian pulse peaked at t=350 fs

Figure 2.3: SCFLY simulations of the time evolution of the space-integrated CSD in Ne. The black histogram on the background represents the experimental CSD. The peak of the LCLS pulse occurs in all of the simulations at 350 fs.

Although as in LY2010 the overestimation of the odd-even alternation can be attributed to neglecting the aforementioned double-Auger and shake-off processes in SCFLY, the poor reproduction of the 6^+ feature, still persisting in the SCFLY simulations, deserves some additional explanation. In fact the treatment of resonant pumping, as well as the relevant superconfigurations involved in the 1s→4p transition responsible for the depletion of the 6^+ charge state, are indeed included in SCFLY, so that it is somehow surprising that the results resemble those neglecting this effect.

The failure in reproducing the 6^+ feature in the SCFLY simulations is due to two concurrent issues. First, in the atomic data on Ne used as an input in SCFLY the energy of the relevant 1s→4p transition was reported to be 1076.3 eV, rather than 1053.5 eV as reported in [53] (a 2% overestimation); second, as the atomic processes considered relevant at the time of the calculations (V, A and P) are not affected by the bandwidth of the laser in the experimental conditions, a simple flat-top spectrum with a width of 4 eV was assumed for the FEL, which doesn't overlap with the line profile of the 1s→4p transition. Given that the stress here is on testing the code before using it in HDM conditions, rather than an accurate description of the particular atomic physics experiment, in the following I will ignore, where possible, the particular aspect of the 6+ feature, by keeping in mind that in the work described in the following chapters both the calculation of the atomic energies used as an input was improved (H.-K. Chung – private communication) and the spectrum of the FEL was modelled by a smoother Gaussian profile, that allows for a better modelling of the off-resonance pumping of bound-bound transitions. However, in order to provide a feeling for the impact of the resonance on the SCFLY simulations, two calculations performed using the energy quoted by [53] for the transition just discussed,

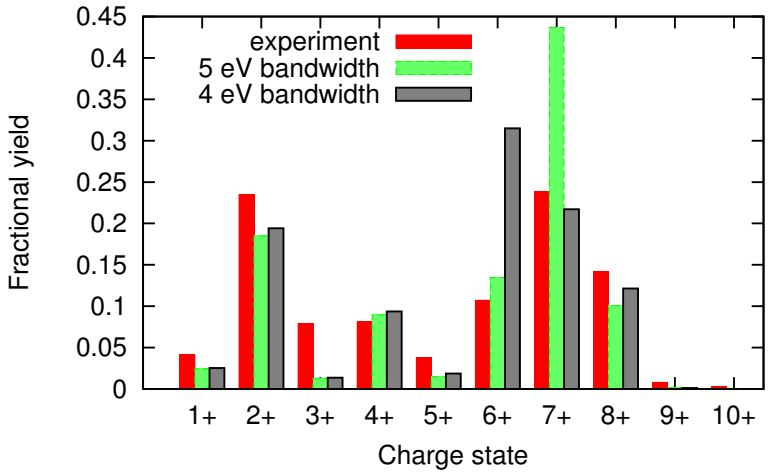

Figure 2.4: Comparison of the experimental data at 1050 eV pumping with SCFLY simulations with an energy correction for the resonance 1s-4p in charge state 6^+. Both the flat-top FEL spectrum used in the old simulations with a bandwidth of 4 eV and an increased bandwidth of 5 eV (flat-top) were used in the new simulations and are compared in the plot.

with bandwidths of the FEL corresponding to 4 and 5 eV (that is, at maximum photon energies in the spectrum of 1052 and 1052.5 eV respectively) are shown in Fig. 2.4. Even if the 5 eV bandwidth simulation now overestimates the population of the state 7^+, the calculation proves that even a partial overlap of the FEL spectrum with the resonance is able at least to reproduce the correct alternation of the population yields even for the 1050 eV case.

2.2.1 Local evolution

Even if the data provide information on the atomic processes occurring in the system, it is important to bear in mind that the physical processes, such as the PAP... or VVV... chains, are actually local processes, determined by the local evolution of the radiation field and plasma environment (the latter being more relevant when the effects of collisions will become detectable).

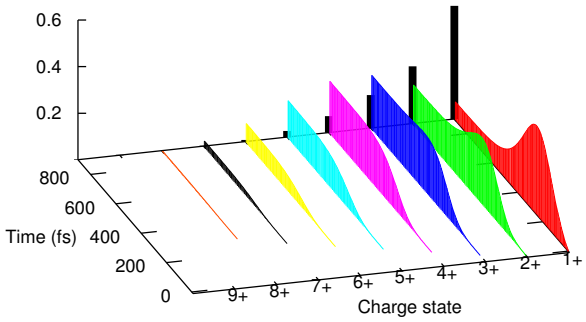

800 eV, 340 fs Gaussian pulse peaked at t=350 fs

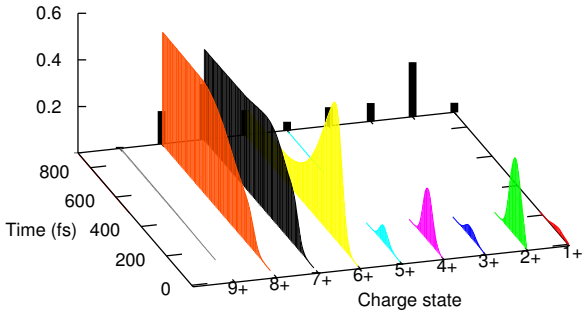

1050 eV, 280 fs Gaussian pulse peaked at t=350 fs

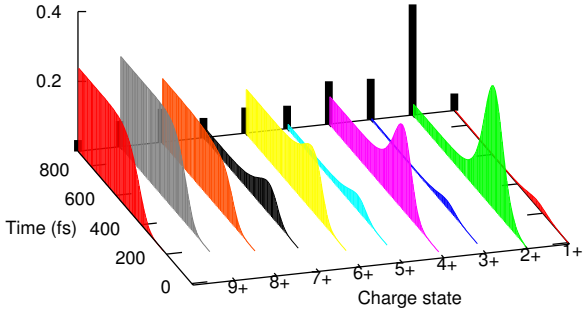

2000 eV, 230 fs Gaussian pulse peaked at t=350 fs

Figure 2.5: Single intensity SCFLY simulations of the time evolution of the CSD. The simulation plotted corresponds to the one at peak intensity of the X-rays, modelling the local evolution of the Ne gas in the focal point. The black histogram on the background represents the experimental CSD. The peak of the LCLS pulse occurs in all of the simulations at 350 fs.

In order to understand the importance of considering the effects of the spatial profile when modelling the plasma evolution, the CSD evolution for the simulation at the peak intensity, that corresponds to the local evolution of the plasma in the focal point, is shown in Fig. 2.5. By comparing this with Fig. 2.3 it can be seen that the measured CSD, roughly reproduced by the space integrated simulations, is not reproduced locally even in the simple case of 800 eV pumping, where the local simulation doesn't even present a monotonically decreasing CSD. The simulations for the two above-edge cases show instead a strong depletion of the lower charge states, in clear disagreement with the experimental data, whilst the three CSDs peak respectively at 3^+, 8^+ and 9^+ rather than at 1^+, 6^+ and 2^+ in the space integrated simulations. Note that the peak intensity of the Gaussian beam profile would not be too dissimilar from the average intensity experienced through an assumed uniform sample. The experimentally observed CSD is thus indeed determined by the contribution of different absorption histories occurring though the whole interaction volume, rather than by its average behaviour. The effect of neglecting contributions by zones experiencing a peak intensity corresponding to less than 2% of the one at the focus, is shown in Fig. 2.6 for a simulation at 1050 eV.

Because of the point just discussed the degree of accuracy to which the experimental data can be reproduced is probably limited by the knowledge of how the energy of the X-ray pulse is distributed into the different intensities, or more physically speaking, into the transverse spatial structure of the pulse. I will show in §5.1.1 that even the assumption of a Gaussian spatial profile of the LCLS is not accurate enough to reproduce the experimental data described in the next chapters.

As mentioned before, other than the atomic processes described here,

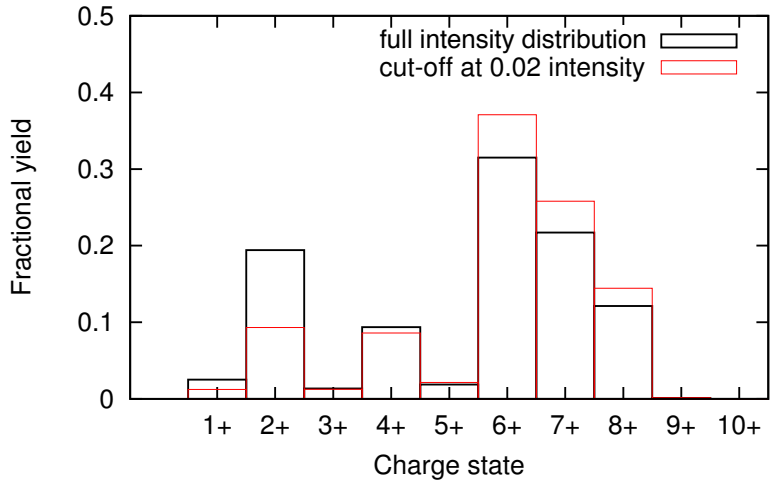

Figure 2.6: Simulation for the 1050 eV case using the full intensity distribution compared with a simulation excluding the contribution of the zones at an intensity lower than 2% of the focal intensity. The complete simulations include intensities as low as 3×10^{-4} of the focal value.

also the thermodynamic quantities, like the temperature, will evolve locally. As SCFLY can keep track of the energy balance of the system while the rate equations for the populations are solved, it calculates a self consistent temperature evolution for the different zones of plasma experiencing different laser intensities, provided that the assumption of instantaneous thermalization of the electrons is valid. Of course this is clearly not true for the LY2010 conditions, where, as an example, the collisional energy loss rate for fast ($\sim$1 keV) Auger electrons colliding with the slower photoelectrons can be estimated [54] to be of the order of a few GHz, for the assumed density of 10^{18} cm^{-3}, so that the electron system cannot thermalize during the interaction with the laser. The instantaneous thermalization will be instead a reasonable assumption when modelling the solid density plasmas described later, where the density, and thus the collisional rates, will be higher by five orders of magnitude.

Nevertheless, the calculated temperature for the LY2010 case is still

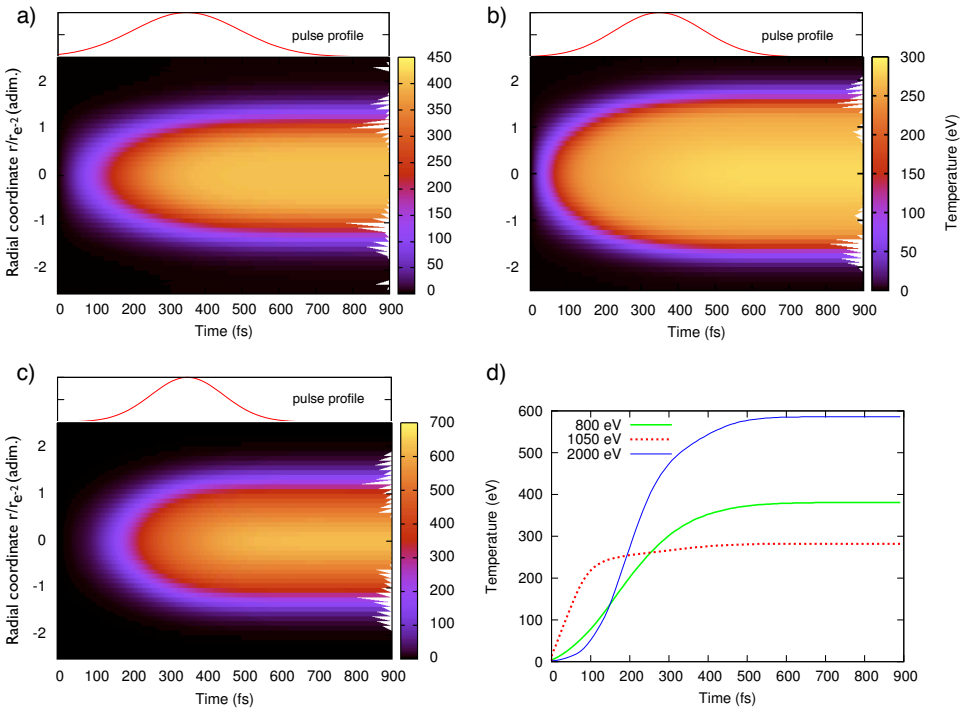

Figure 2.7: Calculated temporal evolution of the radial temperature profiles in the focal plane, when pumping at a) 800 eV, b) 1050 eV, and c) 2000 eV. The plot in d) shows the local evolution in the point of peak intensity (lineout at a spatial coordinate of 0 in the other plots).

representative of the part of the absorbed laser energy that is stored within the free electrons, even if the system itself is not thermalized in the real case. Regarding the temperature with this meaning, Fig. 2.7 shows the temporal evolution of the radial temperature profiles in the focal plane, along one of the axis of the elliptical beam. It is interesting to compare the maximum temperature calculated in the three cases. This can be done by focusing on a particular point of the plasma, as in the plot d) of the figure, restricting the attention on the focal point. The plot shows that driving the system at photon energies below the K-edge (800 eV) can lead to temperatures which are higher than those reached pumping just above it (1050 eV), in spite of the well known opposite relationship between the absorption cross-

sections. This can be readily explained by comparing the temperature local evolution with the CSD local evolution shown in Fig. 2.5. Looking at the CSD, due to the high cross-section of the PA process, when pumping at 1050 eV the charge states up to 5^+ are depleted well before the peak of the X-ray pulse, whilst when pumping at 800 eV those charge states remain predominant throughout the pulse. At 1050 eV this corresponds to a sudden increase in temperature, followed by a plateau at a time corresponding to the depletion of the lower charge states, whilst at 800 eV the temperature increases more slowly, but during the whole duration of the X-ray pulse. The reason is that after the gas is completely ionized up to the 6^+ in the 1050 eV case, the laser absorption can only proceed via V processes, that although generating electrons with a kinetic energy very similar to that of the Auger electrons from the lowest charge states ($\sim$800 eV), is far less efficient than the P process. The few electrons produced by V cannot thus affect the temperature of the much larger number of electrons produced earlier by the PAP... chain. Note also that for each Auger electron a much lower energy K-shell photoelectron is produced in the PA process at 1050 eV, so that the temperature is lower than that obtained if all the electrons were emitted by V processes. Conversely at 800 eV the production of energetic photoelectrons, arising by the V process in the lowest charge states, takes place throughout the pulse at a constant cross section. Of course the 2000 eV case has a final temperature which is higher than both the cases discussed before, as the processes V, A and P all lead to the emission of high energetic electrons during the whole evolution, and the absorption rates are comparable to those at 800 eV.

For sake of completeness, the 6^+ resonance discussed earlier would slightly change the ratio between the temperatures (the simulation with a 5 eV band-

width in Fig. 2.4 still giving 300 eV as a final temperature, only slightly higher than the 280 eV in the former discussion), but the presented discussion, that would have held thoroughly if the LCLS was slightly detuned from the resonant energy of 1050 eV, is still a useful example of how the local physics, convoluted in the experimental data, can help in the understanding of the relationship between laser absorption and evolution of the plasma parameters.

2.2.2 Role of collisions

SCFLY uses the calculated instantaneous values of the electron density and temperature to compute at each time step the rates for collisional transitions between the atomic configurations, to be used in the rate equations model. Recalling the caveat about the validity of the temperature definition, as discussed before, SCFLY can thus be used to predict the ion density at which collisions between ions and the thermalized free electrons will start to play a significant role in the plasma evolution, and how they would affect the observed CSD.

In order to do so I performed simulations at different ion densities, in the range between 10^{13} and 10^{22} cm^{-3}. A comparison between three of these densities is shown in Fig. 2.8 for the simulation corresponding to the 2000 eV case. The plot shows how the simulation presented earlier, at a density of 10^{18} cm^{-3}, compares with the one at the lowest density considered, lower by five orders of magnitude, and the one at a density just ten times bigger. It is clear that whilst the impact of the density variation on the CSD is minimal by changing from the assumed density to much lower values, the collisions start to significantly perturb the CSD at the moderately higher density of 10^{19} cm^{-3}. The main effect observed on the CSD is the reduction of the even-

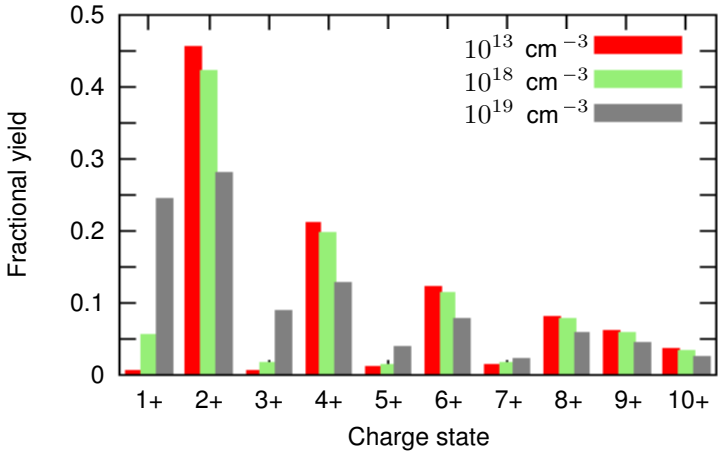

Figure 2.8: Ion density effect on the CSD for the 2000 eV simulation. Collisions are shown to have almost no effect on the results when the ion density is varied between 10^{13} and 10^{18} cm^{-3} (the value used in the simulations described earlier), while a further increase of one order of magnitude shows a significant impact on the CSD.

odd alternation as the density is increased, due to the increasing importance of collisional valence ionization (C process) as a competing process to the PA process, leading to the inverted odd-even alternation due to the chain CPAP.... rather than the chain PAPA... in a collisionless system.

Further insight is provided by the values of the rates calculated for the detailed transitions. In particular Fig. 2.9 shows, as a function of density, the relevant maximum collisional rates for the production of the 1^+ ions, normalized to the maximum photoabsorption rate, as well as the rates for the collisional production of a few odd charge states for the simulations at 2000 eV. As could have been probably guessed by looking at the CSD, the first plot shows that collisional ionization become as efficient as photoionization in creating singly ionized ions at densities around 10^{19} cm^{-3}, whilst recombination effects become important only at much higher densities. Moreover, from the second plot, it is clear that the collisional effects become important for higher charge states at progressively higher densities.

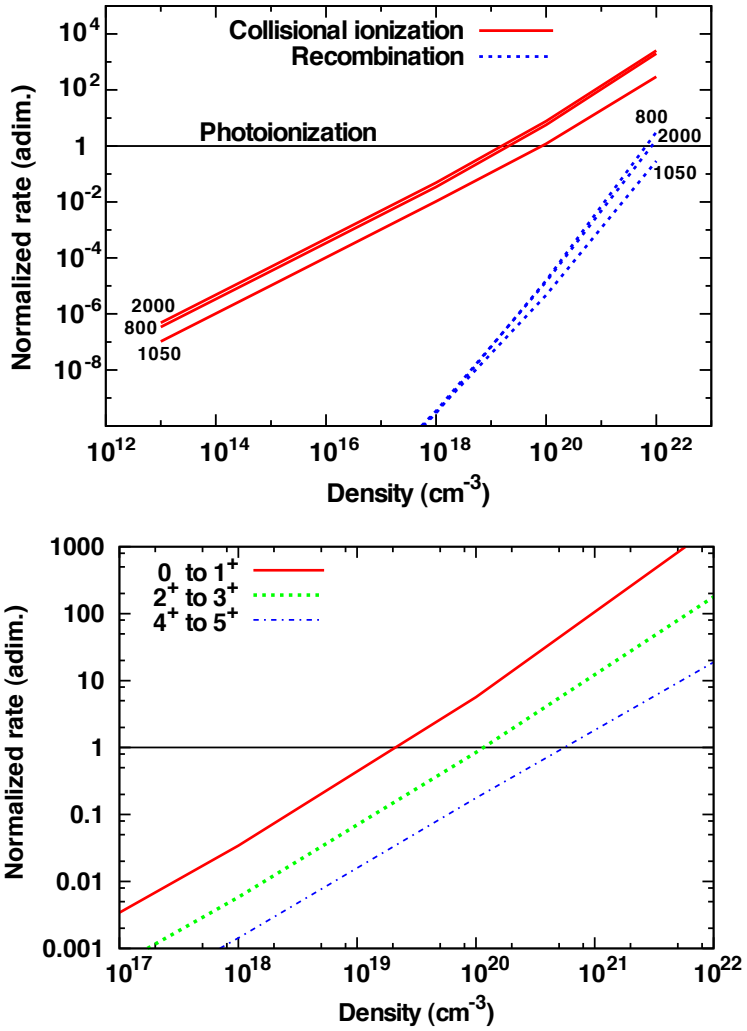

Figure 2.9: Collisional effects contributing to the population of the odd charge states. The plot on the top shows the maximum collisional rates in each peak intensity simulation, at different ion densities, for the production of the 1^+ ions by collisional ionization of neutrals and recombination from 2^+ states, normalized to the maximum photoionization rate from neutral. The bottom plot shows the collisional ionization rates for the production of the first three odd charge states, normalized to the same P rate, for the 2000 eV simulations.

It is interesting to note that even if, according to Fig. 2.9, the collisional production of 1^+ ions is relatively inefficient at the assumed density of 10^{18} cm^{-3}, if compared to photoionization, a visible effect on the 1^+ population is still observable in Fig. 2.8, due to the much longer lifetime of the ground state ions produced by collisional valence ionization, with respect to the short-lived excited ions produced by K-shell photoionization, leading to the creation of the 2^+ peak via a PA process. The simulations at this density were indeed chosen because of this effect, leading to a better reproduction of the experimental 1^+ peak, but without any relevant impact on the general trend. However because of the uncertainties on the laser intensity/profile, and the qualitative, rather than quantitative, overall agreement between simulations and experimental data, no definitive statement can be made about this being a real effect.

Finally, recalling the main purpose of this preliminary work, the disappearance of the odd-even alternation as the density increases, due to the collisional mix of the charge states, is of relevance for the solid density HDM systems I will discuss in the following chapters. As the ion density approaches values which are close to those typical of a solid ($\gtrsim 10^{22}$ cm^{-3}), Fig. 2.9 shows that the rates of collisional ionization are already well above those of photoionization for several charge states. It is thus reasonable to expect that the CSD at solid density will be strongly dominated by collisional effects, rather than by photoabsorption, and the experimental data won't show the typical odd-even alternation observed in a gas: I will show shortly that this is indeed correct. Moreover the secondary ionization mechanisms, double-Auger and shake-off, that are second order processes following a P event, but are still important in determining the CSD for the Ne gas, will become irrelevant in HDM conditions, where the P events won't strongly

themselves affect the CSD. This provides further confidence in the predictive capabilities of SCFLY – neglecting these effects – for these high density systems.

CHAPTER 3

Isochoric heating of Aluminium foils to the HDM regime

Having described and understood the atomic processes determining the laser absorption when LCLS interacts with a gaseous sample, and validated the SCFLY simulations in the new regime, it is now possible to use the same tools in order to understand how those processes will be affected by the collisional physics in a solid density target, and what kind of conditions can be actually achieved in these samples. In particular it is time to verify whether the laser absorption can indeed lead to the formation of a HDM plasma, with the desired temperatures of the order of 100 eV.

In the remaining chapters of this thesis I will describe the results of the first experiment in which the LCLS pulse interacts with a solid target, an Al foil [1, 2], and I will show the features of such interaction, explained by

comparing detailed SCFLY simulations with the experimental data. This chapter in particular will focus on the evolution of the system during the interaction with the X-rays, the spectroscopic diagnostic used in this work, and how this kind of experiment leads to the generation of exceptionally well characterized HDM samples.

3.1 The experiment

The experiment was performed at the SXR instrument of the LCLS, where the X-ray pulse was focused by means of KBOs on a 1 μm thick Al foil, at intensities on target corresponding to 10^{17} Wcm^{-2}. The pulse energy varied between 0.8 and 1.4 mJ, depending on the FEL wavelength, whilst the nominal pulse duration was kept constant at 80 fs.

The photon energy of the FEL was tuned between 1470 and 1830 eV, that is from below the resonant energy of a cold K_α transition, to an energy which is above the experimental threshold for the observation of He_α emission (see Fig. 3.2). Here I will mainly describe the results concerning the data for pump energies which are above the K-edge for the cold Al sample ($\sim$1560 eV), described in [1, 2], but the interested reader can find more information on the below-edge data in [55].

The main target diagnostic was K_α emission spectroscopy, detected by means of a flat crystal spectrometer (ADP 101), sensitive to the spectral range from 1460 to 1680 eV. The spectrometer monitored the emission emerging normally from the front of the target, whilst the laser pumped the system at 45° incidence, with each recorded spectrum corresponding to a single shot on a fresh portion of the target.

The spatial profile of the X-ray pulse was measured during the experiment by analysing imprints on a lead tungstate ($PbWO_4$) sample, using

the procedure described in [56]. From these measurements the effective area of the X-ray beam (determining the pulse fluence) was found to be $9.1 \pm 0.8\ \mu m^2$.

3.1.1 Data analysis technique

The LCLS features a data acquisition system (DAQ) recording on a shot-by-shot basis both the energy of the X-ray pulse (measured in a gas detector located upstream of the beamline) and the velocity of the electron beam in the undulator. The latter can be used in Eq. (1.2) to determine the wavelength of the X-rays for each shot (the accuracy of the conversion was verified to be better than 5 eV by transmission measurements of the attenuated beam on cold samples, around the K-edge of Al).

During the experiment the nominal X-ray photon energy was varied within the range of interest in 25 eV steps, and a minimum of 50 single-shot spectra were acquired for each FEL setting. The photon energy jitter for a given configuration can be inferred by the DAQ data, and was found to be $\gtrsim 10$ eV (FWHM) through the range of settings used in this work. This allows for the acquisition of data corresponding to a good sampling on the FEL photon energies, without the need for a time-expensive fine tuning of the parameters of the accelerator, that would be inconvenient for the limited time allocated for a given LCLS experiment.

The single-shot spectra were thus binned, according to the measured FEL photon energies, in 5 eV bins, with 75% of the bins resulting in a sum of 5 to 35 single spectra, obtaining a typical signal to noise ratio of the order of 10 or more. The effect of the spatial beam jitter, causing a small shift in the position of the spectral lines on the detector, was taken into account when summing the spectra, by forcing the overlap of the peaks from different

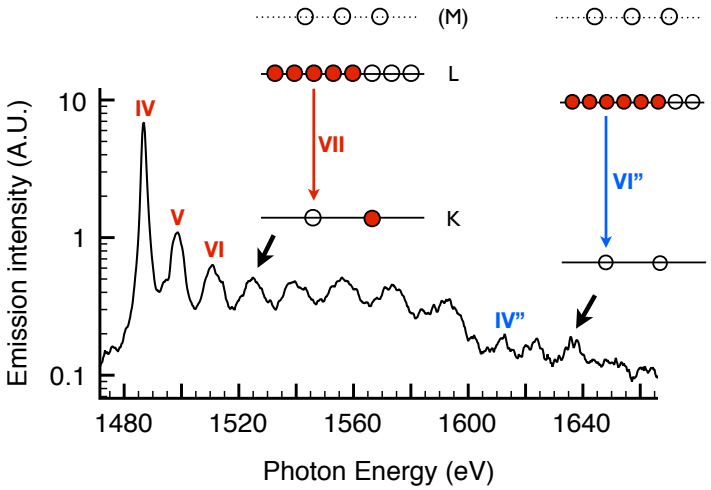

Figure 3.1: Experimental K_α satellites spectrum in Al, when pumped at 1800 eV. The plot shows the atomic process leading to emission of satellite K_α lines by ions with a different number of K and L-shell holes (the M-shell is part of the continuum in the experimental conditions), and the nomenclature used in the text for those lines.

shots. The spectra were then calibrated by using the K_α and K_β lines, as well as previously published energies for other observed lines [57, 58].

3.1.2 K-alpha spectroscopy

The typical spectral lines observed by the spectrometer are described in Fig. 3.1, showing the spectrum obtained by summing the 17 single-shot spectra in the bin corresponding to an FEL photon energy of 1800 ($\pm$2.5) eV.

As in the case of the Ne gas, the main laser absorption mechanism at this wavelength is the direct photoionization of a K-shell electron, with approximately 3% [59] of the ionized atoms emitting a K_α photon by radiative decay of an L-shell electron. As the sample is heated and ionized, the same process will occur in ions with an increasing number of holes in the L-shell, leading to the emission of different K_α lines (satellites) from ions with a different number of holes, as shown in Fig. 3.1. Moreover, given the high

intensity of the X-ray drive, leading to the formation of hollow atoms by PP process, a secondary K_α series can also be observed, arising from radiative decay of ions with an empty K-shell.

The nomenclature I will be using for the different lines is also shown in Fig. 3.1. The roman numerals for the main K_α series refer to the ionization state of the emitting ion (following the naming in [58]): as an example, IV refers to the K_α peak usually observed in cold Al samples, from 4^+ ions generated by ionization of a K-shell electron in a 3^+ ion (the ground state of metallic Al, having three delocalized electrons in the conduction band), whilst XI refers to the He_α line emitted by 11^+ ions. The lines emitted by hollow ions are instead named after the corresponding line of the main series: as an example, if removal of a K-shell electron from a 3+ ion can lead to emission of the line IV, the subsequent removal of the second K-shell electron in that ion (before any decay process has occurred) leads to the emission of the line IV".

3.1.3 Experimental results

A complete set of spectra for all of the investigated FEL photon energies is shown in Fig. 3.2. As the FEL photon energy is increased above the value corresponding to the K-edge of cold Al, more and more satellite lines are observed until, at the highest pumping photon energies, K_α emission from all of the charge states in the system is recorded, as well as emission from hollow atom states. The apparent persistency of line IX in the plot, as the FEL wavelength is varied, is due to the degeneracy of this line with the K_β emission from the cold material, emitted in the early stages of the plasma evolution and clearly visible when the emission of line IX is weak.

The plot also shows that when the photon energy of the laser is tuned

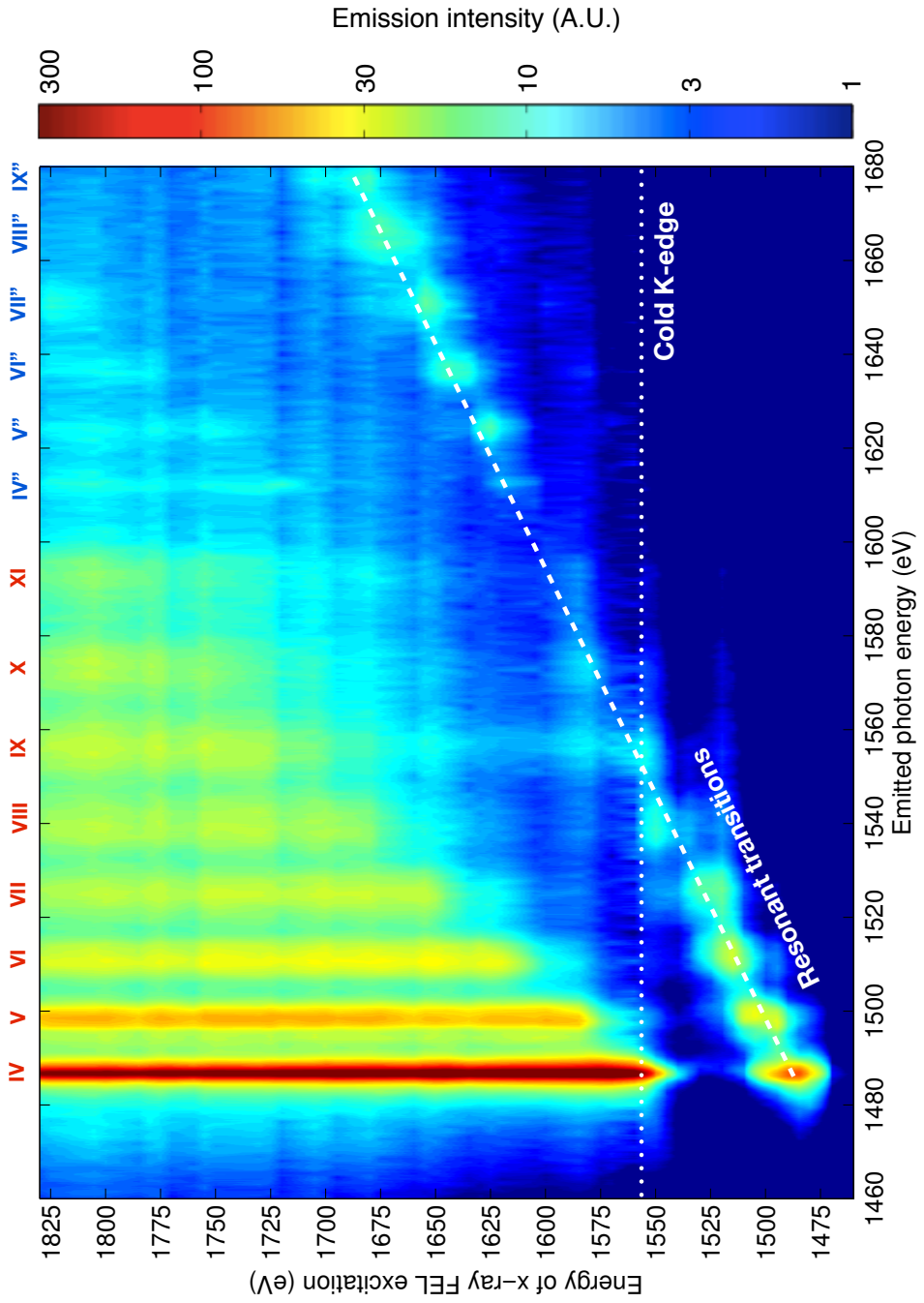

Figure 3.2: Experimental K_α spectra (horizontal lineouts) as a function of the FEL photon energy (vertical axis). Also plotted are the line x=y, corresponding to the excitation of resonant K_α transitions, and the line indicating the FEL photon energy corresponding to the K-edge of cold aluminium. The labels on the top identify each line, following the nomenclature introduced in Fig. 3.1. (Plot courtesy of Dr Vinko)

to the energy of one of the lines, copious emission from that particular line is observed as a result of resonant photoexcitation of a K-shell electron to the L-shell in the relevant charge state [55].

One of the most evident features of these spectra, if compared with the experimental data on Ne discussed earlier, is the uniformity of the emission from different charge states (with the exception of line IV), as long as the FEL photon energy is above a certain threshold for each of the lines. This is in stark contrast with the odd-even alternation observed in the gaseous sample and, as discussed in chapter 2, it is consistent with the prediction that the CSD is strongly affected by the collisions, rather than determined by a pure PAP... absorption chain. There are however two major differences between the Al spectroscopic data and the Ne data described before.

First of all, the satellite spectra are not necessarily representative of the CSD, as they would not reveal charge states produced either by V or C processes, in a system where the ionization of K-shell electrons happened to be energetically forbidden, because of both the temperature and the FEL photon energy being below the relevant thresholds. If this may seem a disadvantage, the unique possibility offered by FELs of tuning the pumping photon energy turns this into an extremely interesting opportunity: not only the energy can be easily tuned to be above the threshold for the K-shell ionization of all the possible charge states (at least for low and medium Z materials), so that the correspondence between spectra and CSD is restored, but also – much more importantly – the observation of the threshold photon energy for the emission of each of the lines is a charge resolved measurement of the K-edges in the system, a fact whose importance is underlined in the next chapter of the thesis. This is of course true only provided that the aforementioned C and V processes are efficient enough to produce the

relevant charge states to be revealed spectroscopically after the P processes, as I will prove shortly by using detailed simulations.

In this respect, our data are also different from any other experimental observation of satellite spectra (e.g. [58,60–63]), where the satellite features are generated by absorption of a broadband light or particle beam, that although probing the CSD of the plasma, is unable to provide information on the ionization energies.

The second main difference with the Ne data is that the satellite spectra are not just representative of the final CSD, but are rather sensitive to the whole CSD history, integrated *only* over the short LCLS pulse duration. In fact, provided that the final temperature is low enough not to cause collisional ionization of the K-shell (which again will require an appropriate modelling as a justification), each line can only be emitted shortly after a P process, due to the Auger lifetime ($\sim$1 fs). The spectroscopic diagnostic is thus intrinsically switched off at the same time as the pump laser.

3.2 Simulations

In order to interpret the experimental results, and to extract the relevant information (n, T, CSD...) that is convolved in the space and time integrated data, I performed detailed SCFLY simulations for the spectra obtained at different FEL photon energies.

In keeping with the model used for Ne, simulations at different peak intensities were performed and weighted according to the spatial profile of the pulse, but using the distribution measured by the $PbWO_4$ imprints, rather than a generic Gaussian profile. More details are given in §5.1.1.

The temporal profile was assumed Gaussian with a FWHM of 80 fs, neglecting the SASE structure, whilst the pulse energy for each simulated

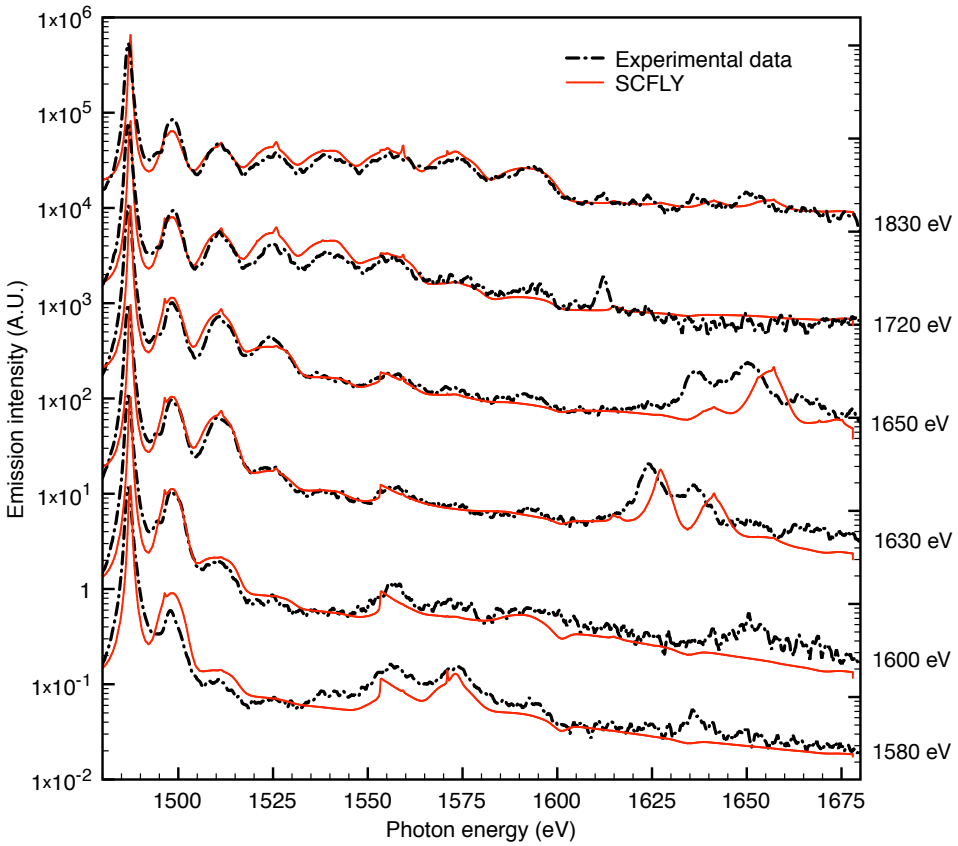

Figure 3.3: SCFLY simulations for the K_α spectra of aluminium produced at different FEL photon energies (values on the right), compared with the experimental data. A bremsstrahlung component, at the maximum temperature given by the simulations, has been added to the simulated spectra.

FEL wavelength was assumed equal to the average of the measured pulse energies for the single shots in the corresponding FEL photon energy bin. The spectrum of the laser was assumed Gaussian, with a FWHM given by 0.5% of the central energy (nominal value).

The simulated space and time integrated spectra for a set of different FEL photon energies are compared with the experimental data in Fig 3.3. Given that the simulations are only performed for a time corresponding to roughly twice the FWHM of the FEL pulse, the simulated spectra are not able to reproduce the underlying continuum emission recorded at later

times. A thermal bremsstrahlung background ($\propto \nu^3 e^{-h\nu/T}$, approximating the optical thickness as a constant), at the maximum temperature given by the simulations, was thus artificially added to the calculated spectra in Fig.3.3, whose effect is to fill in the zones of the spectra with no line emission.

The simulations show an excellent agreement with the experiment for the main K_α series[1], whilst the agreement worsens when attempting to reproduce the double K-hole lines. This is perhaps not surprising, given that these features are strongly dependent on intensity, and thus sensitive to the SASE spikes neglected in the simulations. Even for the hollow atom lines however there is a good qualitative agreement between calculations and experiment, even if the energies are slightly misplaced due to the uncertainties in the atomic data calculations. The two weak high energy features in the spectra at FEL energies of 1580 eV and 1600 eV might instead be explained by a resonant two-photon absorption exciting two electrons from the K to the L shell, a high-order process neglected in the calculations.

Importantly, the simulations shown in Fig. 3.3 were obtained without making any assumption on an (unrealistic) averaged electron density or temperature, so that the agreement with the data is not a mere result of a fit, unlike most of the traditional spectroscopic results, but it is rather an indication of a good reproduction of the physics involved.

3.2.1 Temperature and density evolution

Given the agreement with the data, and the ability of SCFLY to keep track of the energy absorbed in the easily reproducible X-ray single photon processes, the self-consistent values of the electron density and temperature, calculated as the system evolves, can be regarded with a certain confidence.

The temporal evolution of the density and temperature across the tar-

[1]The spectra in Fig 3.3 differ from those presented in [1], as they take into account the work described in Chapter 4 [2].

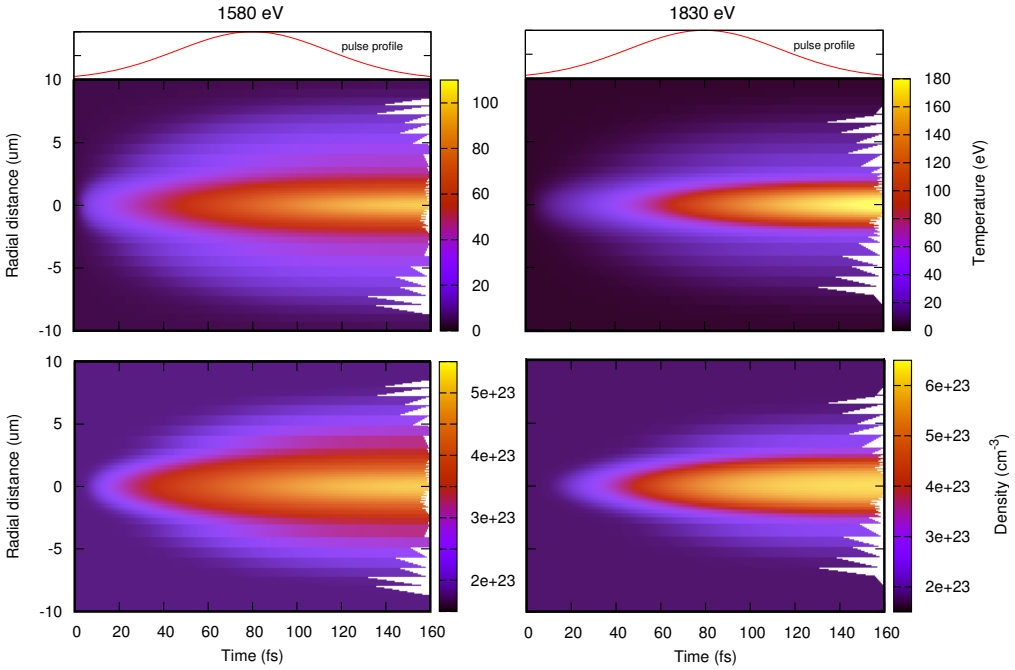

Figure 3.4: Calculated temperature (top) and density (bottom) evolution as a function of the radial distance from focus, for the cases corresponding to FEL photon energies of 1580 eV (left) and 1830 eV (right).

get, as the FEL is absorbed, is plotted in Fig. 3.4 for the two extremes of the simulated cases, namely the 1580 and 1830 eV pumping conditions. The plots assume cylindrical symmetry of the interaction zone, even if the weighting function used to sum the contribution of the different local intensities to the spectra doesn't rely on this approximation (see §5.1.1). The figure shows that in both cases, within the radius of the measured effective area ($\sim$1.7 μm) and within the FEL pulse duration, the system is heated to temperatures between 50 and 200 eV, and it is also highly ionized (5×10^{23} cm^{-3} corresponding to an ionization degree of $\sim$8), supporting the claim of isochoric heating of the sample to HDM conditions. Note that in addition the temperatures are always too low for the thermal ionization of the K-shell, so that a P process is required to reveal any of the lines in the spectra,

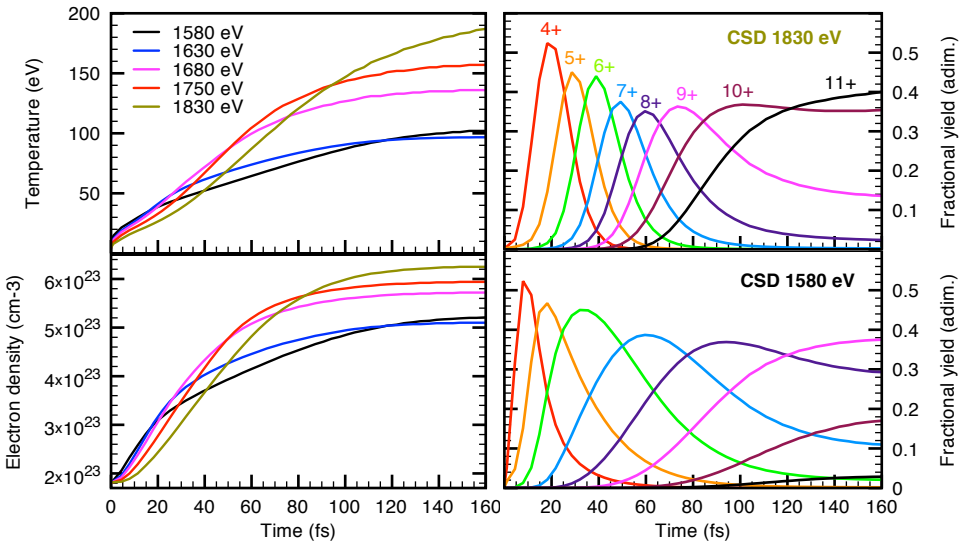

Figure 3.5: Local temperature and density evolution at the focus, for different FEL photon energies (left). The CSD evolution for the two simulations at 1580 eV and 1830 eV is plotted on the right for comparison.

supporting the idea that tuning the photon energy allows for a measurement of the K-edges in the plasma. The plots also show the existence of an extended outer cooler zone, heated to a few tens of eV by K-shell absorption in the lowest charge states, and explaining the higher emission observed for line IV and V in the experimental data shown in Fig. 3.2.

In order to compare more cases, and to discuss the (local) physics of the plasma evolution, Fig. 3.5 shows the density and temperature histories for several FEL photon energies (left), for the simulation at the peak intensity. Both the density and temperature evolution exhibit a very well defined behaviour as a function of the pumping photon energy: at early times the higher the energy, the lower are the density and temperature, but by the end of the pulse (80 fs FWHM, centred at 80 fs, as in Fig. 3.4) the situation is clearly inverted (with the exception of the 1580 and 1630 eV cases, see below). This is readily explained in terms of the coupling of different FEL

wavelengths with different charge states. As an example the CSD evolution for the two limiting cases is also plotted in the figure on the right. At early times the plots show that the 4^+ charge state is much more quickly depleted for the 1580 eV case than for the 1830 eV case, while for the other charge states the opposite holds. On the other hand, a quick look at Fig. 3.3 reveals that the line V, following a P process from a 4^+ to a 5^+ ion, is the highest-charge satellite observed at 1580 eV, i.e. this energy is below the K-edge value for charge states higher than 5^+, whilst all of the lines are visible for the 1830 eV case. The temperature and density trends can thus be explained as follows: the higher the photon energy, the lower is the cross section for P processes in the lowest charge states and thus the slower is the initial laser energy absorption (4^+ is depleted more quickly at 1580 eV than at 1830 eV); however, higher photon energies also means that progressively higher charge states can efficiently absorb the laser by P processes, so that as the system is heated and ionized, the P absorption channel remains active for longer for higher photon energies (5^+ is now depleted more quickly at 1830 eV than at 1580 eV), and the total absorbed energy will eventually catch up with that at lower photon energies.

Note that for the 1580 and 1630 eV cases the curves intercept each other twice, so that the final plasma at 1580 eV is hotter and denser than that at 1630 eV, in contrast with the general trend. Again this is not unexpected, from looking at Fig. 3.3: if the photons at 1630 eV, contrary to the 1580 eV photons, can ionize the 5^+ ions generating emission of the line VI, so that initially the curves for the 1630 eV case overcome those for the 1580 eV case, on the other hand the spectrum at 1580 eV clearly shows a resonance for the line X, so that a strong absorption channel is opened again for this case, when the 10^+ charge state becomes populated at a time that happens

to be around the peak of the X-ray pulse (Fig 3.5). The resonant absorption can then generate a copious amount of fast Auger electrons in the 1580 eV case, so that the density and temperature will rise significantly, eventually overcoming those at 1630 eV. The resonance of the line V" at 1630 eV is instead active only at the same time as the pumping of the line VI, so that it can only contribute to the efficient absorption at earlier times, when the P channel for the 1580 eV photon is still active.

3.2.2 Charge states distribution

What is clear from CSD histories just discussed is that the simulations seem to support the idea that the C and V processes are efficient enough to allow for an effective ionization of the system at all the pumping photon energies investigated, so that tuning the FEL wavelength allows for a selective probing of the charge states in the plasma, and a measurement of the K-edges.

However, having learnt from the work on Ne to distrust the CSD at the peak intensity when comparing with the data, in order to compare the CSD and the experimental spectra, Fig. 3.6 shows the space and time integrated CSD at different pumping conditions.

As expected from the spectra, the CSD doesn't show any odd-even alternation, even for the cases where several lines are observed in the spectra (so that the P processes – leading to the PAP signature in Ne – do occur). Given that in the latter case the V processes are less efficient than the P processes, the only mechanism that can explain this behaviour is the collisional mixing of the charge states.

What is perhaps surprising, when comparing Fig. 3.6 with Fig. 3.2, is that despite the very strong dependence of the spectra on the photon energy, the CSD in the different cases are very similar to each other, with a nearly

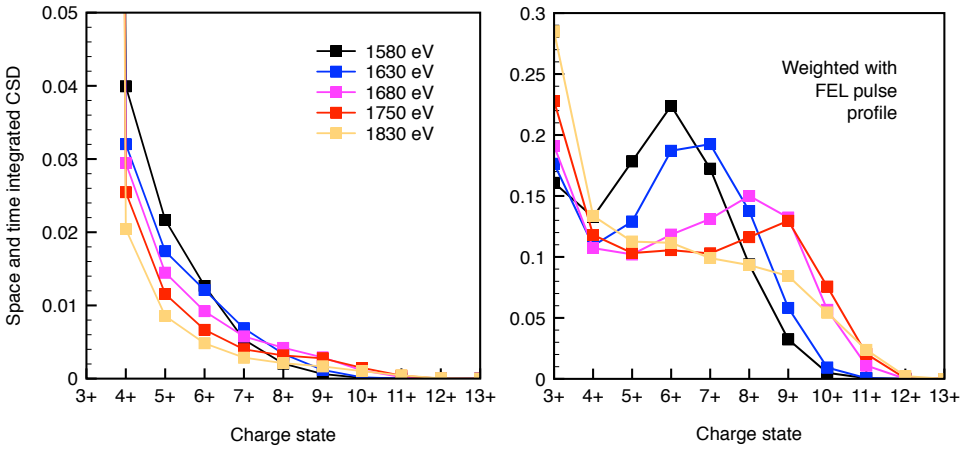

Figure 3.6: Space and time integrated CSD for different FEL photon energies. The pure fractional yield integrated over the total space and time extent of the simulations is plotted on the left, whilst the same quantity is weighted on the right plot with the FEL intensity profile (in order to relate it directly to the spectra through the photoionization events). Note the small difference in the number of populated charge states compared with the notable difference in the number of observed peaks in the spectra in Fig. 3.2.

identical number of accessible charge states. In particular the efficient ionization chain observed in Fig. 3.5 for the CSD at 1580 eV, is not only an effect of the increased V processes in the focal point, as happened for the local evolution of the CSD in Ne at 800 eV, but is rather observed even in the FEL-weighted space integrated CSD, stressing the contribution of the zones which are heated enough to allow for collisional processes to occur. This provides further evidence for the collisions being the dominant mechanism governing the CSD evolution: as the ground state 3^+ is depleted by P processes (true at any of the photon energies considered, save for the outermost part of the target) a great number of Auger electrons is available to the system (whose thermalization will be discussed later in §5.2.1), allowing for an efficient collisional valence ionization of the plasma up to highly charged ion stages. The plasma thus undergoes a very similar ionization chain in all of the cases (but of course slightly more efficient when the P absorption is

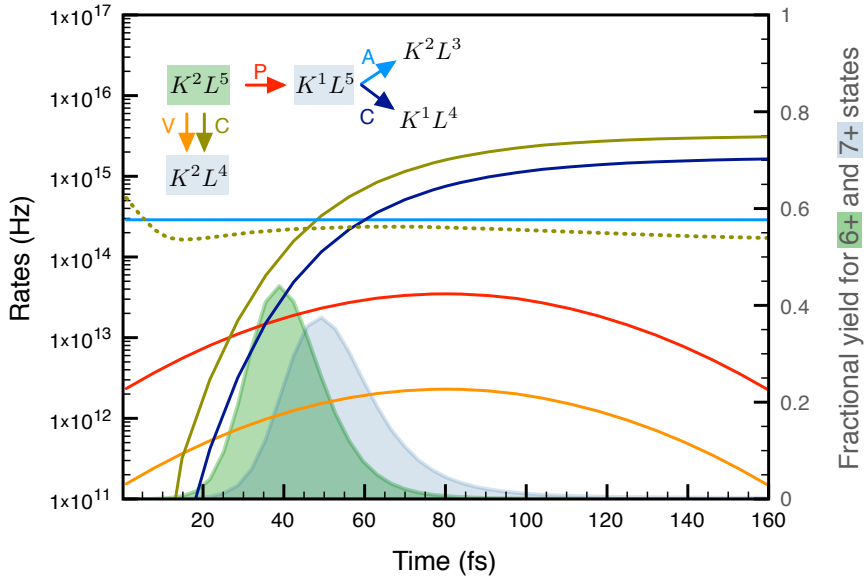

Figure 3.7: Rates of competing processes in 6^+ and 7^+ ions, typifying the main ionization processes for ground state ions and single K-shell ions induced by the X-ray absorption. The dotted line represents collisional recombination (inverse process for the line with the same colour). The rates are computed for the peak intensity simulation at 1830 eV. On the background the plot also shows the evolution of the population of charge states 6^+ and 7^+. The nomenclature for the processes follows that introduced in Chapter 2.

allowed for more charge states), and the X-ray laser can be regarded as a probe, as well as a pump, revealing by spectroscopy those charge states in which the P processes occur.

3.3 Collisional processes

In order to present a more quantitative picture about the collisional evolution just discussed, I will now focus on a numerical example: the plot in Fig. 3.7 shows a comparison between the rates of the ionization mechanisms relating the charge states 6^+ and 7^+, for the simulation at peak intensity, at an FEL photon energy of 1830 eV. The rates are plotted alongside the

evolution of the fractional populations of the two charge states considered.

The simulation shows that by the time at which the population of the 7^+ state starts to increase, around 25 fs, the valence collisional ionization is as efficient as the photoionization in depleting the 6^+ states, and by the time the population of the 6^+ ions has reached its maximum, it is higher by about an order of magnitude. The population of the 7^+ states however doesn't overcome that of the 6^+ until the collisional ionization between ground states is more effective than its inverse process (three body recombination, represented by the dotted line). The collisional processes are thus shown to be determinant in the evolution of the CSD, so that the latter could be expected to tend to the one found in LTE conditions, for the local values of density and temperature. Indeed, if one uses as an input the density and temperature values from the simulation (Fig. 3.5) at a time of 40 fs, a separate LTE calculation (performed with the same code), ignoring the FEL, predicts for the charge states 6^+ and 7^+ fractional populations of 0.4 and 0.3 respectively, that compare very well with the values in Fig 3.7. However, if comparing the populations of the states with a K-shell hole, for the LTE model and the non-LTE simulation, the LTE calculation is found to underestimate the populations for these levels by more than ten orders of magnitude, so that, as expected by the strong wavelength dependence of the spectra and the low temperatures, these states are entirely populated by the P processes. In other words, the plasma is in partial LTE conditions, with the ground state populations, dominating the CSD, well described by a Saha equilibrium (although the formulation of the Saha equation itself requires some attention in these conditions, as I will show in the next chapter), but with excited states largely determined by radiative processes.

The importance of the P processes in determining the population of the

ions having a vacancy in the K-shell doesn't mean that the collisional effects don't strongly affect these states as well. The collisional valence ionization rate for ions with a K-shell hole is also plotted in Fig. 3.7, and compared with the rate of the competing Auger processes. The two ionization processes are shown to become of the same order of magnitude within the temporal window corresponding to a significant population of the 6^+ charge states (from which the excited states are generated by P process), leading to two interesting effects.

First, even if the P processes had any effect on the CSD, as it would be the case if the FEL intensity was further increased, producing a more efficient depopulation of the ground states, the A processes may still be not fast enough to generate a PAP... signature in the CSD as in the case of Ne, due to the competing collisional mixing of states with a K-hole in different ionization stages.

Second, much more practically, the high collisional rates imply that line emission can still be observed, for line V to XI, even if the laser photon energy is below the K-edge for the relevant charge state, but it is above the K-edge for a lower one, the relevant K-shell hole state being generated by a PCC.. chain rather than a simple P process. The effect is clearly visible in the experimental data, Fig. 3.2, for the lower charge states: when the laser photon energy overcomes the K-edge value for a specific line (e.g. line IV turns red on the plot) a visible effect is observed also on the emission from next charge state, that also starts emitting by PC process (line V turns cyan) even if the photons are not able to directly photoionize the K-shell of the relevant ground state ions. A similar argument holds for the K-hole states excited by resonant K to L-shell pumping, the emission from a resonant line being always accompanied by emission from the neighbouring lines.

3.3.1 Time-dependent emission

Further insight is given by plotting the time resolved emission predicted by the simulations, shown in Fig. 3.8. The figure shows the two limiting cases of 1580 eV and 1830 eV pumping, for the simulation at peak intensity, corresponding to the n, T, and CSD histories plotted in Fig. 3.5. The weak emission observed at early times at the highest energies is bound-free emission corresponding to the K_β series (the cold K_β at 1560 eV, and satellites corresponding to emission from ions with a different population of the L-shell).

By comparing with the CSD evolution, when pumping at 1830 eV the peak emission from each of the lines closely follows the peak of the population of the corresponding lower charge state – e.g. the peak of line V (1500 eV) occurs at the same time as the peak of the 4^+ population. Recalling that the CSD essentially maps the populations of the ground states, this means that each of the charge states is then revealed by P ionization processes, energetically allowed for all of the charge states at this FEL photon energy, immediately followed by the emission of a K_α photon (before collisions or Auger processes can change the state of the emitter). That is to say, the laser behaves as probe of the CSD, as predicted.

When pumping at 1580 eV the situation is more interesting. Here, by looking at the experimental data, the only lines for which the laser photon energy is above the K-edge are line IV and V, whose peak emission occurs again at the time of maximum population for the corresponding ground states (0 fs for 3^+, and $\sim$10 fs for 4^+). For other lines the emission appears to turn on at an earlier time than those that could be inferred by the CSD, indicating that, as expected, the laser cannot probe anymore by P processes those charge states for which its photons are below the K-edge. The only

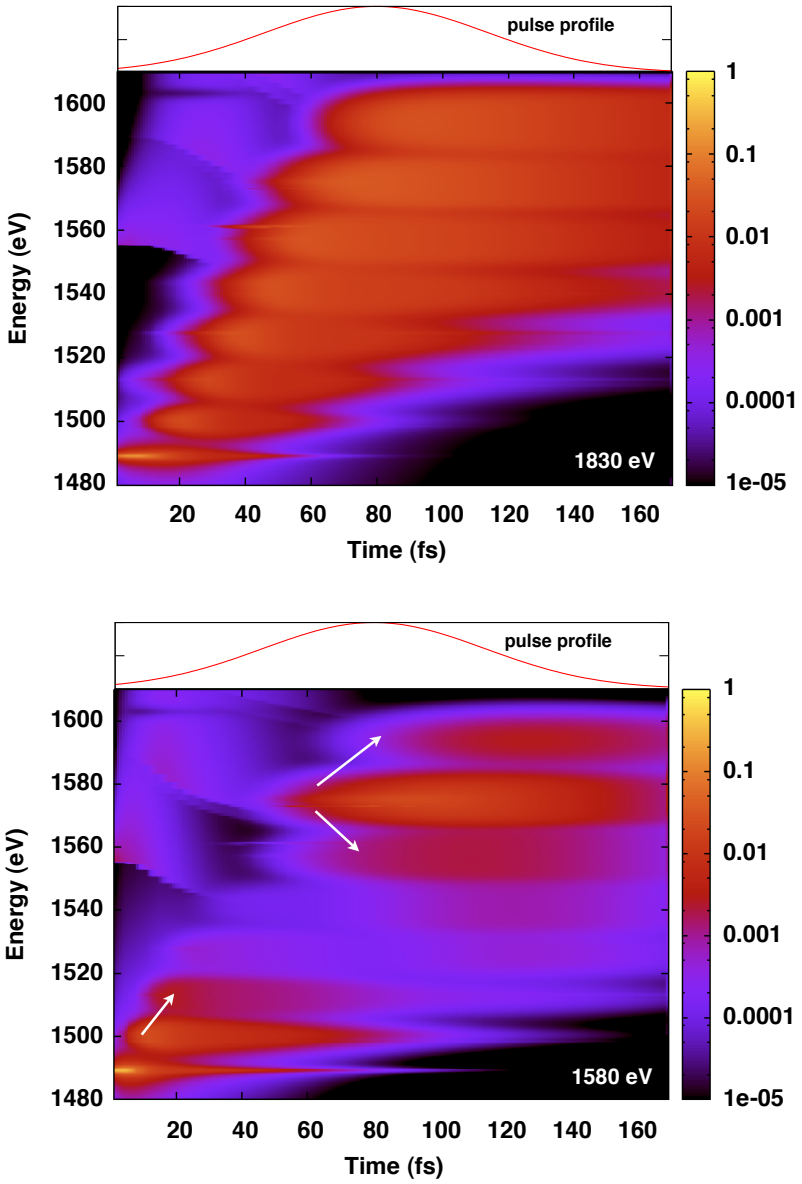

Figure 3.8: Calculated time dependent emission at FEL photon energies corresponding to 1830 and 1580 eV. The y axis corresponds to the emitted photon energy, whilst the colour coding is proportional to the emitted intensity. As the collisions progressively ionize the sample, strong emission from a given charge state is only observed if the FEL photon energy is above the threshold for the creation of a K-shell hole (all the charges states at 1830 eV, first two charge states at 1580) or on resonance for a K to L bound-bound transition at 1580 eV. The white arrows indicate valence shell ionization processes in ions with a K-shell hole.

line that can still be pumped by the laser is the resonant line X, which, as discussed when talking about the temperature evolution, turns on as soon as the population of the charge state 10^+ becomes appreciable. The fact that other lines are visible at all is of course due to the collisional processes affecting ions with a K-shell hole. In fact the simulated time dependent spectrum clearly shows two different mechanisms for generating those lines (arrows on plot), whose emitter configurations can arise either by multiple L-shell ionization after a P process in a 4^+ ion, or by multiple collisional recombination to the L-shell (or ionization for line XI) after a K to L photopumping process in a 10^+ ion (resonance). The effect is particularly visible for line VII (1525 eV) showing two different emission zones at different times, corresponding to the two different processes. As already discussed, this "collisional propagation" of both resonances and above-edge lines is clearly visible in the experimental data.

In conclusion the simulations are able to provide a full self-consistent story about the plethora of effects shown by the experimental data, with minimal input by the user. The calculated (and not imposed) temperatures and densities, well constrained by the ability to reproduce features like the multi-line resonances or below edge emission, both dependent on the collisional rates, prove the ability of the LCLS to generate HDM on inertially-confined timescales. At the same time the relatively low temperature excludes the possibility of collisional K-shell ionization, indicating that the data contain charge resolved information on the K-edge thresholds at the time of the pumping process, before any hydrodynamic expansion may occur.

CHAPTER 4

Continuum lowering in Hot Dense Aluminium

I have described in Chapter 3 how coupling detailed SCFLY simulations with the spectroscopic results from an FEL experiment, where the LCLS isochorically heats an Al foil, leads to the description of an extremely well characterized HDM sample. In particular I have shown that the X-ray pulse also acts as a selective probe for those charge states for which the laser photon energy is above the K-edge value, so that a charge resolved measurement of the edges is possible, in a system where the ion density is exactly known.

The aim of this chapter is now to discuss why this measurement is extremely interesting, and – at last – how this relates to the kind of difficulties concerning the modelling of HDM plasmas described in the Introduction. Specifically, measuring the K-edge values for the different charge states in

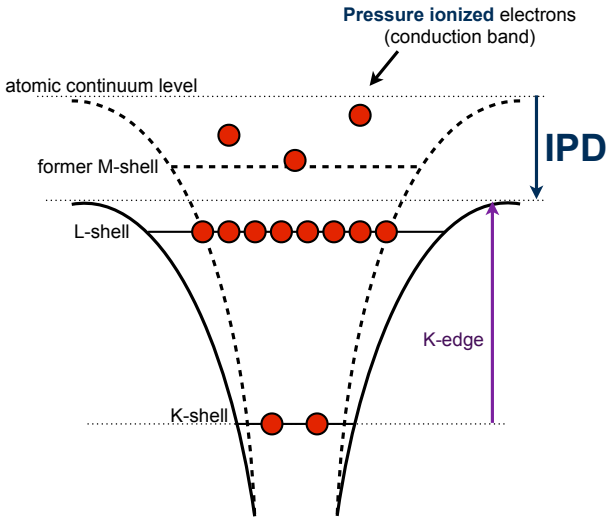

Figure 4.1: Representation of the continuum lowering effects in cold aluminium at solid density. As the ionization energies are reduced by the IPD, pressure ionization occurs for the M shell, whose states become part of the continuum, with the formation of the conduction band.

an HDM system allows one to tackle one of the most difficult and high-impact problems related to dense plasma modelling (and, as a consequence, with most of the usual dense plasma diagnostics): that of the validity of continuum lowering models [2].

4.1 Continuum lowering in dense plasmas

Continuum lowering is the perturbative effect of the environment on the electrostatic potential of an ion in a plasma: as a result of the interaction with the surrounding particles, the ionization thresholds are reduced with respect to the case of an isolated ion [64–70], by a quantity referred to as IPD, or Ionization Potential Depression.

The effect is sketched in Fig. 4.1 for the well known case of an Al ion embedded in the metallic environment – acting as a three times ionized plasma

– in a cold sample. The figure shows the reduction of the K-edge value with respect to the isolated ion case (the K-edge being experimentally well known to occur at 1560 eV, rather than the unperturbed value of 1610 eV for the 3^+ ion), as well as one of its most important consequences, known as *pressure ionization*: when the IPD exceeds the binding energy of a given atomic state, that state becomes part of the continuum, and thus any electron that would otherwise occupy it becomes a conduction electron (for the solid state physicist) or a pressure ionized electron (for the plasma physicist).

A correct evaluation of the IPD is crucial for most dense plasma calculations. An example is provided by looking at its effect on the Saha equation, relating the populations n_z and n_{z+1} of subsequent charge states in LTE:

$$\frac{n_{z+1}}{n_z} = \frac{2}{n_e}\frac{U_{z+1}}{U_z}\left(\frac{2\pi m_e k_B T}{h^2}\right)^{\frac{3}{2}} e^{-(IP_z - IPD_z)/k_B T} \tag{4.1}$$

where U_z and IP_z are the partition function and ionization potential of charge state z. The IPD not only explicitly shifts the ionization balance (in the direction of increased ionization) by appearing in the exponential of Eq. (4.1), but also affects the ratio U_{z+1}/U_z by providing , through the pressure ionization, a cut-off to the partition functions that may be different for different charge states. This shift, also occurring in the general non-LTE case, in turn affects the EOS of the plasma[1] as well as its opacity, so that the continuum lowering plays a pivotal role behind the scenes of astrophysical and ICF research (see the Introduction), as well as affecting any experimental measurement of temperature and density relying on the ratio of spectroscopic lines or on bound-free scattering in dense plasmas.

The reason I have been referring to the continuum lowering as a dense plasma effect is readily explained. For a low density (weakly coupled) plasma, the classical plasma theory holds, and the electrostatic potential

[1] In particular, one can prove [71] that the use of Eq. (4.1) without modifying the EOS leads to thermodynamic inconsistencies

of an ion is modified by the plasma accordingly to the well known Debye-Hückel (DH) theory of screening. The IPD for an ion of charge (z-1) in this case can be evaluated as the difference in the potential energy of a bound electron ($r \simeq 0$) with respect to an unperturbed Coulomb case, that is:

$$IPD_{DH} = \lim_{r \to 0} \left(\frac{ze^2}{r} - \frac{ze^2}{r} e^{-r/\lambda_D} \right) = \frac{ze^2}{\lambda_D} \tag{4.2}$$

where λ_D is the Debye screening length. As this theory is valid only for $\lambda_D \gg n_e^{-1/3}$, it follows that the IPD for dilute plasmas is much smaller than the binary Coulomb interaction energies, which in turn are much smaller than the thermal energy (weak coupling), leaving the ionization balance largely unaffected. In order to provide a quantitative example, for the weakly coupled Ne plasmas discussed in Chapter 2 ($n_e \sim \bar{z} \times 10^{18}$ cm^{-3}, $T \sim 100$ eV) the DH model gives an IPD of the order of $\bar{z}^2 \times 10^{-2}$ eV, which is not even able to pressure ionize atomic shells up to a principal quantum number of 10 for all of the charge states, in contrast with the solid Al case, where pressure ionization can be regarded as the cause of the metallic behaviour.

Postponing a more quantitative discussion on the IPD at high densities to the sections dedicated to the experimental data, I will now rather discuss the theoretical models used to describe the effect in strongly coupled plasmas, where the DH screened potential is not a valid solution of the Poisson equation for the ion, nor can other analytical solutions be easily identified.

4.1.1 Stewart-Pyatt model

The most used and accepted model of continuum lowering is undoubtedly the Stewart and Pyatt (SP) model [66], put forward in 1966. It is the model used in codes like FLYCHK [42], CRETIN [72], LASNEX (DCA) [73], amongst

the most widely used codes for HDM simulations.[2]

The starting point of the SP model is the finite-temperature Thomas-Fermi (TF) model. They first write down a radial Poisson-Boltzmann equation for the ionic potential, where the electron density (bound and free) is described by Fermi-Dirac statistics, and the ion density is described by Boltzmann statistics; the solution then provides the spatial distribution of free electrons and ions, that is in turn used in a second Poisson equation to determine the perturbing potential, whose value at the origin gives the IPD.

Stewart and Pyatt numerically solve this problem for the non-degenerate case and moderate coupling ($K < 3$, see below), and find results which are consistent with those they obtain by deriving an analytical approximation under a very strong assumption: that the potential (ϕ) can be approximated by solving the Poisson-Boltzmann equation only for the region where the potential energy $e\phi$ is much smaller than k_BT, where analytical solutions can be found in two specific limits (note that this means explicitly avoiding the difficulties related to Γ_{ei}>1). Introducing the quantities $y = e\phi/k_BT$, $x = r/\lambda_D$ and $z^* = \langle z^2\rangle/\langle z\rangle$, the latter assumed to be considerably larger than 1, the approximate potential is derived by merging at a point x_1 (unknown) the particular solutions given by

$$y(x) = \begin{cases} \frac{C}{x}e^{-x} & x > x_1, \quad y \ll 1/z^* \\ \frac{K}{x} - J + \frac{x^2}{6(z^*+1)} & x < x_1, \quad 1/z^* \ll y \ll 1, \end{cases} \tag{4.3}$$

where K, J and C are constants to be defined by the boundary conditions. Given that in the analytical approximation used by SP the short range solution is regarded as valid even for x approaching 0, hence $K = ze^2/\lambda_D k_B T$, reproducing the unperturbed Coulomb potential at the origin, and J is then simply the IPD in units of k_BT. The long range solution has the form of a

[2] FLYCHK and CRETIN have been modified, following this work, to include, as an option, the Ecker and Kröll model discussed later

DH potential, but no ad hoc assumption is required for C. Imposing the continuity in x_1 of y and its first and second derivatives, and eliminating C and x_1 from the resulting equations, yields the widely used SP formula for the IPD

$$J = \frac{IPD_{SP}}{k_B T} = \frac{3}{2}\frac{ze^2}{k_B T \lambda_D}\frac{\left[\left(\frac{r_{IS}}{\lambda_D}\right)^3 + 1\right]^{2/3} - 1}{(r_{IS}/\lambda_D)^3} \tag{4.4}$$

where $r_{IS} = (3z/4\pi n_e)^{1/3}$ is the *ion-sphere radius* (the radius of a sphere containing a charge that equals that of the central ion, assuming a uniform electron density), and for z is taken the charge of the central ion after an ionization process (z=1 for the neutral atom).

In weak coupling conditions, that is $r_{IS}/\lambda_D \ll 1$ (or equivalently $n_e^{1/3}\lambda_D \sim \Gamma_{ei}^{-1/2} \gg 1$), the SP formula reduces to the DH formula (4.2). In the opposite limit of strong coupling, $r_{IS}/\lambda_D \gg 1$, it yields the following IPD

$$IPD_{IS} = \frac{3}{2}\frac{ze^2}{r_{IS}}. \tag{4.5}$$

This limit reproduces the results of the simplest of the IPD models for high density plasmas, the ion-sphere model (IS) with uniform electron density [64, 67], where the IPD is simply given by the Coulomb interaction of the central ion with the uniform charge density inside a sphere of radius r_{IS}. In these strong coupling conditions, which hold for our experimental densities and temperatures, the SP model thus predicts a scaling $z^{2/3}$ for the IPD.

4.1.2 Ecker-Kröll model

As Stewart and Pyatt point out in their paper, three years earlier Ecker end Kröll (EK) had put forward a model for the IPD [65] which agrees with their own model in predicting the low density DH limit, but predicts a different

scaling of the IPD with the charge of the ion for strongly coupled systems.

Ecker end Kröll follow a different procedure to compute the IPD, deriving first the two coupling limits separately, and then merging them (but with some reservations). Their starting point is the derivation of the Saha equation for a system of interacting semiclassical particles, where the IPD_z in Eq. (4.1) is found to be

$$IPD_z = \mu_{z+1}^{el} - \mu_z^{el} + \mu_e^{el}. \tag{4.6}$$

Here μ_i^{el} is the electrostatic contribution to the chemical potential of a species i, and an ionization process is seen as an annihilation of an ion of charge z with the creation of an ion of charge $z+1$ and of a free electron. As μ_i^{el} is related to the average electrostatic micropotential ϕ_0 by the Debye charging process, $\mu_i^{el} = z_i e \int_0^1 dx \phi_0(x z_i e)$, the problem is once again reduced to the evaluation of the potential, which in strongly coupled plasmas is described by a non-linear Poisson equation. Note that if ϕ_0 is linear in z (as it will be), the combined effect of the integral defining the chemical potential and of equation (4.6) is to naturally yield an IPD depending on $(z+1)e^2$, that is on the charge of the atom after the ionization process, which was an imposition, rather than a result, in the SP model.

Ecker and Kröll identify three characteristic lengths for the problem:

- $\mathbf{r_{linear}}$ is the smallest radius r above which $|z_i z_j| e^2 / r k_B T \ll 1$, for any couple of charges z_i and z_j (including -1 for the electrons), so that the Poisson-Boltzmann equation can be linearized (DH solution).

- $\mathbf{r_{EK}} = (3/4\pi[n_e + n_i])^{1/3}$ is the average interparticle distance, used to approximate the smallest distance from the ion greater than which it is meaningful to represent the particle ensemble by a continuous density

distribution (the *collective* region).

- $\mathbf{r_{Coulomb}}$ is the largest distance below which the potential can be satisfactorily approximated by a Coulomb-like law.

The authors then solve the problem in two different regimes, depending on whether the particle density n is below or above a critical value given by

$$n_{crit} = \frac{3}{4\pi}\left(\frac{k_B T}{z_{max}^2 e^2}\right)^3 \tag{4.7}$$

where z_{max} is the highest charge state in the plasma. Note that n_{crit} is roughly the density at which $z_{max}^2\Gamma_{ee}$=1 at a given temperature. It can be easily shown that the following relations hold:

$$[\mathbf{n \ll n_{crit}} \quad \Leftrightarrow \quad r_{linear} \ll r_{EK}] \implies \frac{r_{EK}}{\lambda_D} \ll 1 \tag{4.8}$$

$$[\mathbf{n \geq n_{crit}} \quad \Leftrightarrow \quad r_{linear} \geq r_{EK}] \implies \lambda_D(n_{crit}) \geq \frac{r_{EK}}{\sqrt{3}} \tag{4.9}$$

In the weak coupling limit (4.8) the Debye length is much greater than r_{EK}, and as a result the DH potential valid for $r > r_{EK} \gg r_{linear}$ approaches the Coulomb form as $r \to r_{EK}^+$. This means that the Coulomb and DH solutions can be merged at r_{EK}, in exactly the same fashion as in the SP model.[3] Neglecting the x^2 term in the short range potential of Eq. (4.3), imposing the continuity of the potential and its derivative, and using the fact that $r_{EK}/\lambda_D \ll 1$, the resulting potential yields an IPD that equals the IPD_{DH} of Eq. (4.2), in agreement with the SP low density limit.

For densities above the critical density, the plasma is instead in the strong coupling regime (4.9). Note that for Al at temperatures around 100 eV the critical density is of the order of 10^{20} cm^{-3}, well below the solid density value, so that our experimental Al plasma is in this regime. In this case

[3]The original EK derivation uses some $\bar{r}$ such that $r_{Coulomb} \lesssim \bar{r} \lesssim r_{EK}$, which is then neglected in the formulas as $\bar{r}/\lambda_D < r_{EK}/\lambda_D \ll 1$.

one can assume that $r_{Coulomb}$ is smaller but of the same order of magnitude as r_{EK}, or $r_{Coulomb} = \gamma\ r_{EK}$ with $\gamma \lesssim 1$, but the DH potential cannot be extended anymore down to r_{EK} as before, but only down to r_{linear}, so that the SP approach is not justified in this regime. The potential in the region between $r_{Coulomb}$ and r_{linear} is then unknown, but the authors argue that if the screening remains an increasing function of the density, as in the undercritical case, the right-hand limit of the potential in $r_{Coulomb}$ is smaller than the value given by the DH potential at the critical density. Thus, by merging as before the Coulomb-like solution with either 0 or the DH solution at n_{crit}, the potential $\phi_0(z_i e)$ can be constrained as follows

$$-\frac{z_i e}{\gamma\ r_{EK}} \leq \phi_0 \leq -\frac{z_i e}{\lambda_D(n_{crit})} \frac{1}{1+\frac{\gamma\ r_{EK}}{\lambda_D(n_{crit})}}, \tag{4.10}$$

where the term on the right is what would give the DH solution at low densities, under the conditions (4.8). Under the strong coupling conditions (4.9), and introducing the quantity C such that $\gamma^{-1} \geq C \geq (\gamma + 3^{-1/2})^{-1}$, the equation (4.10) yields $\phi_0 = -C z_i e / r_{EK}$. Using ϕ_0 and Eq. (4.6) to calculate the IPD_{z-1} (so that z, in what follows, is the charge of the ion after the ionization, as in SP), the EK formula for the IPD at high densities is finally given by

$$IPD_{EK} = C\frac{ze^2}{r_{EK}}, \tag{4.11}$$

where r_{EK} is independent of z, in contrast with r_{IS} of Eq. (4.5), yielding an additional scaling of $z^{1/3}$ with respect to the SP model.

Of course, the C in Eq. (4.11) remains an unknown quantity, so the authors propose to join the two density regions at n_{crit} by setting $C = r_{EK}(n_{crit})/\lambda_D(n_{crit})$; however they also point out that this is not really justifiable, as the DH form is not valid up to the critical density. Note that

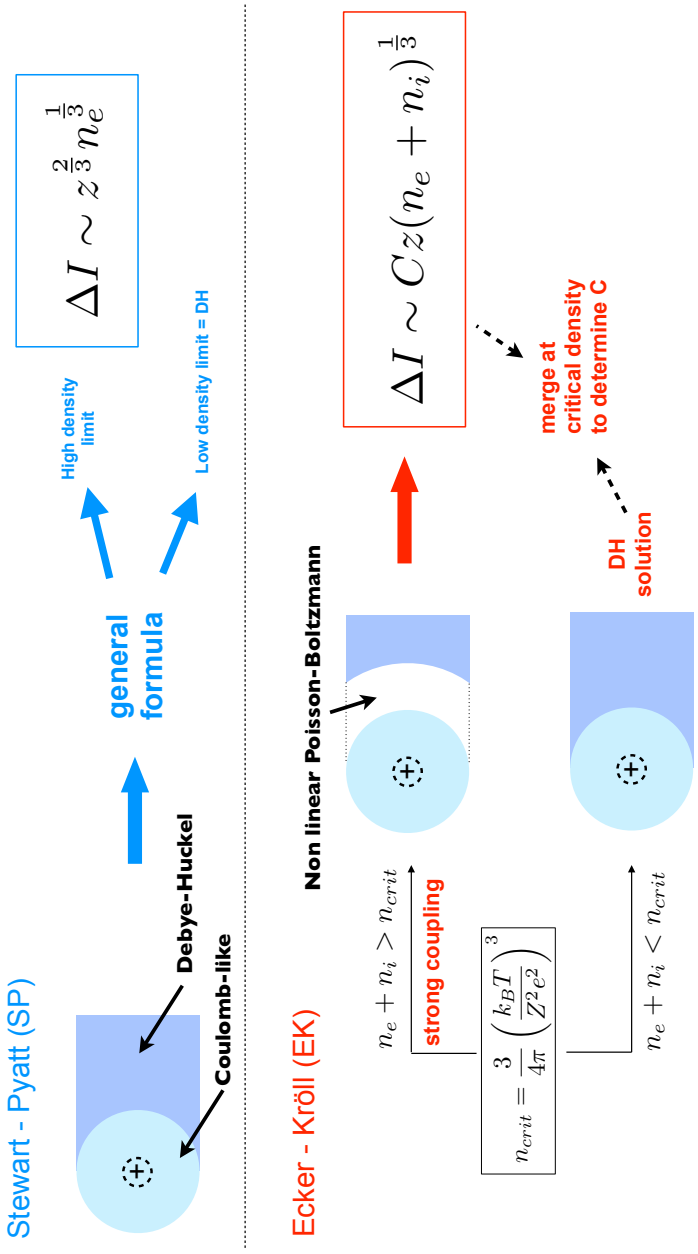

Figure 4.2: Synoptics of the SP and EK models. Note that according to the EK model the SP derivation is not valid above the critical density. This leads to a stronger scaling of the IPD with the charge of the ion for high density plasmas.

even in this approximation, C is a function of the temperature but not of the charge of the ion, so that the stronger scaling in z, with respect to the SP model, is not affected by C. By construction however C is of the order of 1, so that I will simply refer to the IPD in the EK model as that given by Eq. (4.11) with $C = 1$. To this approximation, the high density limits of the SP and EK models are both independent of the temperature. A comparison between their derivation and scaling laws is summarized in Fig. 4.2.

4.2 Measuring the IPD

As can be inferred from Eq. (4.5) and (4.11), and summarized in Fig. 4.2, a validation of the continuum lowering models just described involves experimental data where both the particle densities and the charge of the ion (for which the effect is observed) are known. Moreover the models have to be verified in plasma conditions for which the IPD itself is not negligible, which as discussed excludes ideal plasmas, which yield the weak DH limit.

Despite the impact of the IPD on dense plasma calculations, which in turn are routinely used to infer experimental results, there are only a very few attempts towards an experimental investigation of the phenomenon itself. This is partially due to the aforementioned difficulties of studying, by standard laser techniques, the overcritical transient plasmas required to investigate the IPD for highly charged dense systems. The few available data rely on spectroscopy, either observing continuum edge shifts [74, 75] or pressure ionization effects [76–78] under shock compression or the subsequent expansion of a sample.

The continuum edge measurements suffer from the limitation of being unable to distinguish between different charge states in the plasma. Thus only very small shifts can be observed when the system is driven by a laser,

as a result of the concurrent ionization effects, that tend to blue-shift the edge, and the increasing IPD, that tends to red-shift it.

On the other hand, the disappearance of emission/absorption lines by pressure ionization, that in principle can select a given charge state by looking at a specific line, not only cannot provide more than an upper limit to the IPD, but also it does so in conditions where it is difficult to distinguish between the merging of the line to the true continuum edge and the merging of the spectroscopic series to the continuum due to line broadening (Inglis-Teller effect [79]).

For any of the two methods however, a limiting factor in comparing the results with the models is the degree of accuracy to which the experimental densities are known, as any real-life laser-plasma experiment inevitably presents large density gradients, both in time and space, that are hard to model and to resolve experimentally, with the additional difficulties of converting the calculated or measured mass density distribution into an electron density distribution, which requires the knowledge of both the local temperatures and the IPD itself.

The experiment on Al described in this thesis overcomes all of the above problems. By varying the wavelength of the short LCLS pulse, and recording the K_α emission from different charge states, it is in fact possible to measure *with charge resolution* the K-edges, that is the IPDs, in a highly ionized HDM plasma, where any emission event, used as a diagnostic, can only occur within a few femtoseconds after an absorption event: this means that, unlike any other investigation, the ion density through the entire sample is precisely known, being equal to the solid density value, given that the system has no time to expand during the pumping process. At the same time the plasma generated by the X-ray absorption is virtually free from longitudinal

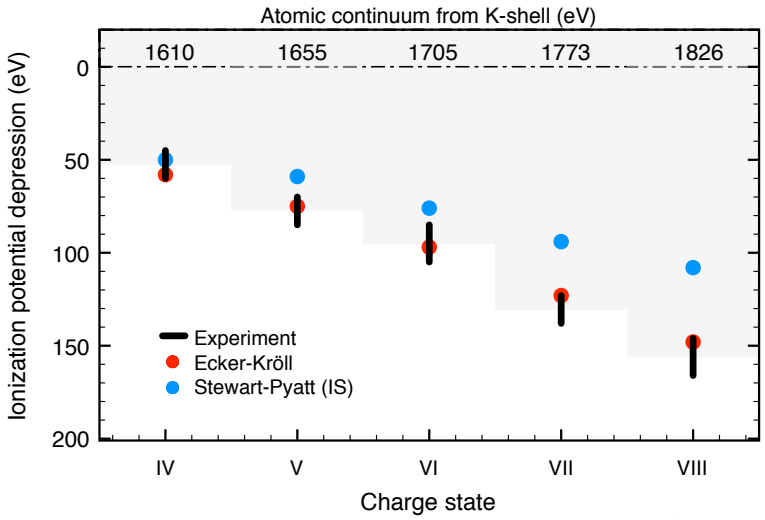

Figure 4.3: Measured values of the IPD compared with SP (IS) and EK predictions assuming $z = \bar{z} + 1$ (recall that line IV corresponds to ionizing a 3^+ ion, with $z = 4$ as the value to be used in the EK and SP formulae). The IPDs are determined by subtracting the measured K-edges from the atomic values reported on the top of the plot. The errorbars on the experimental K-edges are taken equal to the width of the ramp on the curves of the line emissivity versus the FEL photon energy.

gradients[4], and the simplicity of the absorption process also removes most of the uncertainties on the temperature and electron density calculation, easily retrieved by SCFLY simulations, provided a choice is made for the continuum lowering model.

4.3 Experimental results

An effective value for the IPDs in our hot-dense Al plasma can be obtained from Fig. 3.2, by considering vertical lineouts (emission versus FEL photon energy) for each of the satellites, and then subtracting the resulting K-edges from the corresponding atomic values[5]. These IPDs are plotted in Fig. 4.3 for the first five charge states, where they are compared with the values predicted by the SP and EK high density limits, Eq. (4.5) and (4.11), under

[4]Recall that the transverse intensity distribution of the LCLS has been measured, so it doesn't pose any relevant problem either.

[5]The values are those used in SCFLY, based on the model in [80].

the approximation that the charge of the central ion equals the average ionization of the plasma $\bar{z}$ (with $n_e = \bar{z} n_i$). The lines IX to XI have been omitted, as those lines overlap with the K_β and its satellites, whose combined effect with the collisional mixing of the lines (as discussed in §3.3) makes it difficult to identify the K-edge with a reasonable accuracy, as can be easily seen from Fig. 3.2.

This first comparison shows immediately that the measured values for the IPD disagree with the predictions of the standard SP model, save for line IV, with a stronger disagreement – up to 40 eV – for higher charge states (note that the highest charge states would be the most difficult to investigate with standard optical laser techniques, owing to sample expansion). In contrast, the EK predictions are consistent with the experimental values for all of the considered ionization stages, due to the stronger predicted scaling of the IPD with the charge of the ion. Moreover, the values for line IV, which is emitted when the sample is cold, should be overestimated by the Fermi energy (11 eV) in both of the (semiclassical) models, which would put the EK model in very close agreement with the well known value for this case (50 eV), and would instead slightly worsen the agreement of the SP model.

However, although extensively used in the field, the approximation $z = \bar{z} + 1$ used in the above discussion is not necessarily representative of the experiment, as the plasma is never[6] in a single ionization stage (see Fig. 3.5), and as a result emission from a given ion may occur at times when the average ionization stage of the plasma (and thus n_e) is higher, increasing the IPD with respect to the values plotted in Fig. 4.3. For this reason, in order to compare in a rigorous way the experiment with the models, full space and time resolved simulations are required, for which the IPD

[6]Save of course at $t = 0$, in the initial metallic state.

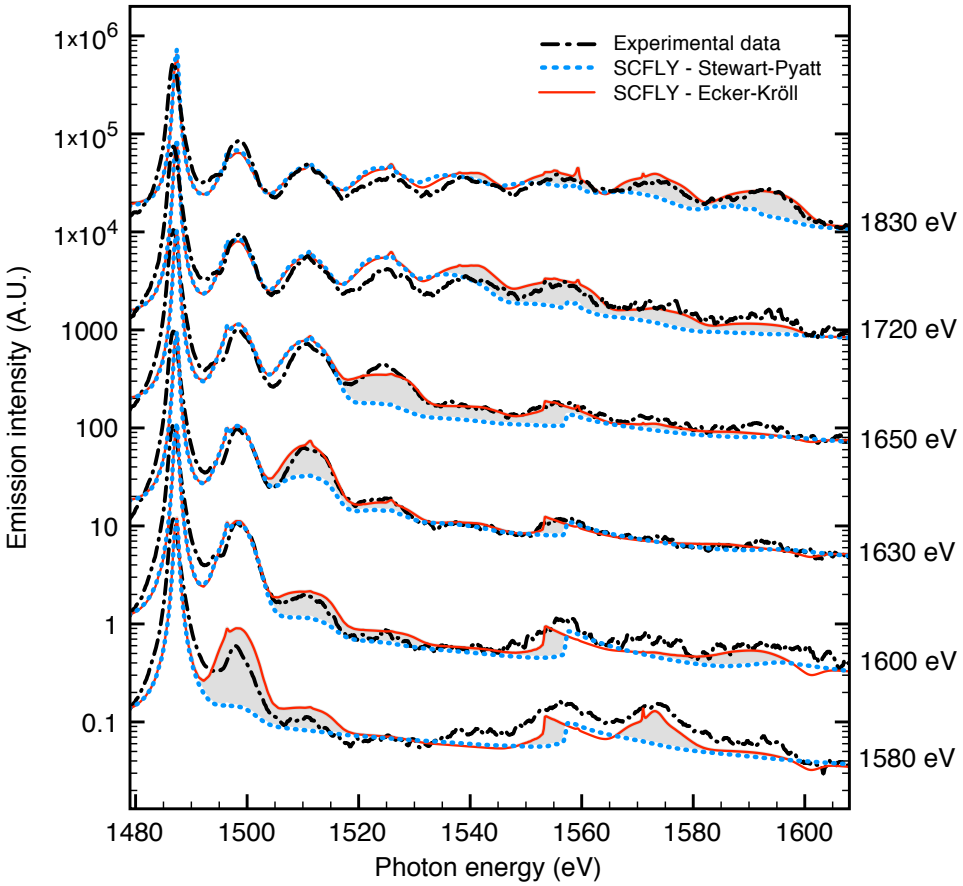

Figure 4.4: Comparison between SCFLY simulations performed with the SP and EK models, for six different FEL photon energies (reported on the right). The grey zone indicates the difference between the SP and EK spectra.

for each of the charge states is calculated as the system evolves, using the instantaneous values of electron density and temperature.

4.3.1 K-edges and simulated spectra

The spectra from six SCFLY composite simulations, using either the SP or the EK model, for different FEL photon energies, are compared in Fig. 4.4 with the experimental data. For each photon energy, 26 simulations at different intensities were performed, and the emission summed from them in a weighted manner according to the experimental F-scan (see §5.1.1). The

complete SP formula (4.4) was the default model used in SCFLY, whilst I implemented the EK model within the code. Consistently with the effective IPD results just discussed, the figure clearly shows that the SP calculations overestimate the FEL photon energy threshold (i.e. the effective K-edge) for the appearance of line V to VII, whilst the agreement with the EK simulations is nearly perfect.

For line VIII (for which the disagreement between the effective edges is even larger, so that the same applies as for the above lines) the figure rather compares the simulations at 1720 eV, which according to Fig. 4.3 is just above the K-edge value predicted by the SP model: even in this case however – where both the models slightly overestimate the intensity of the line – the SP simulation still shows a poorer agreement, as line VIII appears red-shifted with respect to the experimental case. Indeed for all of the lines VIII to XI, and for the entire FEL photon energy range up to 1830 eV, the SP calculations predict red-shifted lines, and underestimate the intensity of the emission for the high-energy part of the spectrum, whilst the agreement with the EK simulations remains excellent. The reason for the red-shifts will be discussed shortly.

The comparison of the simulations for the FEL photon energy of 1580 eV also provides a secondary example of the sensitivity of the experiment to the IPD. The resonant line X ($\sim$1575 eV) is in fact reproduced only by the EK simulations and not by the SP ones. This is mainly due to the increase in absorption caused by the possibility of K-shell absorption in charge state 4^+ leading to the emission of line V in the EK simulations: because of this absorption channel the final temperature in the EK case is about 10 eV higher than in the SP calculation (at the focal point), and the average ionizations are respectively 8.7 and 7.7, with the result that

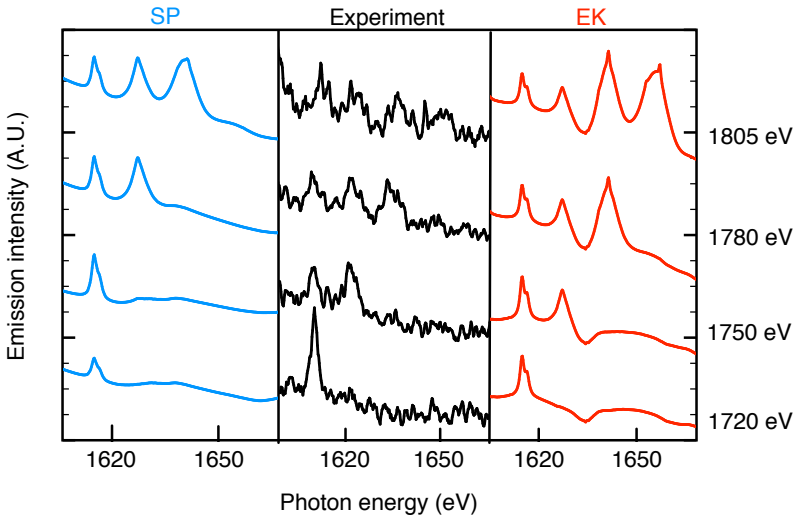

Figure 4.5: SCFLY simulations, using either SP or EK, for hollow atom lines at different FEL photon energies (on the right), compared with the experimental data.

the charge state 10^+ in which the resonant process occurs is significantly populated during the FEL pulse only in the EK case, where the plasma ionization is greater. The effect is also enhanced by the effect of the IPD on the ionization balance, once because even at the same temperature the difference between the two IPDs ($\sim$ 60 eV for ions 9^+) causes a higher ionization for the higher IPD, and once again because even if the two cases had the same average ionization of ~ 9, the higher IPD would still yield a higher population of the 10^+ ions.

The K_α emission from the main series is not however the only feature which is sensitive to the K-edge variations. A second IPD measurement can be performed, using the same procedure, by looking at the reduction in the ionization potential for those ions in which a second electron is removed from the K-shell immediately after a first P process. The resulting experimental spectral lines IV" to VII" are compared with the EK and SP simulations in Fig. 4.5 for four increasing FEL photon energies. Despite the poor ability

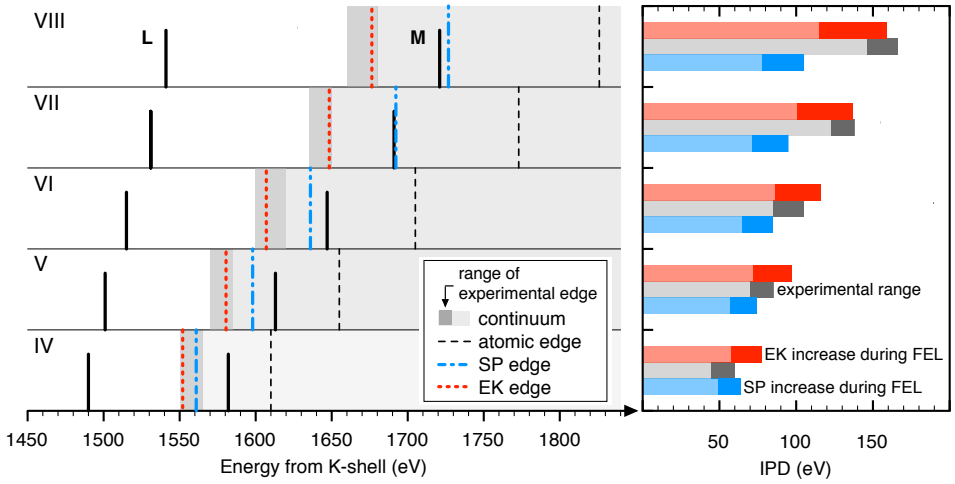

Figure 4.6: Left – Position of atomic shells and measured continuum (grey zone) with respect to the K-shell for the lines IV to VIII. The L- and M-shell position is given by the energies required for a K-L or K-M transition in ions with a final number of L-shell holes corresponding to the given line. The position of the atomic edge is also plotted, as well as the K-edges predicted by the SP and EK simulations (near-edge simulations, at the focus, and for the time of maximum emissivity of the given line). Right – The dark portions of the histogram compare the measured IPD values (as in Fig. 4.3) with the total variation of the IPD occurring during the plasma evolution in the SP and EK simulations at the focus.

of the simulations to reproduce the details of these lines, as discussed in §3.2, the threshold FEL photon energies at which each line can be excited can be easily compared with the predictions of the models, and once again the SP model tends to overestimate the K-edges, whilst the EK model can correctly reproduce the number of lines for each photon energy. Note that these lines arise from the same charge states as the lines V to VIII discussed before, but are observed in different pumping conditions (thus different n_e), given by the higher FEL photon energies required to photoionize the second K-shell electron. This is thus an independent measurement of the IPDs.

Having performed detailed simulations, one can also update Fig. 4.3 to include the effect of the density variations during the plasma evolution. This

is done in Fig. 4.6, on the right, where the total variation of the IPD during the plasma evolution, for the two models, is compared with the measured effective IPDs. The plot shows the variation for the simulation at the focus, that also represents the maximum variation within the sample, in simulations where the FEL photon energy is determined by the experimental K-edge. The instantaneous values of the K-edges for the two models, taken at time of maximum emission for each of the lines, are also shown in the left part of the figure, and are compared with the experimental edges. These values are consistent with those under the approximation used in Fig. 4.3, as could have been inferred by the time resolved spectra discussed in §3.3.1, where the line emission does peak at the time where the average ionization equals the charge of the ion to be ionized.

4.3.2 Pressure ionization effects

The left plot in Fig. 4.6 also compares the position of the predicted continuum edges with that of the L- and M-shell, for ions with the relevant number of L-shell holes for a given line. This shows another difference between the EK and SP model: whilst for the former the M-shell is always pressure ionized, the SP model predicts that the M-shell does rebind for highly charged ions. In particular for line VIII emission from ions with the relevant number of L-shell holes can occur in ions with bound M-shell spectator electrons. By looking at the simulations it turns out that for all of the lines VIII to XI, at a time where the relevant charge states are populated, the EK model predicts a pressure ionized M-shell, whilst the SP one predicts it to be bound.

This different behaviour in turn affects the emitted spectra, as can be seen in Fig. 4.7, focusing on the high energy part of the spectrum at an FEL photon energy of 1830 eV. The result is the aforementioned red-shift of the

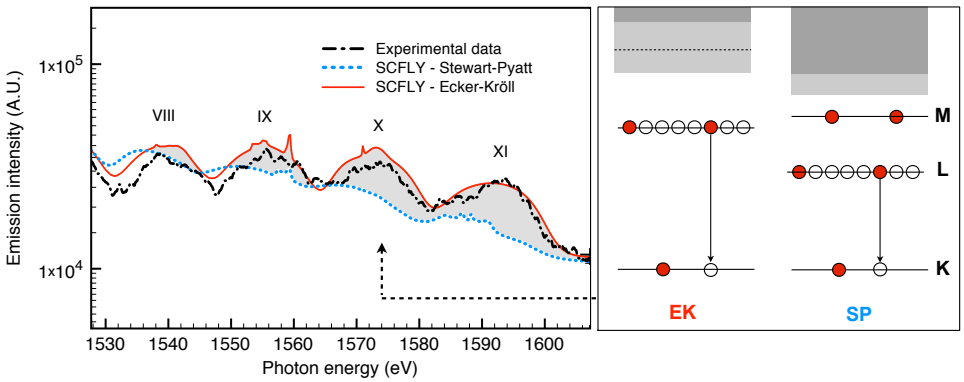

Figure 4.7: Effect of the pressure ionization on the simulated spectrum at 1830 eV. The presence of bound spectator electrons in the M-shell causes a given line to be emitted from lower charge states, causing a red-shift of the K_α peak. The effect is sketched for line X on the right. The EK simulations include a 5 eV broadening of the He_α doublet, consistent with a rough estimation of the Stark width obtained by FLYCHK simulations (the current version of SCFLY has no Stark broadening).

lines VIII to XI, occurring because of the shift of the inner-shell energy levels induced by the presence of the M-shell spectator electrons. This red-shift is instead absent both in the EK simulations and in the experimental data, indicating that at the densities observed in the experiment the M-shell is indeed pressure ionized.

Note that the presence of M-shell spectators also changes the K-edge for a given line, by reducing – through the charge state – both the ionization potential and the IPD. It could then be argued that the failure of the SP model in reproducing the lines corresponding to the lower charge states is due to an overestimation of the IPD, rather than an underestimation, that would pressure-ionize states which are essential in order to reproduce the results. Indeed this was the initial interpretation of the Al data, in keeping with a pre-existent modified SP model that was included in the FLYCHK and SCFLY codes [81]. However the use of such an ad hoc model leads to notable inconsistencies between data and simulations, because of

the red-shift effects just discussed and because the number of ions with a populated M-shell is different from the number of ground state ions (hence the difference in the line intensity for the SP simulation in Fig 4.7). The data can clearly distinguish between the two scenarios, as can be easily verified by comparing the simulations in [1] and the EK simulations presented here and in [2].

To summarize, whilst the IPD measurements performed through the K-edges are in principle independent of pressure ionization and the related problems of line merging, pressure ionization might still affect the results by varying the charge state corresponding to a given line; however, the experimental position of the lines, and a consistent use of SCFLY detailed simulations (where the right ratio between the lines is reproduced only by the EK case), rather than a rough average-ionization estimation of the IPDs, is even able to resolve this secondary issue.

Note finally that the definition of bound and free states itself is quite arbitrary for states which are very close to the continuum, as real-life pressure ionization is never a step-like process, but rather involves a continuous transition between localized and delocalized orbitals, thus experimental results on the IPD relying on the definition of a charge state depending on the population of these high-lying states are to be considered suspicious. The Al data do not suffer from this problem either, as according to Fig 4.6 the M-shell is always well separated by the experimental position of the continuum.

4.4 Remarks

Whilst the derivation of the EK model presented earlier explicitly points out why it should not be surprising that the SP model cannot reproduce the experimental data, far more obscure is the physical reason underlying

the success of the EK model with C=1. In particular nothing can be said about its validity at densities which are much closer to the critical density, that strongly depends on the temperature.

Nevertheless the main purpose of this work is not to explain the success of the EK model, nor to suggest that one should blindly replace the widespread SP model with the EK one in dense plasma simulations, but rather to stress the two following points:

– first, that a careful validation of the continuum lowering models used in dense plasma simulations is required, given that at high ionizations the potential errors introduced by a wrong IPD model can be quite significant (e.g. see the 40 eV discrepancy between the predicted and measured IPD for line VIII, which is comparable with the plasma temperature), and can have a strong impact on ICF and astrophysical simulations;

– second, that despite the fact that this validation has been hindered in the last 60 years by the intrinsic limitations of the optical laser experiments, the newly available FEL sources provide us with a formidable experimental platform to perform this kind of studies, as I hope to have shown in this thesis.

Further work on continuum lowering, following from the results here described, will be mentioned in the concluding chapter.

CHAPTER 5

Details of the modelling

The SCFLY simulations described in the previous chapters of this work rely on the ability to model, with reasonable accuracy, the details of the space and time dependent FEL-plasma interaction, as well as the detailed plasma processes. I will now point out some of the approximations and models used in describing the system and discuss their impact on the final results.

5.1 Modelling the X-ray laser properties

The first step towards a correct modelling of the laser-plasma interaction is of course the ability to reproduce the properties of the FEL itself. In fact, even if the detailed single photon processes were easily reproducible in the X-ray regime, this would be of little help if a reasonable laser intensity history and spatial distribution were not used in the SCFLY simulations.

In this section I will first show how the measured spatial laser intensity distribution is treated in the simulations, and compare the results obtained by using this model with those obtained using a Gaussian beam approximation. Second, I will focus on the effects of the temporal structure and pulse duration of the FEL, which are the most difficult properties to reproduce for the LCLS pulse, due to the chaotic behaviour related to the SASE process. Finally I will briefly comment on the pulse energy used in the calculations.

A detailed study of the bandwidth effects is, however, not required, as the FEL spectrum is routinely measured at SXR (see e.g. [82]) and is roughly described by a Gaussian distribution[1] with a FWHM given by 0.5% of the central photon energy. This nominal spectrum is used in all of the simulations for the Al experiment, and its adequacy can be inferred by the reasonable reproduction of the resonant line pumping in the simulations shown in Fig. 3.3.

5.1.1 Measured spatial profile

The transverse intensity distribution of the focused LCLS beam has been reconstructed by the analysis of laser imprints on a $PbWO_4$ substrate, acquired during the experiment, following the procedure described in [56]. This technique provides a fluence scan (or F-scan) across the beam profile: if $F(x, y)$ represents the local value of the normalized fluence at coordinates (x, y) in the focal plane, and S represents the area enclosed by an iso-fluence curve on that plane, the F-scan is expressed as a function $F(S)$.

Due to the short X-ray wavelengths, the Rayleigh range of the LCLS beam is much longer than the thickness of the 1 μm targets used in the Al experiment (indeed it has been measured to be of the order of 10 mm [83]), so that in the longitudinal direction the beam is collimated.

[1] A red-shifted shoulder is observed at longer pulse durations, but it is negligible for the 80 fs pulses used in this work.

It is then trivial, by inverting the function $F(S)$, to determine the volume of the target experiencing a given fluence F. In turn, the distribution of these volumes, as a function of the fluence, can be used in order to weight the emission spectra generated in zero-dimensional SCFLY simulations at different peak fluences, thus reproducing the space integrated spectrum.

Each of the space-integrated simulations for the Al plasma shown in this thesis is a combination of 26 single fluence simulations, where each fluence value is converted into a temporal intensity profile. The intensities (I_n) span five orders of magnitude, and are given by $I_n = I_0 e^{-2(n\cdot 0.1)^2}$, where $I_0 = I_0(\omega, t)$ is the focal intensity distribution, and $n = 0, \ldots, 25$. If $I_{n\pm 1/2} \stackrel{\text{def}}{=} (I_n + I_{n\pm 1})/2I_0$, where I_{-1} is defined equal to I_0, and if h is the thickness of the target, the weighting factor for the simulation at intensity I_n, in terms of the measured $S(F)$, is $V_n = h \times (S(I_{n+1/2}) - S(I_{n-1/2}))$.

The $I_n V_n$ product for the measured profile is plotted in Fig. 5.1, where it is compared with the same quantity calculated for a Gaussian beam having the same total fluence. The choice of plotting this product, rather than just the weighting function, is justified by the fact that the emitted spectra to be weighted are directly proportional to the number of photons absorbed locally, so that the $I_n V_n$ distribution is representative of the relative importance of the simulations at different I_n. The measured profile was given in terms of a double Gaussian fit and – as can be inferred from the figure – its effect is to enhance the impact of the low intensity wings of the beam profile on the resulting spectrum.

Two space-integrated spectra calculated by weighting the same set of 26 simulations with the two different beam profiles are shown in Fig. 5.2. The simulation in the figure is the one at 1830 eV, which shows all of the lines emitted by the highest ionization stages, which are the most sensitive to the

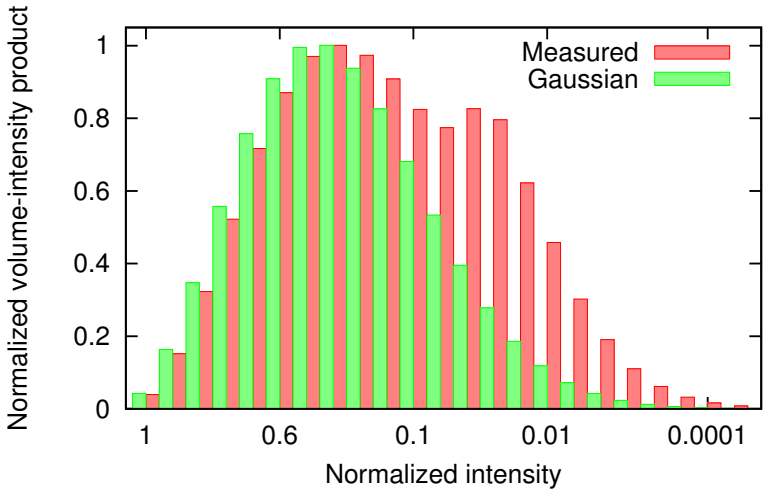

Figure 5.1: Comparison between the measured spatial profile and a Gaussian distribution having the same fluence. The product of the local intensity (determining the emissivity) and the corresponding interaction volume (used to weight the simulations), normalized to its maximum value, is plotted against the local intensity values. The intensity sampling is chosen to be consistent with a linear sampling in the radial coordinate of a Gaussian beam.

high intensity part of the beam (they are emitted at higher temperatures and densities). Even if for this case the calculation using the measured profile slightly overestimates the ratio between line IV and V (peculiar of the 1830 eV case, see Fig. 3.3), the overall profile is well described by this spatial distribution. Conversely, the spectrum obtained assuming a Gaussian profile cannot reproduce the correct ratio between all of the lines; even if one normalized this spectrum in such a way that the highest charge states are reasonably reproduced, this would result in a notable underestimation of the intensity of lines IV, V and VI.

The overall shape of the recorded spectra is thus proven to be a direct consequence of the double bump shown in Fig. 5.1 for the measured profile: for example, this additional contribution of the low intensities in the measured case, with respect to the Gaussian case, is the ultimate reason for the

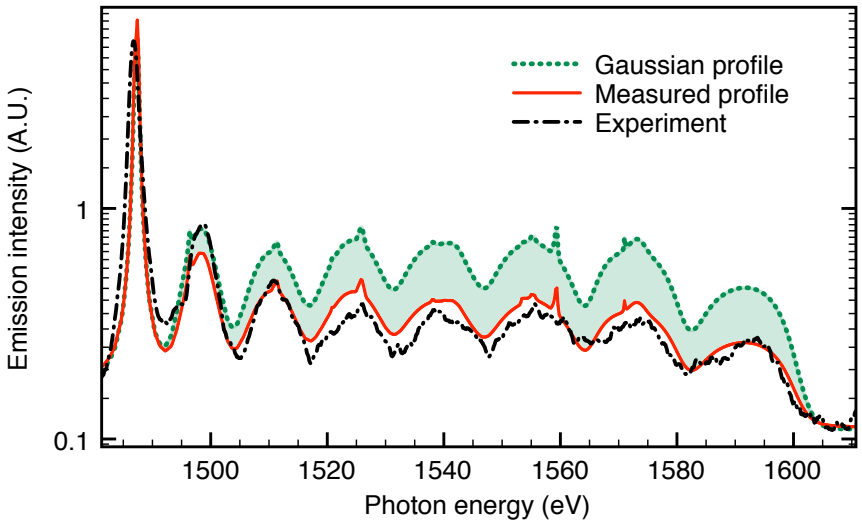

Figure 5.2: Comparison between SCFLY simulated spectra at 1830 eV, assuming either the measured spatial profile or a Gaussian profile. The Gaussian simulation was normalized to match the experimental cold K_α profile; due to the simulated line ratios, a different normalization would still be unable to reasonably match the experiment.

higher emissivity of line V with respect to the other satellite lines, which is clearly visible from the experimental data in Fig. 3.2, but is not reproduced by the calculations using a Gaussian profile, as shown in Fig. 5.2.

The discussed procedure to model the spatial distribution of the laser intensity neglects the longitudinal intensity gradient caused by the laser absorption. This is justified by the moderate thickness of the target (about an attenuation length for cold Al; note that the transmission is expected to be much higher than in the cold case, due to the rapid ionization) and by modified SCFLY calculations including a full radiation transport model, as described in [55, 84], that predict just about a 5% variation in the final temperature between the front and the back of the target (D. S. Rackstraw – private communication).

The approximation used is consistent with the standard approach used in FLYCHK or SCFLY, which actually simulate infinite uniform plasma

slabs, by taking into account opacity effects on the rate equations with an escape factor formalism [44]; the simulations presented in this work result indeed from a sum of 26 different annular sections of such uniform slabs, each simulating a region pumped by a different laser intensity.

Finally, note that even if the escape factor formalism is technically suitable only for the uniform slab case, opacity effects are however negligible for the pumping conditions described in this thesis: first, the K-shell photoabsorption processes for a given charge state is maximum at times where the relevant absorbing charge state is relatively depopulated, as discussed in [55], second the absorption of the plasma emission is always negligible with repect to both the laser absorption and the collisional processes, so that opacity effects cannot influence the plasma evolution.

5.1.2 SASE temporal profile and pulse duration

Due to the chaotic nature of the SASE amplification process the main uncertainty on simulating the LCLS pulse is related to the definition of a temporal profile. The most evident issue in modelling a SASE pulse is the aforementioned spiky structure, which can affect processes which are strongly intensity-dependent – such as the production of hollow ions – even for data which are averaged over several shots [48]. Another possible source of errors is the pulse duration itself, which cannot be measured by standard autocorrelation techniques, due to the lack of suitable optics, and is rather assumed to be equal to the duration of the electron bunch: although this is the value provided by the facility, and used in all of the simulations discussed so far, several independent investigations have concluded that the LCLS pulse has actually a duration which is somewhat shorter than this nominal value [46, 47, 85, 86].

In order to provide a rough estimate of the impact of these combined effects on the results of the simulations, I have performed a set of four local (i.e. I_0) calculations, using the same peak fluence but a different temporal profile of the LCLS. Note that the (local) fluence is the parameter that can be measured, through the F-scan, as described in the previous section, in spite of the uncertainty on the time envelope.

The four different pulse profiles used are plotted in Fig. 5.3-A, and include the standard 80 fs Gaussian profile used in all of the simulations (a), a shorter Gaussian pulse having a duration of 40 fs (b), a pulse composed by 1 fs (FWHM) triangular spikes modulated by the 80 fs Gaussian (c), and a variation of the latter obtained by shuffling a few spikes (d). This last profile is used in order to roughly mimic the effects of the random amplitude of the spikes in a SASE pulse, which in reality are not modulated by any well defined time envelope, by preserving the total pulse energy and the pulse duration.

The simulations were performed for an FEL photon energy of 1650 eV: as can be seen by comparing the spectra in Fig. 5.3-D with that in Fig. 3.3 the local simulations still preserve the difference between line VII (laser above the K-edge for the relevant P process) and line VIII (laser below the K-edge). This case has indeed been chosen as it presents both lines for which the laser is above the edge and lines for which the opposite holds; a study of the chaoticity effects on the intensity of the double K-hole lines, although interesting, has not been performed[2], as the lines are poorly reproduced by the simulations (Fig. 4.5) and a more sophisticated investigation on the SASE effects on hollow atom states can be found in [48]. The effects of the intensity spikes on the laser absorption by hollow ion states will be however discussed.

[2]For this reason the spectral synthesis for Fig. 5.3-D has a cutoff at 1600 eV, as the simulations are computationally very expensive, due to the fine time grid required to model the spikes.

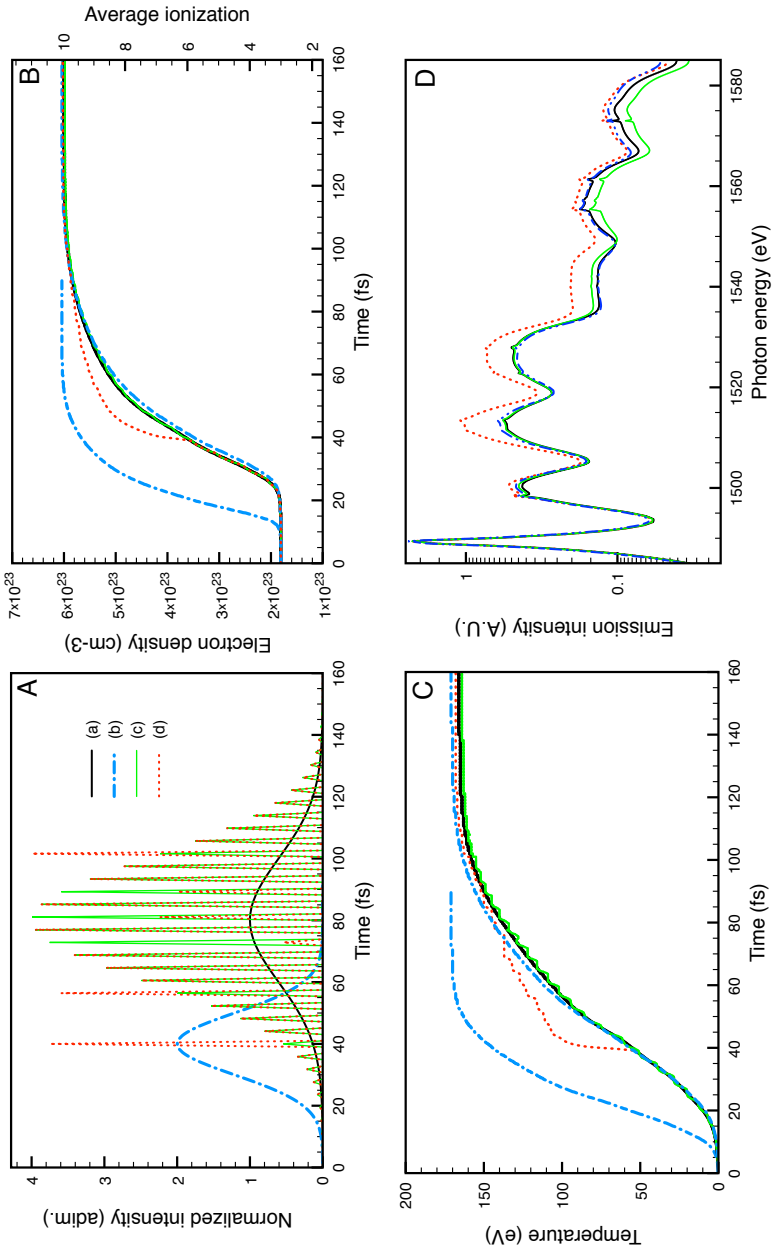

Figure 5.3: Effects of the FEL temporal profile on the simulation I_0 for the 1650 eV case. A – pulse profiles compared in the figure; all of the pulses have the same (measured) fluence. B, C – Electron density and temperature evolution for the four cases; the results of the simulation for the 40 fs pulse are plotted both as a standard function of time $f(t)$ and as a function $f(t/2)$, to verify the overlap with the 80 fs simulations. D – Local time-integrated spectrum for the four simulations.

The electron density and temperature evolution for the four simulations are compared in subfigures B and C. The results of the simulation for the 40 fs pulse are also plotted by stretching the time axis by a factor of 2, in order to verify the overlap with the 80 fs simulations. As can be expected by the collisional evolution mechanism described in Chapter 3, the final density and temperature values are independent of the intensity profile, so that the four simulations all yield roughly the same result.

In the case of the long and short Gaussian pulses, (a) and (b), the difference between the two cases is that for the short pulse the laser energy is absorbed twice as fast, so that the system undergoes almost exactly the same evolution process as in the 80 fs case if the timescale is appropriately rescaled: a very small divergence between the temperatures is still observable at a time of 50 fs (or 25 fs for the 40 fs simulation), when $\bar{z} \sim 7$ and the higher intensity for the simulation (b) causes a better absorption of the laser energy through the resonant line VII" (1652 eV) arising by a PP process from 7^+ ions (evidently intensity dependent).

Note however that the simulation (c), which has an intensity spike at ∼45 fs, when the intensity is similar to that of the short pulse (b) at the relevant time, shows a much better overlap with the simulation (a): this results from the spike duration being shorter than the lifetime of single charge states (compare with Fig. 3.5) so that periods of increased absorption balance out with periods of zero absorption during this lifetime. This oscillation in absorption is clearly visible in the temperature profile for (c), whilst the density – determined by the collisional processes rather than the laser absorption– is much less sensitive to these variations. The situation is clearly different for simulation (d), where a spike at 40 fs increases the instantaneous intensity by more than an order of magnitude, causing a steep rise

in temperature through both the aforementioned PP process, and the active simple P processes, and in density, through consequent collisions. As the absorbing charge states are quickly depopulated however (up to 7^+, given that the laser is below the K-edge for the 8^+), the P processes are quenched, and the temperature and density are soon again determined by the total energy absorbed, overlapping eventually with those of simulation (a).

Finally Fig. 5.3-D shows the total effect of the different profiles on the time integrated spectra for the main K_α series. The simulations (a), (b) and (c) show a very good overlap with each other, whilst the simulation (d) shows an increased emission for the lines VI and VII, arising from absorption by the charge states populated around 40 fs ($\bar{z} \sim 6$, from subfigure B). Note also the increased emission for line VIII, for which the laser is below the K-edges, determined by the collisional effects described in §3.3 as a result of the increased emission for line VII, although the difference between above and below edge emission is still clearly recognisable.

It is important to stress that the case (d) provides an idea of the possible processes occurring in a single shot, where the random distribution of the SASE intensity spikes can create a condition such as that of the enhancement of particular lines discussed here; however, given that the Al data described in this thesis are a result of a sum of several shots, it is reasonable to expect that such effects will be reduced when looking at the time-integrated data, ultimately justifying why the simple Gaussian envelope approximation used in the simulations is able to reproduce the results quite accurately.

The prediction on the plasma parameters, as well as the measurements of continuum lowering are thus insensitive to both the pulse duration and the SASE spiky structure, provided that an accurate value of the fluence is used, and the experimental data are averaged over many FEL shots, so that

the random effects caused by the SASE fluctuations are washed out.

5.1.3 Beamline transmission

A minor source of uncertainty on the FEL parameters is the degree of accuracy by which the pulse energy impinging on the target is known. The pulse energy of the LCLS is measured for every single shot, in a gas detector [87] situated upstream of a beamline composed of seven optical elements. An average of the energies measured for the different shots composing a given experimental spectrum is then used in the simulation, assuming a known beamline transmission.

A measurement of beamline transmission was performed by using a second gas detector [88] situated downstream of the optical chain leading to the SXR experimental chamber, resulting in a measured transmission of the beamline of $\sim$30%. This value is 1.7 times lower than the value estimated by the nominal reflectivities [89] of the SXR optical components (BC_4 coated Si mirrors at 0.8° grazing incidence [90], with nominal reflectivity 92% at 1500 eV).

The simulations discussed in this thesis are performed using the nominal beamline transmission. This has been preferred to the measured value because of a better reproduction of the resonant features, in spite of the negligible difference in the reproduction of the main K_α spectra. I thus briefly discuss here the effects of this choice on the results of the simulations.

A comparison between the local simulations I_0 and I_5, that differ in intensity by roughly the same factor as the nominal and measured beamline transmission, is shown in Fig. 5.4. On the left are plotted the time-integrated spectra for the simulations at an FEL photon energy of 1580 eV, where the I_5 simulation predicts a very low emission for line XI, which makes it

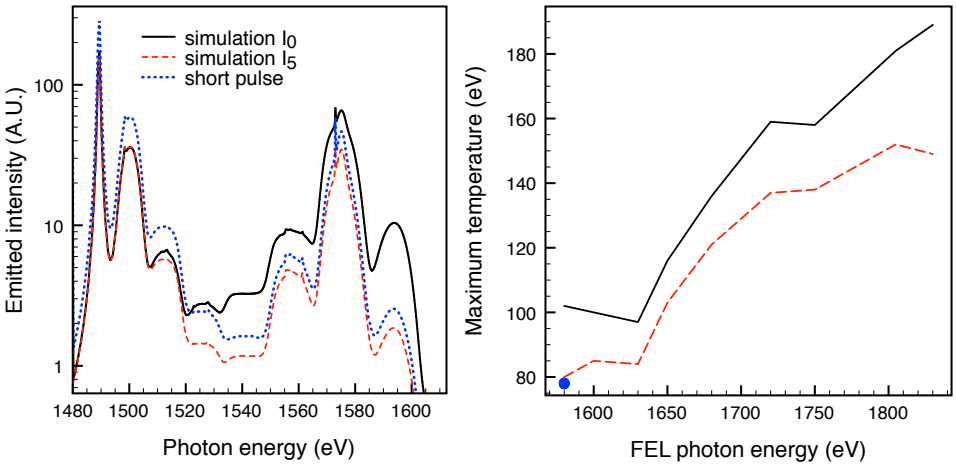

Figure 5.4: On the left are compared single intensity simulations for the spectrum at an FEL photon energy of 1580 eV. The first two labels refer to the intensities I_n defined in §5.1.1, whilst the simulation labelled as "short pulse" has the same intensity as I_0 but the same fluence as I_5. On the right are plotted the maximum temperatures reached in simulations I_0 and I_5 as a function of the FEL photon energy; the blue dot refers to the temperature corresponding to the short pulse simulation reported on the left, which as expected matches the simulation I_5 having the same fluence.

impossible to reproduce the experimentally observed line if this simulation is taken as the one at the maximum intensity for this pumping condition. The lines which are pumped by P processes (IV and V) are instead perfectly overlapping for the two simulations (note that the spectra shown here are not renormalized to get the overlap). A third simulation, having the same intensity as I_0 but the same fluence as I_5 (i.e. having a 1.7 times shorter pulse duration), is plotted as well for comparison, showing that the ratio between line XI and the other lines is not affected by the choice of the pulse duration: that is to say that the difference between the simulations is indeed due to the pulse energy, not to the aforementioned overestimation of the LCLS pulse length.

The reproduction of line XI at 1580 eV however also depends on the accuracy by which the far wings of the laser spectrum are reproduced: re-

calling that the nominal FWHM bandwidth at 1580 eV is 7.9 eV, a small deviation on either the bandwidth or the fluence can yield a notable difference in terms of the overlap between the FEL spectrum and the line (causing the off-resonance pumping of the transition). Given also the insensitivity of the lines pumped by P processes to the small difference in maximum fluence (see line IV and V), it is thus impossible to determine the best value for the beamline transmission from the Al data alone, so that it is useful to provide an estimation of the possible errors derived by the choice of using the nominal transmission rather than the measured one.

In order to do so, the right plot in Fig. 5.4 compares the maximum temperature calculated in simulation I_0 and I_5 for different FEL photon energies. The maximum temperatures across the photon energy range investigated, calculated by assuming either the nominal (I_0) or the measured (I_5) transmission, are shown to differ at most by 20%. Since all of the temperatures are still high enough to allow for the thermal population of the relevant charges for the lines IV-XI, and – as discussed in Chapter 3 – each line is emitted when the average ionization (determining n_e) roughly equals that of the absorbing ion, the main features of the spectra are unaffected by the choice. Importantly, as the IPD is independent of the temperature at high densities, the measurement of the K-edges is also unaffected.

5.2 Instantaneous thermalization

Provided that the FEL properties are reasonably modeled, the most important factor determining the reliability of the simulations is a suitable reproduction of the mechanism by which the laser energy is deposited into the system. As explained in §1.2.2, the SCFLY simulations rely on the assumption of instantaneous thermalization of the free electrons in order to

determine a self consistent temperature, that is in turn used to calculate the collisional rates required to solve the rate equations.

In the real system, the main part of the absorbed energy is transformed, via PA process, into kinetic energy of Auger electrons. A rough estimate of the characteristic timescale for the thermalization can then be inferred by considering a population of fast Auger electrons at an energy E ∼1400 eV, produced in the initial stages of the laser absorption, thermalizing with a population of cold electrons at a density $n \sim 2{\times}10^{23}$ cm^{-3}: by using a standard approach [54], this timescale is then given by $\tau \sim (6 \cdot 10^{-6} n E^{-3/2} \lambda)^{-1} \sim 4$ fs (where $\lambda \simeq 10$ is the Coulomb logarithm), which is smaller – but of the same order of magnitude – than the characteristic time required to deplete one of the charge states (see Fig. 3.5).

Although this value seems to reasonably support the validity of the approximation, it must be stressed that the error on this estimate can be quite substantial, as for example the definition of the Coulomb logarithm itself is non trivial in strongly coupled conditions (see e.g. [91]). Moreover one could argue that the energy is continuously stored as kinetic energy of Auger electrons as the pulse is absorbed, so that a marked two temperature distribution may still be present: as a result, if this stored energy is not in turn transferred to the ion system (by direct collisional ionization or after thermalization) at the same rate as if it were directly stored in a thermal electron distribution, this may strongly impact the simulated (collisional) plasma evolution.

5.2.1 Auger electrons simulations

In order to better understand the impact of the non-thermal effects I modified the SCFLY model, in such a way as to separate the free electrons arising

from Auger processes from the thermal electrons.

The idea is to extend at each time step the population array $N_i(t)$ by adding a bin $N_k(t)$ – containing Auger electrons at energy E_k – for each of the Auger transitions active at the given time; these bins are then populated by Auger transitions and depopulated by collisional processes involving an Auger electron of the given energy. The simplifying assumption is that a single collision makes an Auger electron a thermal one.

If $R\delta_{j(k)}$ is the Auger rate for the transition generating an Auger electron of energy E_k from the decay of specific state N_j, and if R^k_{ij} is a collisional rate for a transition $N_j \rightarrow N_i$ involving an Auger electron at E_k, whilst R^k_{fr} is the Auger thermalization rate as defined above (τ^{-1}, where λ is that described in [92]), then the rate equations, that is Eq. (1.3), are modified to

$$\frac{d}{dt}\begin{pmatrix} N_i \\ N_k \end{pmatrix} = \sum_{j \neq i} \begin{pmatrix} R_{ij} + \sum_k R^k_{ij} N_k \\ R\delta_{j(k)} - \sum_i R^k_{ij} N_k \end{pmatrix} N_j - \begin{pmatrix} \sum_{j \neq i} [R_{ji} + \sum_k R^k_{ji} N_k] N_i \\ R^k_{fr} n_e N_k \end{pmatrix}$$

where the free electron density n_e includes only the thermal electrons. Apart from R^k_{fr} all of the rates for the collisional processes involving Auger electrons are calculated using the standard routines for non thermal distributions used in SCFLY [81], modified so that the distribution for each of the Auger bins is a delta function at the relevant energy E_k.

The energy balance is modified as well so that the temperature of the thermal distribution is determined by what fraction of the laser energy stored into Auger energies (as a consequence of PA processes) is in turn given back to the plasma by collisions (both Auger-ion and Auger-thermal).

The results of a simulation using this modified model, for an FEL photon energy of 1630 eV, is shown in Fig. 5.5. The uppermost plot shows that the temperature and density evolution from this simulation perfectly

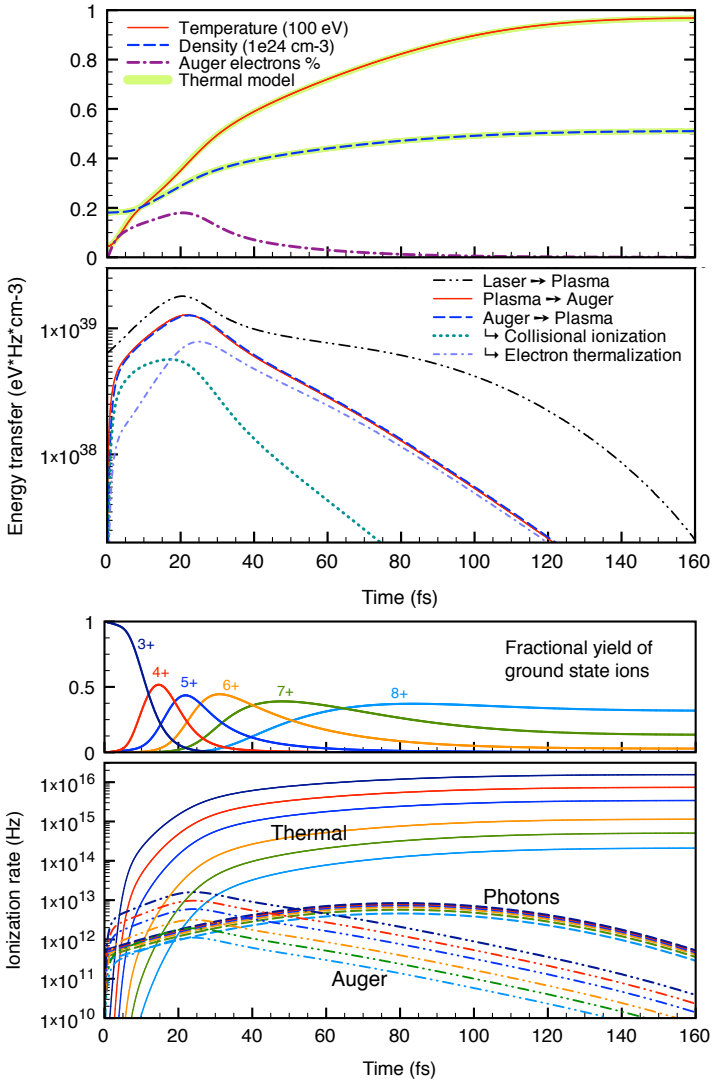

Figure 5.5: SCFLY simulation, using the modified model with non-thermal Auger electrons, for an FEL photon energy of 1630 eV. Top – The electron density and temperature evolution are compared with those obtained by a standard simulation with the same parameters, showing a perfect overlap; on the same plot it is shown the evolution of the total Auger population ($\sum_k N_k$) as a percentage on the total number of free electrons. This is to be compared with the energy transfer rates plotted immediately below. Bottom – Time evolution of the CSD considering only ground state ions, and evolution of the ionization rates for the L-shell electrons of those ions, due to either thermal electrons, Auger electrons or photons.

overlap with those obtained by using the standard SCFLY thermal model. On the same plot is also shown the evolution of the total population of Auger electrons, whose number never exceeds the 0.2% of the total number of free electrons. The reason why the Auger population is always so low when compared with that of the thermal electrons is intimately connected with the success of the thermal model: if one looks at the energy transfer rates on the second plot, it is clear that the energy transferred from the plasma (meaning the ions and thermal electrons) to the Auger population, through A processes, is immediately returned to the system through collisional processes where the Auger electrons lose their kinetic energy. Recall that this also means that the population of the Auger bins N_k is immediately reduced, with the slowed-down electrons migrating to the (thermal) free electron density.

It is interesting to note that the laser absorption and the energy transfer to the Auger system (and back) become uncorrelated at later times, when only charge states above the 5^+ are populated (see CSD in the lower plot), that have a K-edge which is above the FEL photon energy (see Fig 4.4). The shoulder in the absorption profile at later times is then due to V processes only, that don't involve the creation of Auger electrons (the Auger population rapidly decays), but would still generate fast photoelectrons with similar energies: a similar treatment as the one discussed for the Auger populations could be applied to these electrons as well, and would credibly yield very similar results.

The energy transferred from the Auger system to the plasma can be decomposed in the contributions of the different collisional processes, and the energy transfer plot in Fig. 5.5 also shows the two leading terms of this decomposition. At the beginning of the simulation, the main mechanism

responsible for the thermalization of the Auger electrons is the collisional ionization of L-shell electrons from ground state ions, but as the free electron density increases, so does R^k_{fr}, and the collisions with the thermal electrons eventually overcome the collisions with the ions. Note that, for the case of the collisional ionization, in reality it takes a few collisions for the Auger electron to actually thermalize, but the depopulation of the bin at energy E_k is still given by single collisions. A proper treatment including bins for the electrons having a residual high kinetic energy, after the collision, would be complicated by the modelling of the energy sharing between ionized and ionizing electron. The energy loss rate of the slower (still non-thermalized) electrons is however expected to be even greater than that of the Auger bins, considering the standard scaling $E^{-3/2}$ for the collisional rates of fast particles with colder electrons or ions [54].

A comparison between the rates for the collisional ionization of L-shell electrons, by Auger and thermal electrons, and the rates of the corresponding V processes, is shown in the bottom part of Fig. 5.5, for different charge states. With the exception of the 3^+ ground state (which of course cannot be thermally ionized when the system is still cold), by the time each of the charge states is appreciably populated, the thermal collisional ionization is shown to overcome the collisional ionization by Auger electrons. The thermal model is thus able to reproduce the same collisional evolution. The rates for the ionization by Auger electrons remain however greater than the photoionization rates during the period corresponding to the production of Auger electrons (recall they stop being produced when $z \geq 6$).

Finally note that the equivalence between the thermal model and the one presented here is not sensitive to errors on the determination of R^k_{fr} (whose evaluation is, as mentioned before, problematic for strongly coupled condi-

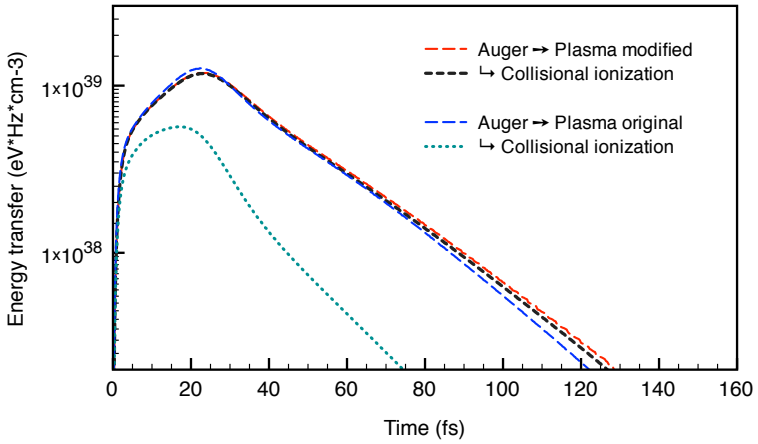

Figure 5.6: Energy transferred from the Auger population to the plasma in the limit of zero collision between thermal and Auger electrons. The same quantity and its ionization component, as reported on Fig. 5.5, are plotted for comparison. The transfer for the modified model is entirely due to collisional ionization of L-shell electrons.

tions): this can be seen by performing the same simulation, but assuming the worst case scenario of $R^k_{fr} = 0$ (if in contrast the thermalization is faster then the agreement with the thermal model can only improve). The results of such a calculation on the energy transfer rates are compared in Fig. 5.6 with the results discussed above. The energy transfer from the Auger system to the plasma is basically unchanged, but with no competing process now all of the energy is transferred by collisional ionization of L-shell electrons. That is to say, the collisional ionization, even if occurring at a slower pace than what would be that of the thermal-Auger thermalization, is still fast enough to ensure that all of the energy stored in the Auger system (depending only on the laser and CSD history) is instantaneously returned to the plasma.

Of course the Auger bins are now more slowly depleted, and indeed their maximum population now is increased to 0.45% of the free electron density (rather than 0.2%), and peaks at 25 fs (rather than 20 fs), but the

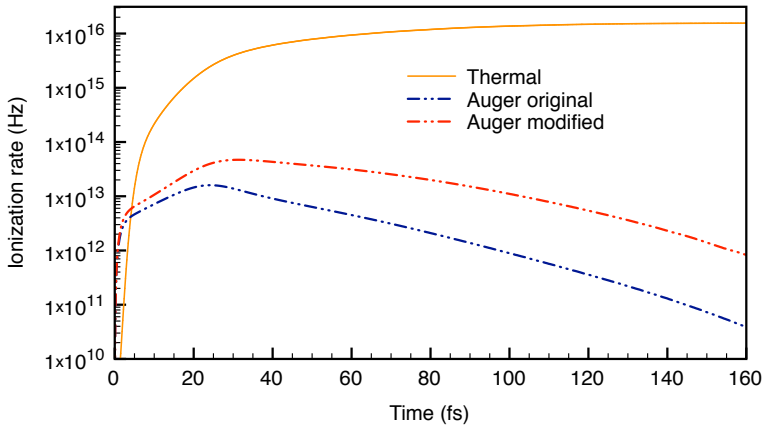

Figure 5.7: Collisional ionization rates for the complete Auger model, and the one at $R^k_{fr} = 0$, compared with the thermal ionization rates. The figure shows as an example the rate for 3^+ ions.

consequent increase of the Auger collisional rates is not so substantial as to modify the time at which the collisions with thermal electrons dominate, as can be clearly seen in Fig. 5.7. As a result, the collisional ionization by thermal electrons is still the dominant mechanism ruling the ionization of each given charge state, so that the plasma evolution is still indistinguishable from the model assuming instantaneous thermalization.

In conclusion, a study of the impact on the simulations of the FEL parameters (pulse duration and energy, spatial and temporal profile) reveals that the Al data are mainly sensitive to the spatial intensity distribution of the laser, which cannot be simply approximated with a Gaussian profile, but needs to be characterized experimentally; conversely, the uncertainties on the pulse duration (large) and on the pulse energy have negligile effects on the final results, whilst temporal profile (SASE) effects may become relevant only for single shot data. Simulations performed with a modified version of

SCFLY, including rate equations for the populations of fast electrons, also show that, due to high collisionality of the Auger electrons with either the ions or thermal electrons, the growth of a non-thermal component of the electron distribution is strongly suppressed, so that the instantaneous thermalization approximation used in SCFLY provides an accurate description of system.

CHAPTER 6

Conclusions and future work

6.1 Summary and Conclusions

I have presented the results of the first study in which an extremely well characterized HDM plasma is driven by an X-ray FEL, and is described by a non-LTE model in which the plasma parameters (n_e, T) are not imposed by the user.

Particular care has been taken initially in validating and testing the SCFLY simulation package, by modelling the first available experimental data obtained at the LCLS [46,47]: the study of the simplified (collisionless) case of a Ne gas has allowed for the separation of specific factors determining the modelling capabilities of the simulations (such as the cut-off of the spatial FEL profile, or the accuracy of the atomic data required by the presence of

resonant transitions), and for the establishment of a procedure to model the three-dimensional experimental system by using the zero-dimensional SCFLY model.

The K_α spectroscopic data obtained by the first experiment where the LCLS interacts with a solid were then interpreted by using this modelling platform, leading to the experimental demonstration of the possibility of creating and diagnosing HDM Al samples in well defined conditions, on inertially confined timescales, by using an X-ray FEL [1]. The opportunity to directly model the microscopic details of the interaction between the laser and the plasma, a unique feature of the X-ray drive, provides one with an unprecedented level of detail about the fast plasma evolution, as I hope to have shown in this thesis, and makes the code able to reproduce the experimental data with no other input by the user than a reasonable spatial and temporal description of the laser pulse. Temperatures up to 190 eV at solid density were calculated by the simulations, as a consequence of the energy balance for the detailed transitions occurring in the system.

The simulations have also proven that the progressive ionization of the Al sample, at solid density, is dominated by collisional events, rather than by photoabsorption processes, so that the CSD is very weakly dependent on the laser wavelength, in stark contrast with the low density (Ne) case. The FEL pump can thus be used, by varying the wavelength, also as a selective probe of the plasma, revealing by K_α spectroscopy only those charge states for which the laser photon energy is above the corresponding K-edge value. This has led to the first charge resolved measurement of the IPD in a HDM plasma [2], that has proven that the standard model of continuum lowering used in dense plasma simulations, the SP model, is not accurate for our experimental conditions. The data are still described by the older EK model,

predicting a stronger scaling of the IPD with the charge of the ion.

The effects of the detailed features of the laser pulse, and of the non-thermal collisional effects on the simulations have also been discussed. Whilst the spatial intensity profile of the FEL is shown to visibly affect the space-integrated data, effects related to its temporal profile, as well as the effects of a non-thermal electron distribution due to the Auger processes, have a negligible impact on the final results.

Both the demonstration of the isochoric heating to the HDM regime by an X-ray FEL, as described in Chapter 3, and the results of the IPD measurements, described in Chapter 4, have potentially profound implications for the physics of dense plasmas. On the one hand, the work described in this thesis proves the existence of an experimental platform where relatively thick, uniform samples of strongly coupled plasmas, in (n, T) conditions similar to those of the solar interior, can be generated by an easy-to-model pumping process: this can essentially pave the way for a new phase of validation of the models used in dense plasma calculations – quite often outside their regime of validity – in order to determine experimental plasma parameters by fit procedures (such as line ratio, Thomson scattering or Stark broadening measurements), since densities and temperatures – and above all their spatial/temporal gradients – can now be easily retrieved by simply modelling the laser absorption. Even if the present policy at FELs is to dedicate very short wavelength beamlines to the study of WDM/HDM[1], which are not suitable for the kind of studies described here, I am sure that with an increasing involvement in FEL experiments of the general laser-plasma community (which at present is only a minority with respect to the high-pressure/Thomson-scattering community, using the FEL as a short-wavelength probe), this sort of study will eventually become a priority and

[1]Both the MEC endstation at LCLS, and the future HED [93] endstation at XFEL work at photon energies above 4 keV

will have a tremendous impact on the way we diagnose dense plasmas.

On the other hand, the IPD measurements presented here not only are a clear example of the kind of validation measurements just discussed, but also take full advantage of the exquisite probing capability of the tunable X-ray pump. Furthermore, given the wide use of the SP model in dense plasma calculations, and the strong impact of potential errors for the IPD on quantities like the opacity and compressibility for the kind of plasmas found in astrophysical or ICF systems, a new phase of both theoretical and experimental investigation on continuum lowering is essential. Some of the research work performed in this direction, as a consequence of the IPD results discussed in this thesis, is briefly indicated below.

6.2 Further work on IPD

The work described in [2] has predictably already attracted some interest in the dense plasma community. From a theoretical point of view, a few attempts have been made to explain the experimental results by operating corrections to the SP model [94, 95], and the author is aware of two self-consistent-field approaches to reproduce the experimental IPDs being currently developed by other theoretical groups. Recently a DFT (Density Functional Theory) approach, showing agreement with the data, was also developed within our group and the results have been recently published [96].

With regard to the experimental investigation, we performed a second experiment at the LCLS in April 2013, using the same technique described in this thesis in order to measure the IPDs in different materials. At the same time, the results of two other experiments, performed at optical laser facilities, have been published [78, 97] showing pressure ionization effects in compressed materials. I will now briefly describe these three experiments.

6.2.1 LCLS experiment on different materials

A substantial part of my last year's work has been dedicated to the design, execution and data analysis of a new LCLS experiment dedicated to the measurement of the IPD in a wider range of conditions. The experiment, performed again at the SXR endstation, successfully determined the IPDs for different charge states in Mg, Al, Si, Al in Al_2O_3, Si in SiO_2, Al and Si in Mica. Although Mg and Si are not too dissimilar from Al (from an atomic point of view), all of these materials have different crystalline structures, different ion densities, and in the case of the compounds the lighter elements surrounding the active ions inevitably destroy the condition $z = \bar{z}$ shown to hold for the Al case at the time of the IPD measurement; the IPD is thus truly measured in a variety of (n_i, n_e, T) conditions. During the experiment we also explicitly tuned the FEL to be in resonance with the He_β line of Al and observed no effect of resonant pumping, confirming the results on the pressure ionization of the M-shell for all of the charge states, as described in Chapter 4 (see also the Orion results below).

The analysis of the data from this experiment is in a very advanced stage, and I plan to describe the extensive set of results in a paper in the near future.

6.2.2 Pressure ionization at Orion and OMEGA

As discussed, our Al spectra indicate a pressure-ionized M-shell for He-like ions at solid density. A contrasting result is claimed by the authors of [78]. Using the Orion laser at AWE (Aldermaston, UK) they have compressed with a ns pulse ∼100 nm Al foils buried in ∼10 μm layers of plastic or diamond, and subsequently heated them with a ps pulse to temperatures around 700 eV. By looking at the He_β and Ly_β emission, and determining

the density in each shot by Stark broadening of these lines, the density at which the lines disappear is between 5.5 and 9 g·cm^{-3}. This is to be compared with the 2.7 g·cm^{-3} (solid density) of our measurement, and the 11.6 g·cm^{-3} the authors calculate as the point at which the line is pressure ionized according to SP.

Although one could ask the legitimate question of why the calculation of the fluctuating microfield – determining the Stark profile [98], and thus the 'experimental' densities – is any more reliable than the calculation of the perturbative static micropotential, i.e. the IPD, in strongly coupled conditions, the results of this work seem to exclude that the EK model with C=1 can be applied at temperatures that are a factor of ∼4 higher than those obtained at the LCLS (as hypothesized in [99]): even if this may seem a little difference in terms of coupling parameter, the strong temperature dependence of the critical density (4.7), with $n_{crit}^{AWE} \sim 60 \cdot n_{crit}^{LCLS} \sim 5 \times 10^{21}$ cm^{-3} (recall that higher n_{crit} means weaker coupling at a given density), and the fact that the coupling conditions for the Al system are at the borderline between different coupling regimes (see Fig. 1.1), may still explain the discrepancy between the two experiments. The work in [95] attempts to reconcile the two results, but cannot fully reproduce the LCLS data.

On the other hand, an experiment – described in [97] – performed at the OMEGA laser (Rochester, NY, USA) shows that the IPD, in an even more strongly coupled system, is greater than that predicted by their Thomas-Fermi model (recall that SP is essentially a Thomas-Fermi model itself). In the study, plastic spherical capsules are compressed, by using three shocks, to densities up to ∼7 times that of the initial solid at temperatures around 10 eV, and a backlighter source is used in order to investigate the density and temperature evolution of the system by X-ray Thomson scattering. The

scattering spectra can only be described by assuming a higher than predicted ionization of the carbon sample (4^+ rather than 2^+), and the hydrodynamic simulations agree with the electron density results only under the same assumption. Given the low temperature, that cannot justify the thermal ionization of the L-shell, the increased ionization is interpreted in terms of pressure ionization due to an higher than predicted IPD.

6.3 Further work on the Al data

Apart from the follow-up work on the IPD, the work on the Al data described in this thesis can be further expanded to investigate particular aspects of the physics involved in the plasma evolution. A clear example is given by the line emission for below edge lines caused by the collisional ionization of L-shell electrons in ions with a K-shell hole, as discussed in §3.3. By considering the ratio between the emission recorded above and below the edge for different pairs of neighbouring lines, and comparing with detailed SCFLY calculations, a charge resolved measurement of the collisional ionization rates in a HDM system can be performed, and the results of such a study are currently being prepared for publication.

The large set of space and time resolved simulations partially presented here, describing the timescales of the local plasma evolution, or the importance of the contribution of the colder zones of the plasma to the observed results, remain at present unpublished. The same holds for the detailed analysis on the FEL parameters presented in Chapter 5, as well as for the discussion of the non-thermal effects due to the generation of Auger electrons as a consequence of the main laser absorption mechanism. As these are all important aspects of the physics of the experiment, but still could not be properly discussed in the main publications [1,2,55] due to the space

constraint imposed by the respective journals, I plan to eventually discuss them in a dedicated synoptic longer paper.

6.4 Further work on SCFLY

Apart from the modified model described in §5.2.1, a new modified version of SCFLY has been developed in order to model FEL experiments in which the target is a compound. The standard way of modelling mixtures of elements in FLYCHK/SCFLY, as described in [81], is to perform the detailed non-LTE calculation only for a given species and to assume an average ionization for any secondary species: that is to say the only effect of secondary species is to increase the electron density by a fixed amount. Even if this procedure is appropriate for plasmas in which the species of interest is embedded in a well defined plasma environment (e.g. heavy ions embedded in a fully ionized hydrogen plasma), the model is not suitable to describe plasmas in which more than a single species is heated during the laser pulse, such as in the case of the oxides used in our last LCLS experiment: the subsets of rate equations corresponding to different elements are in fact coupled by the time dependent calculation of the density and temperature and cannot be solved independently (the ionization balance can be regarded as an additional rate equation $dn_e/dt = \sum z_i dN_i/dt$, where the populations N_i belong to different species). For this reason I modified the SCFLY model in order to solve the rate equations for a given set of different elements at the same time.

The new model has been tested and is able to reproduce tabulated transmission data [89] for oxides at low temperatures, and will soon be used to model the results of the new LCLS experiment measuring the IPD in silica, alumina and mica.

In conclusion, the work on the hot-dense Al plasma produced at the LCLS provides the foundations for a novel class of laser-plasma benchmark experiments exploiting the excellent pumping/probing capabilities of the newly available 4th generation X-ray sources; the first result of such experiments, a charge resolved measurement of the IPD in a HDM system, has already challenged the way we model – and thus diagnose – dense plasmas, and the results of the first set of follow-up LCLS measurements will be soon released. Further analysis of the Al data and further development of the SCFLY code, as described above, are also in progress, and clearly identify the near-term direction of the research following this work.

References

[1] S. M. Vinko, O. Ciricosta, B. I. Cho, K. Engelhorn, H.-K. Chung, et al. Creation and diagnosis of solid-density hot-dense matter with an X-ray free-electron laser. *Nature (London)*, 482:59–63, 2012.

[2] O. Ciricosta, S. M. Vinko, H.-K. Chung, B.-I. Cho, C. R. D. Brown, et al. Direct Measurements of the Ionization Potential Depression in a Dense Plasma. *Physical Review Letters*, 109:065002, 2012.

[3] P. Debye and E. Hückel. Zur Theorie der Elektrolyte. *Physikalische Zeitschrift*, 24:185–206, 1923.

[4] L. Tonks and I. Langmuir. Oscillations in Ionized Gases. *Physical Review*, 33:195–210, 1929.

[5] J. Nuckolls, L. Wood, A. Thiessen, and G. Zimmerman. Laser Compression of Matter to Super-High Densities: Thermonuclear (CTR) Applications. *Nature*, 239:139–142, 1972.

[6] S. X. Hu, B. Militzer, V. N. Goncharov, and S. Skupsky. Strong Coupling and Degeneracy Effects in Inertial Confinement Fusion Implosions. *Physical Review Letters*, 104:235003, 2010.

[7] J. Lindl. Development of the indirect-drive approach to inertial confinement fusion and the target physics basis for ignition and gain. *Physics of Plasmas*, 2(11):3933–4024, 1995.

[8] J. D. Lindl, P. Amendt, R. L. Berger, S. G. Glendinning, S. H. Glenzer, et al. The physics basis for ignition using indirect-drive targets on the National Ignition Facility. *Physics of Plasmas*, 11(2):339–491, 2004.

[9] S. P. Hatchett. Ablation Gas Dynamics of Low-Z Materials Illuminated by Soft X-Rays. *Techical report. Presented at the Inertial Fusion Lecture Series, Princeton, NJ, Apr. 1991*.

[10] D. Colombant, M. Klapisch, and A. Bar-Shalom. Increase in Rosseland mean opacity for inertial fusion hohlraum walls. *Physical Review E*, 57:3411–3416, 1998.

[11] J. N. Bahcall, W.F. Huebner, S. H. Lubow, P. D. Parker, and R. K. Ulrich. Standard solar models and the uncertainties in predicted capture rates of solar neutrinos. *Reviews of Modern Physics*, 54:767–799, 1982.

[12] D. B. Guenther, P. Demarque, Y.-C. Kim, and M. H. Pinsonneault. Standard solar model. *The Astrophysical Journal*, 387:372–393, 1992.

[13] C. A. Iglesias and F. J. Rogers. Opacities for the solar radiative interior. *The Astrophysical Journal*, 371:408–417, 1991.

[14] C. A. Iglesias and F. J. Rogers. Updated Opal Opacities. *The Astrophysical Journal*, 464:943, 1996.

[15] J. E. Bailey, G. A. Rochau, C. A. Iglesias, J. Abdallah, J. J. MacFarlane, et al. Iron-Plasma Transmission Measurements at Temperatures Above 150 eV. *Physical Review Letters*, 99:265002, 2007.

[16] F. Perrot and M. W. C. Dharma-wardana. Spin-polarized electron liquid at arbitrary temperatures: exchange-correlation energies, electron-distribution functions, and the static response functions. *Physical Review B*, 62:16536–16548, 2000.

[17] R. W. Lee, S. J. Moon, H.-K.Chung, W. Rozmus, H. A. Baldis, et al. Finite temperature dense matter studies on next-generation light sources. *Journal of the Optical Society of America B*, 20(4):770–778, 2003.

[18] G. Steinmeyer, D. H. Sutter, L. Gallmann, N. Matuschek, and U. Keller. Frontiers in Ultrashort Pulse Generation: Pushing the Limits in Linear and Nonlinear Optics. *Science*, 286(5444):1507–1512, 1999.

[19] H. Daido. Review of soft x-ray laser researches and developments. *Reports on Progress in Physics*, 65(10):1513, 2002.

[20] M. Zepf, B. Dromey, M. Landreman, P. Foster, and S. M. Hooker. Bright Quasi-Phase-Matched Soft-X-Ray Harmonic Radiation from Argon Ions. *Physical Review Letters*, 99:143901, Oct 2007.

[21] Z. Huang and K.-J. Kim. Review of x-ray free-electron laser theory. *Physical Review Special Topics – Accelerators and Beams*, 10:034801, 2007.

[22] H. Motz. Applications of the Radiation from Fast Electron Beams. *Journal of Applied Physics*, 22(5):527–535, 1951.

[23] T. H. Maiman. Stimulated Optical Radiation in Ruby. *Nature*, 187:493–494, 1960.

[24] J. M. J. Madey. Stimulated Emission of Bremsstrahlung in a Periodic Magnetic Field. *Journal of Applied Physics*, 42(5):1906–1913, 1971.

[25] A. L. Robinson. History of Synchrotron Radiation, in *X-ray data booklet (A.Thompson et al.)*. Center for X-Ray Optics and Advanced Light Source, LBNL, Berkeley CA, 2009.

[26] R. W. Schoenlein, S. Chattopadhyay, H. H. W. Chong, T. E. Glover, P. A. Heimann, et al. Generation of Femtosecond Pulses of Synchrotron Radiation. *Science*, 287(5461):2237–2240, 2000.

[27] N. M. Kroll and W. A. McMullin. Stimulated emission from relativistic electrons passing through a spatially periodic transverse magnetic field. *Physical Review A*, 17:300–308, Jan 1978.

[28] R. Bonifacio, C. Pellegrini, and L.M. Narducci. Collective instabilities and high-gain regime in a free electron laser. *Optics Communications*, 50(6):373 – 378, 1984.

[29] S. V. Milton, E. Gluskin, N. D. Arnold, C. Benson, W. Berg, et al. Exponential Gain and Saturation of a Self-Amplified Spontaneous Emission Free-Electron Laser. *Science*, 292(5524):2037–2041, 2001.

[30] E. L. Saldin, E. A. Schneidmiller, and M. V. Yurkov. Self-amplified spontaneous emission FEL with energy-chirped electron beam and its application for generation of attosecond x-ray pulses. *Physical Review Special Topics – Accelerators and Beams*, 9:050702, 2006.

[31] FLASH homepage. `http://flash.desy.de/`.

[32] V. Ayvazyan, N. Baboi, J. Bähr, V. Balandin, B. Beutner, et al. First operation of a free-electron laser generating GW power radiation at 32 nm wavelength. *The European Physical Journal D - Atomic, Molecular, Optical and Plasma Physics*, 37(2):297–303, 2006.

[33] LCLS homepage. `http://lcls.slac.stanford.edu/`.

[34] P. Emma, R. Akre, J. Arthur, R. Bionta, C. Bostedt, et al. First lasing and operation of an angstrom-wavelength free-electron laser. *Nature Photonics*, 4(9):641–647, Sep 2010.

[35] FERMI homepage. `https://www.elettra.trieste.it/FERMI/`.

[36] SACLA homepage. `http://xfel.riken.jp/eng/index.html/`.

[37] European XFEL homepage. `http://xfel.eu/`.

[38] SwissFEL homepage. `http://www.psi.ch/swissfel/`.

[39] J. Arthur, P. Anfinrud, P. Audebert, K. Bane, I. Ben-Zvi, et al. Linac coherent light source (LCLS) conceptual design report. 2002.

[40] P. Kirkpatrick and A. V. Baez. Formation of Optical Images by X-Rays. *Journal of the Optical Society of America*, 38(9):766–773, 1948.

[41] H.-K. Chung, M.H. Chen, and R.W. Lee. Extension of atomic configuration sets of the Non-LTE model in the application to the K[alpha] diagnostics of hot dense matter. *High Energy Density Physics*, 3(1-2):57 – 64, 2007. Radiative Properties of Hot Dense Matter.

[42] H.-K. Chung, M.H. Chen, W.L. Morgan, Y. Ralchenko, and R.W. Lee. FLYCHK: Generalized population kinetics and spectral model for rapid spectroscopic analysis for all elements. *High Energy Density Physics*, 1(1):3 – 12, 2005.

[43] FLYCHK homepage. `http://nlte.nist.gov/FLY/`.

[44] J.P. Apruzese. An analytic Voigt profile escape probability approximation. *Journal of Quantitative Spectroscopy and Radiative Transfer*, 34(5):447 – 452, 1985.

[45] L. Fang, M. Hoener, O. Gessner, F. Tarantelli, S. T. Pratt, et al. Double Core-Hole Production in $\mathbf{N}_2$: Beating the Auger Clock. *Physical Review Letters*, 105:083005, Aug 2010.

[46] O. Ciricosta, H.-K. Chung, R. W. Lee, and J. S. Wark. Simulations of neon irradiated by intense X-ray laser radiation. *High Energy Density Physics*, 7(3):111 – 116, 2011.

[47] L. Young, E. P. Kanter, B. Krässig, Y. Li, A. M. March, et al. Femtosecond electronic response of atoms to ultra-intense X-rays. *Nature*, 466(7302):56–61, 2010.

[48] N. Rohringer and R. Santra. X-ray nonlinear optical processes using a self-amplified spontaneous emission free-electron laser. *Physical Review A*, 76(3):033416, Sep 2007.

[49] M. Ya. Amusia, I. S. Lee, and V. A. Kilin. Double Auger decay in atoms: Probability and angular distribution. *Physical Review A*, 45(7):4576–4587, 1992.

[50] M. O. Krause, M. L. Vestal, W. H. Johnston, and T. A. Carlson. Readjustment of the Neon Atom Ionized in the K Shell by X Rays. *Physical Review*, 133(2A):A385–A390, 1964.

[51] G. Doumy, C. Roedig, S.-K. Son, C. I. Blaga, A. D. DiChiara, et al. Nonlinear Atomic Response to Intense Ultrashort X Rays. *Physical Review Letters*, 106:083002, 2011.

[52] R. Bonifacio, L. De Salvo, P. Pierini, N. Piovella, and C. Pellegrini. Spectrum, temporal structure, and fluctuations in a high-gain free-electron laser starting from noise. *Physical Review Letters*, 73(1):70–73, 1994.

[53] W. Xiang, C. Gao, Y. Fu, J. Zeng, and J. Yuan. Inner-shell resonant absorption effects on evolution dynamics of the charge state distribution in a neon atom interacting with ultraintense x-ray pulses. *Physical Review A*, 86:061401, 2012.

[54] J. D. Huba. NRL Plasma Formulary. Naval Research Laboratory, Washington, D.C., 2009.

[55] B. I. Cho, K. Engelhorn, S. M. Vinko, H.-K. Chung, O. Ciricosta, et al. Resonant K_α Spectroscopy of Solid-Density Aluminum Plasmas. *Physical Review Letters*, 109:245003, 2012.

[56] J. Chalupský, J. Krzywinski, L. Juha, V. Hájková, J. Cihelka, et al. Spot size characterization of focused non-Gaussian X-ray laser beams. *Optics Express*, 18(26):27836–27845, Dec 2010.

[57] J. Auerhammer, H. Genz, A. Kumar, and A. Richter. Two-electron one-photon transition in aluminum following double K-shell ionization. *Physical Review A*, 38:688–693, Jul 1988.

[58] J. Bailey, A. L. Carlson, G. Chandler, M. S. Derzon, R. J. Dukart, et al. Observation of K_α X-ray satellites from a target heated by an intense ion beam. *Laser and Particle Beams*, 8:555–562, 12 1990.

[59] J.H. Hubbell, P.N. Trehan, N. Singh, B. Chand, M.L. Garg, et al. A review, bibliography, and tabulation of K, L, and Higher atomic shell x-ray fluorescence yields. *Journal Name: Journal of Physical and Chemical Reference Data*, 1994.

[60] J. D. Garcia, R. J. Fortner, and T. M. Kavanagh. Inner-Shell Vacancy Production in Ion-Atom Collisions. *Reviews of Modern Physics*, 45:111–177, 1973.

[61] N. H. Burnett, G. D. Enright, A. Avery, A. Loen, and J. C. Kieffer. Time-resolved K_α spectra in high-intensity laser-target interaction. *Physical Review A*, 29:2294–2297, 1984.

[62] C. A. Back, C. Chenais-Popovics, P. Renaudin, J. P. Geindre, P. Audebert, et al. Study of K_α absorption structures in a subcritical-density laser-produced plasma. *Physical Review A*, 46:3405–3412, 1992.

[63] A. Saemann, K. Eidmann, I. E. Golovkin, R. C. Mancini, E. Andersson, et al. Isochoric Heating of Solid Aluminum by Ultrashort Laser Pulses Focused on a Tamped Target. *Physical Review Letters*, 82:4843–4846, 1999.

[64] BH Armstrong, J Sokoloff, RW Nicholls, DH Holland, and RE Meyerott. Radiative properties of high temperature air. *Journal of Quantitative Spectroscopy and Radiative Transfer*, 1(2):143–162, 1961.

[65] G. Ecker and W. Kröll. Lowering of the ionization energy for a plasma in thermodynamic equilibrium. *Physics of Fluids*, 6:62–69, 1963.

[66] J. C. Stewart and K. D. Pyatt Jr. Lowering of ionization potentials in plasmas. *Astrophysical Journal*, 144:1203, 1966.

[67] G.B. Zimmerman and R.M. More. Pressure ionization in laser-fusion target simulation. *Journal of Quantitative Spectroscopy and Radiative Transfer*, 23(5):517 – 522, 1980.

[68] D. D. Burgess and R. W. Lee. High density plasma effects on atomic and ionic spectra. *Journal de Physique Colloques*, 43(C2):C2–413–C2–432, 1982.

[69] R. M. More. Electronic energy-levels in dense plasmas. *Journal of Quantitative Spectroscopy and Radiative Transfer*, 27(3):345 – 357, 1982.

[70] B. J. B. Crowley. Average-atom quantum-statistical cell model for hot plasma in local thermodynamic equilibrium over a wide range of densities. *Physical Review A*, 41:2179–2191, 1990.

[71] M. A. Sweeney. Thermodynamic inconsistency of the modified Saha equation at high pressures. *The Astrophysical Journal*, 220:335–338, 1978.

[72] H. A. Scott. Cretin – a radiative transfer capability for laboratory plasmas. *Journal of Quantitative Spectroscopy and Radiative Transfer*, 71(2-6):689 – 701, 2001.

[73] Y. T. Lee. A model for ionization balance and L-shell spectroscopy of non-LTE plasmas. *Journal of Quantitative Spectroscopy and Radiative Transfer*, 38(2):131 – 145, 1987.

[74] D. K. Bradley, J. Kilkenny, S. J. Rose, and J. D. Hares. Time-resolved continuum-edge-shift measurements in laser-shocked solids. *Physical Review Letters*, 59:2995–2998, 1987.

[75] D. Riley, O. Willi, S. J. Rose, and T. Afshar-Rad. Blue Shift of the K Absorption Edge in Laser-Shocked Solids. *Europhysics Letters*, 10(2):135, 1989.

[76] M. Nantel, G. Ma, S. Gu, C. Y. Côté, J. Itatani, et al. Pressure ionization and line merging in strongly coupled plasmas produced by 100-fs laser pulses. *Physical Review Letters*, 80:4442–4445, 1998.

[77] A. Lévy, F. Dorchies, A. Benuzzi-Mounaix, A. Ravasio, F. Festa, et al. X-Ray Diagnosis of the Pressure Induced Mott Nonmetal-Metal Transition. *Physical Review Letters*, 108:055002, 2012.

[78] D. J. Hoarty, P. Allan, S. F. James, C. R. D. Brown, L. M. R. Hobbs, et al. Observations of the Effect of Ionization-Potential Depression in Hot Dense Plasma. *Physical Review Letters*, 110:265003, 2013.

[79] D. R. Inglis and E. Teller. Ionic depression of series limits in one-electron spectra. *The Astrophysical Journal*, 90:439, 1939.

[80] K.-N. Huang, M. Aoyagi, M. H. Chen, B. Crasemann, and H. Mark. Neutral-atom electron binding energies from relaxed-orbital relativistic Hartree-Fock-Slater calculations $2 \leq Z \leq 106$. *Atomic Data and Nuclear Data Tables*, 18(3):243 – 291, 1976.

[81] H.-K. Chung, R.W. Lee, M.H. Chen, and Y. Ralchenko. The How To for FLYCHK (NIST,2008).

[82] J. Welch, F-J. Decker, Y. Ding, P. Emma, A. Fisher, et al. FEL spectral measurements at LCLS. *Proceedings of FEL2011*, FEL Experiments and Projects:461–464, 2011.

[83] J. Chalupský, P. Bohacek, V. Hájková, S.P. Hau-Riege, P.A. Heimann, et al. Comparing different approaches to characterization of focused X-ray laser beams. *Nuclear Instruments and Methods in Physics Research Section A: Accelerators, Spectrometers, Detectors and Associated Equipment*, 631(1):130 – 133, 2011.

[84] D.S. Rackstraw, S.M. Vinko, O. Ciricosta, B.I. Cho, K. Engelhorn, et al. Opacity effects in a solid-density aluminium plasma created by photo-excitation with an X-ray laser. *High Energy Density Physics*, 11(0):59 – 69, 2014.

[85] J. Wu, Y. Ding, P. Emma, Z. Huang, H. Loos, et al. LCLS X-ray pulse duration measurement using the statistical fluctuation method. *in Proceedings of the 2010 Free-Electron Laser Conference*, (paper MOPC14).

[86] S. Düsterer, P. Radcliffe, C. Bostedt, J. Bozek, A. L. Cavalieri, et al. Femtosecond x-ray pulse length characterization at the Linac Coherent Light Source free-electron laser. *New Journal of Physics*, 13(9):093024, 2011.

[87] S.P. Hau-Riege, R.M. Bionta, D. D. Ryutov, and J. Krzywinski. Measurement of x-ray free-electron-laser pulse energies by photoluminescence in nitrogen gas. *Journal of Applied Physics*, 103(5):053306–053306–9, 2008.

[88] A. A. Sorokin, U. Jastrow, P. Juranić, S. Kapitzki, K. Tiedtke, et al. *Report on Pulse energy monitoring at the SXR beamline using gas-monitor detectors*. (Technical report, SLAC, 2010).

[89] CXRO homepage. `http://henke.lbl.gov/optical_constants/`.

[90] P. Heimann, O. Krupin, W. F. Schlotter, J. Turner, J. Krzywinski, et al. Linac Coherent Light Source soft x-ray materials science instrument optical design and monochromator commissioning. *Review of Scientific Instruments*, 82(9):093104, 2011.

[91] D. O. Gericke, M. S. Murillo, and M. Schlanges. Dense plasma temperature equilibration in the binary collision approximation. *Physical Review E*, 65:036418, 2002.

[92] Y. T. Lee and R. M. More. An electron conductivity model for dense plasmas. *Physics of Fluids*, 27(5):1273–1286, 1984.

[93] HED instrument at European XFEL. `http://www.xfel.eu/research/instruments/hed/`.

[94] Carlos A. Iglesias and Philip A. Sterne. Fluctuations and the ionization potential in dense plasmas. *High Energy Density Physics*, 9(1):103 – 107, 2013.

[95] B. J. B. Crowley. Continuum Lowering – A New Perspective. arXiv:1309.1456v3 (2013).

[96] S.M. Vinko, O. Ciricosta, and J.S. Wark. Density functional theory calculations of continuum lowering in strongly coupled plasmas. *Nature Communications*, 5:3533, 2014.

[97] L. B. Fletcher, A. Kritcher, A. Pak, T. Ma, T. Doppner, et al. X-ray Thomson scattering measurements of temperature and density from multi-shocked CH capsules. *Physics of Plasmas*, 20(5):056316, 2013.

[98] H. R. Griem. *Plasma Spectroscopy*. McGraw-Hill, 1964.

[99] T. R. Preston, S. M. Vinko, O. Ciricosta, H.-K. Chung, R. W. Lee, et al. The effects of ionization potential depression on the spectra emitted by hot dense aluminium plasmas. *High Energy Density Physics*, 9(2):258 – 263, 2013.

List of Acronyms

A process	Auger decay
ADP	Ammonium dihydrogen phosphate
AWE	Atomic Weapons Establishment
C process	Collisional valence ionization
CSD	Charge State Distribution
DAQ	Data acquisition system
DFT	Density Functional Theory
DH	Debye and Hückel
EK	Ecker and Kröll
EOS	Equation Of State
FEL	Free Electron Laser
FLASH	Free electron LASer in Hamburg
FWHM	Full width at half maximum
HDM/WDM	Hot Dense Matter / Warm Dense Matter
ICF	Inertial Confinement Fusion

IPD	Ionization Potential Depression
IS	Ion-sphere model
KBO	Kirkpatrick-Baez Optics
LCLS	Linac Coherent Light Source
LTE	Local Thermal Equilibrium
LY2010	Experiment described in Ref. [47]
P process	K-shell shell Photoionization
SASE	Self-Amplified Spontaneous Emission
SP	Stewart and Pyatt
TF	Thomas-Fermi model
V process	Valence shell photoionization

List of Figures

1.1 Temperature-density phase diagram for the general plasma . 3
1.2 Comparison between XUV and X-ray sources 7
1.3 LCLS aerial view 9

2.1 Charge state distribution in a Ne gas 20
2.2 Simulations at different pump energies 23
2.3 Time evolution of the space-integrated CSD in Ne 25
2.4 Effect of resonances on the CSD of Ne 27
2.5 Local time evolution of the CSD in Ne at the focus 28
2.6 Neglecting low intensity wings in Ne simulations 30
2.7 Temperature profiles in Ne in the focal plane 31
2.8 Ion density effect on the CSD 34
2.9 Collisional population of the odd charge states 35

3.1 Experimental K_α satellites spectrum in Al at 1800 eV 41
3.2 Exprimental K_α spectra as a function of the FEL photon energy 43
3.3 SCFLY simulations for the K_α spectra of aluminium 46
3.4 Temperature and density evolution across the target 48
3.5 Local T, n and CSD evolution at different wavelengths 49
3.6 Space-time integrated CSD at different wavelengths 52
3.7 Rates of competing processes in 6^+ and 7^+ ions. 53
3.8 Calculated time dependent emission 57

4.1 Continuum lowering and pressure ionization in cold aluminum 60
4.2 Synoptics of the SP and EK models 68
4.3 Measured values for the IPD 71
4.4 Simulated spectra for SP and EK models 73
4.5 SP and EK caculations for hollow atom lines 75
4.6 Atomic shells and continuum edge, and total IPD variations . 76
4.7 Effect of the pressure ionization on the simulated spectra . . 78

5.1 Comparison between Gaussian and measured spatial profile . 84
5.2 Simulations with Gaussian and measured spatial profile . . . 85
5.3 Effects of the FEL temporal structure 88
5.4 Impact of the beamline transmission value 92
5.5 SCFLY simulation with non-thermal effects 96
5.6 Auger model with no electron-electron thermalization 99
5.7 Collisional rates with different Auger models 100

Notation

Quantity	Symbol	Value/Units
Average ionization	$\bar{z} = \langle z \rangle$	adim.
	$z^* = \langle z^2 \rangle / \langle z \rangle$	adim.
Boltzmann constant	k_B	8.617×10^{-5} eV/K
Coulomb logarithm	λ	adim. ($\sim$10)
Coupling parameters	$\Gamma_{ee} = \frac{e^2}{k_B T_e} \left(\frac{3}{4\pi n_e} \right)^{-\frac{1}{3}}$	adim.
	$\Gamma_{ei} = \Gamma_{ee} \bar{z}$	adim.
	$\Gamma_{ii} = \Gamma_{ee} \bar{z}^{\frac{5}{3}}$	adim.
Debye length	$\lambda_D = \sqrt{\frac{k_B T}{4\pi e^2 (z^*+1) n_e}}$	cm
Electron charge	e	4.803×10^{-10} esu
Electron density	n_e	cm^{-3}
Electron mass	m_e	9.109×10^{-27} g
Electron temperature	T_e or simply T	eV
Electron-Volt (cgs units)	eV	1.602×10^{-12} erg
Ion density	n_i	cm^{-3}
Fermi temperature	$T_F = \frac{\hbar^2}{2m_e} (3\pi^2 n_e)^{2/3}$	eV
Lorentz factor	$\gamma = 1/\sqrt{1 - v^2/c^2}$	adim.
	$\gamma_e = m_e \gamma c^2 / m_e c^2$	E[GeV]$/0.511 \times 10^{-3}$
Particle density	$n = n_e + n_i$	cm^{-3}
Reduced Planck constant	$\hbar = h/2\pi$	1.054×10^{-27} erg $\cdot$ s
Speed of light	c	2.998×10^{10} cm/s
Undulator parameter	$K_0 = \frac{eB\lambda_u}{2\pi m_e c}$	$0.934 \cdot B$[T]λ_u[cm]